Wearable Power Sources and Self-powered Sensors Based on the Triboelectric Nanogenerators

Ziang Feng

Dissertation submitted to the faculty of the Virginia Polytechnic Institute and State University in partial fulfillment of the requirements for the degree of

Doctor of Philosophy
In
Electrical Engineering

Xiaoting Jia, Chair
Anbo Wang
Ting-Chung Poon
Yang Yi
Vinh Nguyen

11/16/2020
Blacksburg, VA

Keywords: triboelectric nanogenerator (TENG), thermal drawing process, 3D printing, power source, self-powered sensor

Wearable Power Sources and Self-powered Sensors Based on the Triboelectric Nanogenerators

Ziang Feng

ABSTRACT

The triboelectric nanogenerator (TENG) has attracted global attention in the fields of power sources and self-powered sensors. By coupling the omnipresent triboelectrification effect and the electrical induction effect, the TENGs can transduce ambient mechanical energy into electrical energy. Such energy could be consumed instantaneously or stored for later use. In this way, they could be deployed distributedly to be compatible power sources in the era of the internet of things (IoTs), completing the powering structure that is currently relying on power plants. Also, the electrical signals can reflect the environment changes around the TENGs. Thus, the TENGs can serve as self-powered sensors in the IoTs. In this work, we adopted two approaches for TENG fabrication: the thermal drawing method (TDP) and 3D printing. With TDP, we have fabricated scalable fiber-based triboelectric nanogenerators (FTENG), which have been woven into textiles by an industrial loom for wearable use. This fabrication process can supply FTENG on a large scale and fast speed, bridging the gap between the TENG and weaving industry. With 3D printing, we have fabricated TENGs that are compatible with the shape of arbitrary substrates. They have been used as biocompatible sensors: human-skin-compatible TENG has been used to recognize silent speech in real-time by sensing the chin movement; the porcine-kidney-shaped fiber mesh has been used to monitor the perfusion rate of the organ. These works have extended the territory of TENGs and can be critical components in the IoTs.

Wearable Power Sources and Self-powered Sensors Based on the Triboelectric Nanogenerators

Ziang Feng

GENERAL AUDIENCE ABSTRACT

Portable electronic devices have become important components in our daily lives, and we are entering the era of the Internet of Things (IoTs), where everyday objects can be interconnected by the internet. While electricity is essential to all of these devices, the traditional power sources are commonly heavy and bulky and need to be recharged or directly connected to the immobile power plants. Researchers have been working to address this mismatch between the device and power systems. The triboelectric nanogenerators (TENG) are good candidates because they can harvest energy in the ambient environment. The users can use them to generate electricity by merely making the rubbing motion. In this work, we report two fabrication methods of the fiber-based triboelectric nanogenerators (FTENG). With the thermal drawing process, we have fabricated sub-kilometer-long FTENG and wove it with the regular cotton yarn into textiles. The wearable power source is human friendly as it does not induce any extra weight load for the user. Besides, we have demonstrated that such long fibers can work as self-powered distributed sensors, such as a Morse code generator. With 3D printing, we have fabricated FTENG-based devices that conform to the working substrates, which can be any shape. We have employed them as biofriendly sensors to translate the chin movement during speaking to language and to monitor the perfusion rate of a pig kidney. The FTENGs have offered excellent comfortability to the users and can play a vital role in reframing the power structure to be compatible with IoTs.

Dedicated to my beloved family and friends

Acknowledgments

During the past few years at Virginia Tech, many people have guided, encouraged, helped, and supported me. Without them, my Ph.D. career could not have been as stimulating and enriching as it was. I would like to take this opportunity to express my sincere thanks to them. First of all, I am indebted and grateful to my advisor Prof. Xiaoting Jia, who offered me the honor to be a member of her research group when I was at my lowest point. Her scientific vision and passion for science inspired me in every aspect of my professional life. Her encouragement directed me to overcome the difficulties and setbacks with confidence. Her excellent management of the group provided me great freedom and flexibility to tackle the tasks. I also would like to thank my committee professors, Dr. Anbo Wang, Dr. Ting-Chuang Poon, Dr. Yang Yi, and Dr. Vinh Nguyen, for their great teaching in the classes and valuable advice on my research.

I would like to send my special thanks to Dr. Lei Zuo and Dr. Blake N. Johnson, who are the main collaborators on my projects. Their exceptional expertise and brilliant ideas brought about the possibility of the collaborations. Besides, I would like to extend my thanks to Drs Yong Xu, Yizheng Zhu, Aimin Yan, Wei Zhou, Yunhui Zhu, Peter H Prideaux, Rui Li, and Guowen Song. They taught me useful knowledge from the underlying physics to the real applications.

I would like to thank my dearest friends and colleagues at CPT, Bo Dong, Lingmei Ma, Dong Wang, Islam Ashry, Qingzhao Kong, Chenyuan Hu, Bo Liu, Peng Lv, Aram Lee, Chennan Hu, Di Hu, Amiya Behera, Zhipeng Tian, Li Yu, Chengshuai Li, Shichao Chen. Thanks also extend to Jiaji He, Shuo Yang, Tong Qiu, Taylor Ray, Shan Jiang, Logan Theis, Zhixing He, Ziling Wu, Yujing Zhang, Jongwoon Kim, Guannan Shi, Meitong Nie, Ruixuan Wang, Jacob Black, Joe

Thomas, Peter Kent, Sixian Jia, and Steven Parker. I enjoyed all the brainstorms, discussions, and cooperations. I could not have experienced such a beautiful academic life without their help and friendship.

I am also grateful to all of my other friends. We not only traveled, partied, played games, worked out together, but also comforted, encouraged, challenged, and pushed each other to be better ones. Their company kept me both mentally and physically healthy. It is an unforgettable memory with them.

I would like to express my deepest gratitude to my parents, X. Feng and F. Meng, and my girlfriend, Y. Wang, who have always been the most loyal supporters. They have always been there to half my sorrow and double my joy. Without their love and care, I cannot achieve what I have done today. Thank you!

Table of Contents

List of Figures

List of Tables

List of Abbreviations

LIB	Lithium-ion battery
SC	Supercapacitor
WSCPS	Wearable self-charging and powering systems
TEG	Thermoelectric generators
PEG	Pyroelectric generators
EMG	Electromagnetic generator
PENG	Piezoelectric nanogenerator
TENG	Triboelectric nanogenerator
IoTs	Internet of Things
TTENG	Textile-based triboelectric nanogenerators
FTENG	Fiber-based triboelectric nanogenerators
CS(TENG)	Contact-separation (triboelectric nanogenerator)
LS(TENG)	Lateral-sliding (triboelectric nanogenerator)
SE(TENG)	Single-electrode (triboelectric nanogenerator)
FT(TENG)	Freestanding triboelectric-layer (triboelectric nanogenerator)
FEM	Finite element method
OC	Open circuit
SC	Short circuit
FOM	Figure-of-merit
TDP	Thermal drawing process

DDR	Draw-down ratio
Cu	Copper
PP	Polypropylene
PC	Polycarbonate
FDM	Fused deposition modeling
SVM	Support Vector Machine

Chapter 1 Introduction

1.1 Wearable Energy Harvesting Devices

Wearable electronic devices have developed significantly in the past few years. They have become smarter and lighter, meaning that more functions are integrated into smaller volumes. The functions have evolved from simple and single ones, such as showing the time only on a traditional watch, to advanced and complex ones, such as sending and receiving messages, displaying images, making phone calls, tracking movements and heartbeats, and showing the time and alarms on a modern watch or wristband. Moreover, fiber-based devices, which can be integrated into clothes, are becoming more and more popular because shirts and pants are more natural to wear than a watch or a strap. Such advancements have profoundly modified our lives in multiple ways, creating more comfortable and convenient living environments and raising the quality of life. [1-3]

One of the critical challenges for wearable electronic devices is to find suitable and sustainable power sources.[4] Currently, portable and wearable devices are commonly employing electrochemical energy-storage devices, e.g., rechargeable lithium-ion batteries (LIBs) and supercapacitors (SCs). However, they can hardly catch up with the developing speed of wearable electronics for the following reasons. Firstly, the consumption of power by electronics is huge and continuous, while the batteries can only provide very limited power and, thus, need frequent recharging. Besides, the electronics are more and more distributed, while the power plants for recharging are commonly immobile. Therefore, the electronic devices can hardly work at their full capacities continuously. Secondly, the widely used materials in batteries or SCs are not comfortable or human-friendly because of their physical properties. For example, the electrodes with inorganic oxide-, phosphate-, or hydroxide-based active materials can hardly be flexible or

stretchable. Also, the energy storage devices are usually heavy and bulky, causing an additional burden for the users. Thirdly, because the chemicals in the batteries or SCs may cause serious potential pollutions to the environment, it is necessary and, however, complicated and costly to take care of or recycle the used batteries and SCs.[5-7]

Currently, there are two strategies to address this awkward mismatch. One is to improve the energy storage devices by increasing the energy density and seeking for user- and environment-friendly materials.[8-12] However, though enormous efforts have been dedicated to this field, the gap between energy usage and storage is still wide.[13] The other one is to search for alternative power supply devices that can meet the requirements of the users. Energy harvesting devices have played a vital role in compensating for the inability of the batteries and SCs. Because they try to convert the ambient energy from various forms, such as solar energy, thermal energy, and mechanical motion to electricity, the recharging process can be realized in the working environment, lowering the dependence on the power plants or even making it unnecessary.[14-17] Also, the materials for these harvesters can be light, soft, flexible, and stretchable, increasing the possibility of integrating them into comfortable clothes and accessories for portable use.[18] Besides, the harvested energy is commonly renewable, providing more sustainability than fossil fuels do. Moreover, some of the energy harvesters can be deployed as self-powered electronic devices, e.g., sensors, which do not need external power sources at all, making the working mechanism more compact and concise. Combining these two strategies, we can look forward to wearable self-charging and powering systems (WSCPS) (Figure 1.1) that aim to make the best use of all forms of energy. The energy harvested can be directly consumed by the electronics or stored in the storage devices for later usage, and the self-powered components will serve themselves.[4, 19]

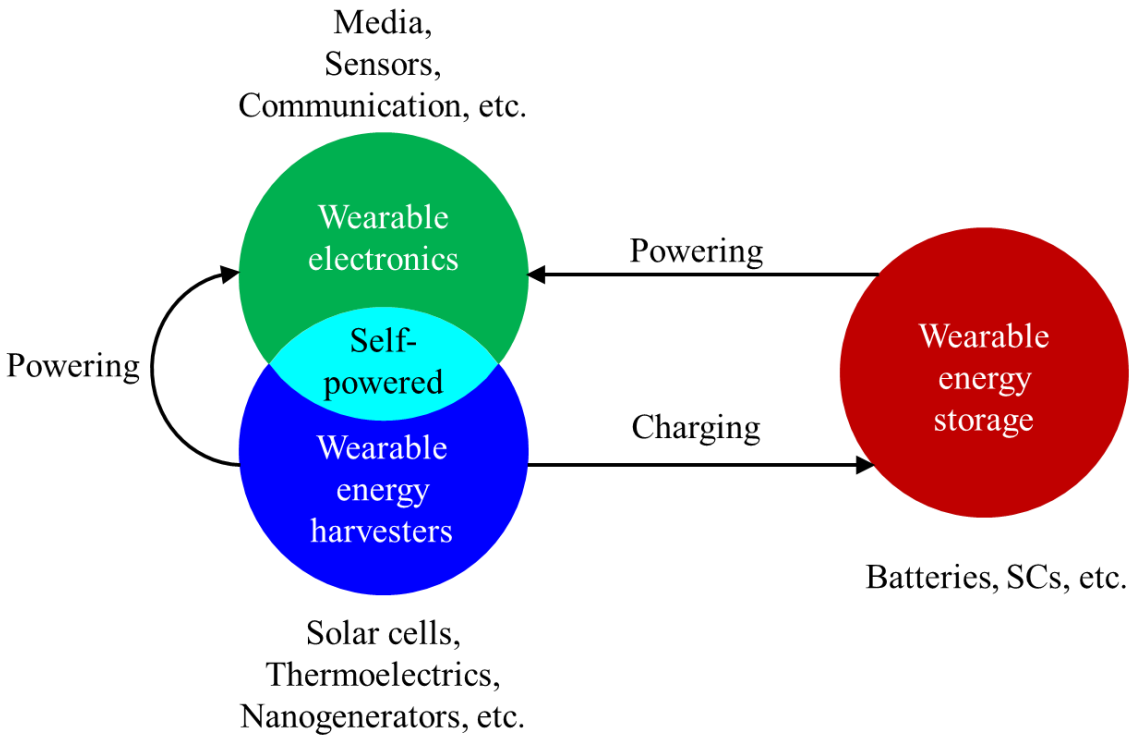

Figure 1.1 Illustration of wearable self-charging and powering system (WSCPS)

The energy harvesters can be fabricated with flexible fiber or textile materials for wearable use[20]. They can be broadly categorized based on the original form of energy. The infinite solar energy from the sunlight can be harvested by solar cells by the photovoltaic effect.[21, 22] Despite the high converting efficiency, it is clear that the performance heavily depends on the availability of light, which can be significantly affected by the season, time, weather, and location.[4] Besides, because of the limited flexibility and low stability of electrodes, the performance is usually much lower than expected.[23] Therefore, the solar cells are expected to increase the immunity to the environment and to find new electrode materials. The thermal energy, which is significant but usually wasted, can be converted into electricity by utilizing either thermoelectric generators (TEG) based on the Seebeck effect or pyroelectric generators (PEG) based on the re-orientation of dipoles

triggered by temperature fluctuations. [15, 24-26] While TEG and PEG can harvest the energy from the body heat as wearable devices, the low efficiency and special geometry or form requirement are problems to be solved for practical applications.[24] Mechanical energy is widely available and has many appearances, such as human motion,[27] vibration,[28] wind,[29] sound,[30] and water waves.[31] Such renewable energy can be converted to electricity via electromagnetic generator (EMG),[32] piezoelectric nanogenerators (PENG),[33] and triboelectric nanogenerators (TENG).[34] The working mechanism of these devices can be explained by Maxwell's equations: the output of EMG is due to the time-varying magnetic field, and the those of PENG and TENG are due to the displacement currents.[4, 35] Because conventional EMGs commonly use heavy and rigid magnets, it is not comfortable to apply them in the wearable electronics.[36] However, PENG and TENG can be fabricated with flexible and light materials, making them good candidates for wearable uses as compensation for the conventional power plants and as distributed sensors. Compared with PENGs, TENGs usually have much more compact structure design, more materials options, more mechanical motion sources, and higher output performance. Therefore, wearable TENGs are expected to play an essential role in the coming epic era of the Internet of Things (IoTs).[37-42]

1.2 Triboelectric Nanogenerators

The concept of triboelectric nanogenerator (TENG) was not carried out until 2012 by the research group led by Prof. Zhong Lin Wang at Georgia Tech.[16] Though the triboelectrification effect has been observed for thousands of years, before then, this ubiquitous phenomenon was commonly regarded more as hazards than as a technique. It can be not only annoying but dangerous. For example, the rubbed clothe may attract small particles, such as dust, which can shorten the lifetime

of usage. Electric signals can be mixed with noises due to the triboelectrification effect between the equipment and the environment. What's more, the high voltage electrostatic discharge can damage electronics, and the sparks between charged surfaces can cause an unintentional fire.[43] However, employed by TENGs and coupled with the electrostatic induction, triboelectrification can lead to displacement current, thus harvesting energy from the mechanical motions.[34, 44, 45]

A typical TENG structure and its working mechanism are shown in Figure 1.2.[16] When driven by external forces, the two middle insulator layers (PET and Kapton) will get into contact, and charges will transfer between them because of triboelectrification. The displacement current occurs when there is relative position change, including vertical separation, lateral sliding, etc. In this way, the mechanical energy is converted to AC currents that flow between the top and bottom conductive layers because of the electrical induction effect. As can be seen in the subsets of Figure 1a, nanostructures (*e.g.*, nanowires and nanoholes), from which the name 'nanogenerator' originates, are usually added to the triboelectric surfaces to enlarge the contact area, thus increasing the number of transferred charges to enhance the performance.[46, 47] However, in the development of TENGs, researchers found that the nanomaterials may be worn off or washed away during use, causing worse and worse output performance. Therefore, TENGs have removed the requirement to include nanostructures: as long as the generator is based on triboelectrification and electrical induction, it can be regarded as a TENG.

TENG has multiple advantages for wearable use. Firstly, the easy availability of triboelectrification, which can occur between any two objects, leads to the vast options of materials. Light, soft, and flexible materials that are comfortable to wear can be used to fabricate TENGs. Secondly, the structure design is simple: contact and relative motion of the triboelectric surfaces are sufficient to generate energy. Thirdly, TENGs can harvest energy from a variety of mechanical

forms, including body motion,[48] vibration,[49] sound,[50] wind,[51] tire rotation,[52] water wave (blue energy),[53] etc. Therefore, their versatility makes it possible to apply TENGs in multiple environments. Besides serving as power sources, TENGs can also be self-powered sensors, which are essential components in the IoTs. The mechanical signals can be converted to electrical ones, such as open-circuit voltage and short-circuit current.[54, 55] When they are deployed on human bodies, a complex of body indices can be collected for health monitoring and analysis while introducing almost no extra burden for the users.

As mentioned above, shirts and pants are the most natural to wear, so textile-based TENGs (TTENG) are drawing more and more attention. As textiles can be categorized as 1D fibers,[56] 2D fabrics,[57] and 3D fabrics[58] based on the fiber orientation and architecture dimensions, TTENGs can be designed and fabricated according to these structures. [59] While textiles can be manufactured with techniques of weaving, knitting, braiding, nonwoven, etc,[60-62] the 1D fiber is the fundamental element of the textiles and can be further processed into higher dimensional structures. Therefore, fiber-based triboelectric nanogenerators (FTENG) are of significant interest.

To be compatible with industrial looms and appropriate to wear, fibers are expected with a few features. Firstly, they should be soft, thin, and flexible enough to stay intact when twisted, squeezed, and crumpled. Secondly, they need to be strong enough to survive the pulling, beating, and stretching forces. Thirdly, the length of the fibers should be at least on ~100 m scale for seamless and large pieces of textiles. Lastly, they should have excellent washability, breathability, and durability for long lifetimes and comfortability. Beyond these basic wearabilities, shape-conformal textiles or meshes are preferred for bio-applications. Therefore, the structure, materials, and fabrication methods of the fibers need to be carefully designed and selected.

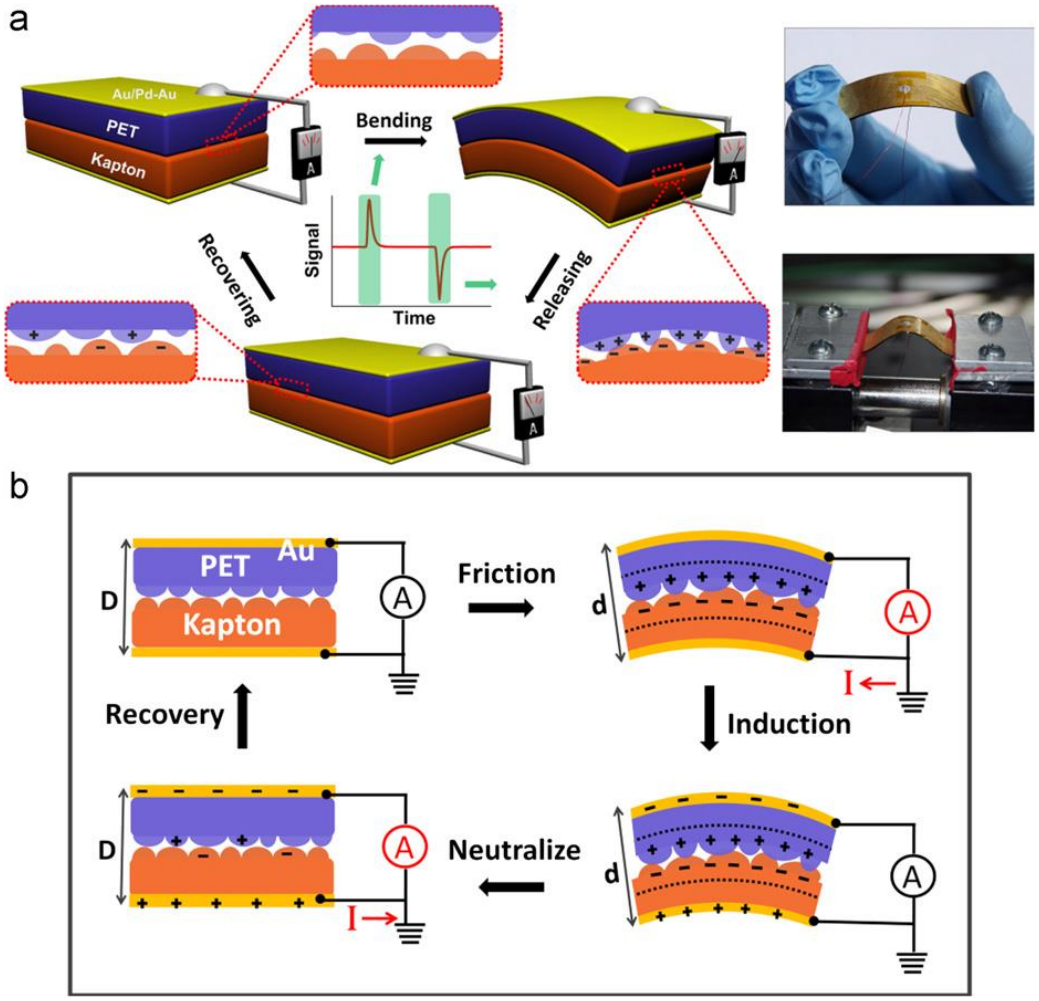

Figure 1.2 Schematic illustration of the structure and working principle of the triboelectric generator. (a) The structure of an integrated generator in bending and releasing process and related electrical measurement tests. Photographic images of a flexible TEG and mechanical bending equipment. (b) Proposed mechanism of a TEG. [16]

1.3 Outline of the Dissertation

In this dissertation, two approaches to fabricate FTENGs are introduced: the thermal drawing method (TDP) and coaxial 3D printing. TDP can provide scalable, washable, and lightweight FTENGs for industrial loom weaving.[56] It is the first time that the versatile TDP is introduced

to the fabrication of FTENG. The diameter of the fiber is down to 350 μm, while the length of a single fiber is up to 200 m. The fabrication speed could reach 4 m min^{-1}. All these features contribute to the excellent weavability of the thermally drawn FTENGs. Both hand-woven and loom-woven textiles were demonstrated, and they can be used as both wearable power sources and self-powered sensors. The coaxial 3D printing can provide shape-conformal FTENG based pads and films.[63] These devices are based on FTENGs, and they enjoy high flexibility and stretchability. Organ conformal TENG self-powered sensors have been demonstrated for silent speech recognization and kidney perfusion monitoring with the help of machine learning techniques.

The dissertation is presented in five chapters. Following this introductory chapter, Chapter Two reviews the fundamentals of the TENG, including the working mechanisms and designs. In Chapter Three, the FTENG is discussed, and the thermal drawing method is introduced to the fabrication of it. The design, fabrication, and performance of the thermally drawn FTENG are presented. In Chapter four, the state-of-the-art conformal TENG devices are briefly reviewed and discussed, and the design, fabrication, and performance of the 3D printed FTENG-based conformal devices are presented. A summary of the works is presented in the last chapter.

Chapter 2 Fundamentals of Triboelectric Nanogenerators

2.1 Theoretical Analysis of TENG

Based on the setup configuration, TENGs are categorized into four working modes: vertical contact-separation (CS) mode,[64-66] lateral sliding (LS) mode,[67-69] single-electrode (SE) mode,[52, 70, 71] and freestanding triboelectric-layer (FT) mode[72-74] (Figure 2.1).[35] The fundamental working mechanism of the TENGs is the coupling of the triboelectric effect and electrostatic induction. Charges will transfer and accumulate on the triboelectric surfaces after the contact of them, and the electrical potential will be changed when their relative position is changed because of the induced charge movement. A continuous AC output can be obtained if electrodes are connected with each other. This qualitative description provides a straightforward explanation of how TENGs converts mechanical energy to electricity.

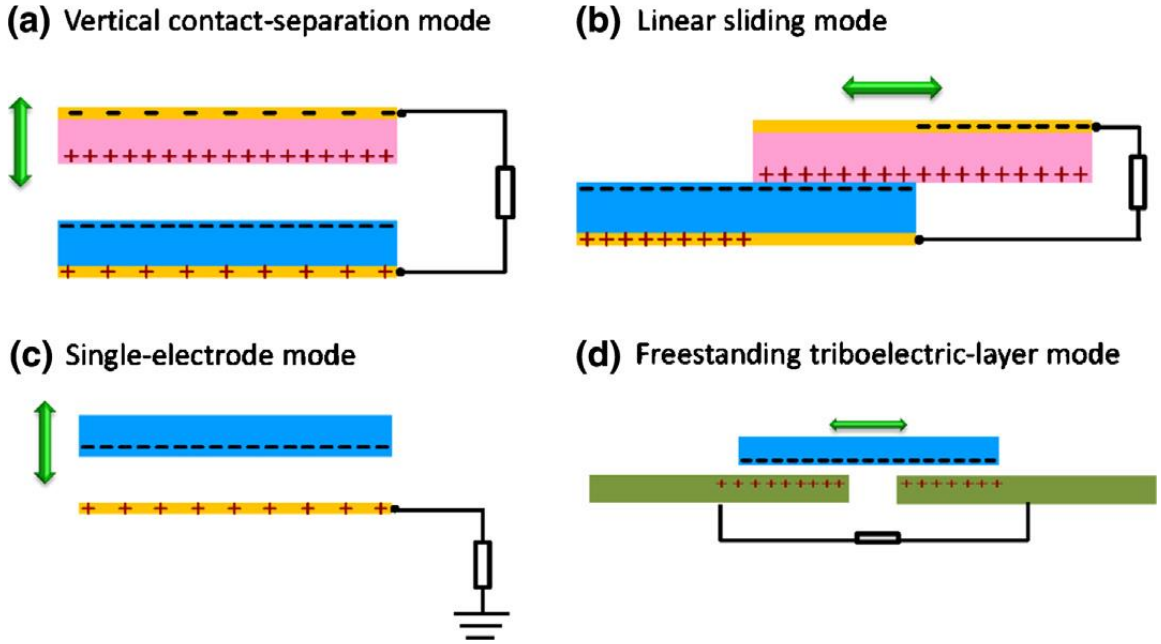

Figure 2.1 The four fundamental working modes of the triboelectric nanogenerators. (a) The vertical contact-separation mode. (b) The lateral-sliding mode. (c) The single-electrode mode. (d) The freestanding mode. [35]

The quantitative explanation was first given by the capacitive model for each working mode.[75-78] Later, Maxwell's displacement current theory was employed to unify the analysis. [35] The results of both methods turned to be equivalent. Here, the capacitive models for each working mode and the displacement current explanation are summarized.

2.1.1 Capacitive Model

For any triboelectric generator, there are charged surfaces. When they are driven by external forces, the distance between them will be changed. This process is analogous to the charging and discharging of a capacitor. The open-circuit voltage ($V_{OC}(x)$) and the electric potential distribution will be dependent on the distance and the amount of transferred charges (Q), and the short-circuit current will be dependent on Q and the speed of the distance change.

If the number of transferred charges is constant at Q, the TENG can be regarded as a typical capacitor. The total voltage difference between the two electrodes is governed by the following equation:[76]

$$V = -\frac{1}{C(x)}Q + V_{\mathrm{OC}}(x) \tag{2.1}$$

where x and C are the distance and the capacitance between the electrodes, respectively. Under short-circuit condition, the following equation can be obtained:[77]

$$0 = -\frac{1}{C(x)}Q_{\mathrm{SC}}(x) + V_{\mathrm{OC}}(x) \tag{2.2}$$

Thus, the fundamental relationship among Q_{SC}, C, and V_{OC} is as follows:[77]

$$Q_{\mathrm{SC}}(x) = C(x)V_{\mathrm{OC}}(x) \tag{2.3}$$

The TENG can thus be modeled as an ideal voltage source and a capacitor connected in series (Figure 2.2).[79]

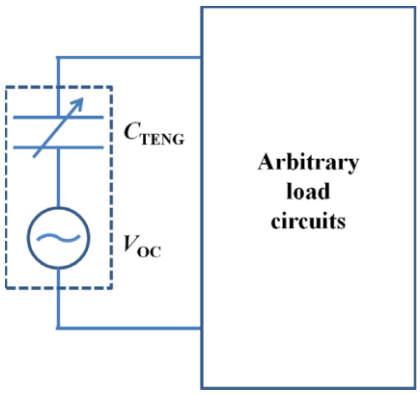

Figure 2.2 Equivalent circuit model of a triboelectric nanogenerator [79]

To quantitatively analyze the *V-Q-x* relationship in TENGs, Niu et al. developed analytical derivation and numerical calculation based on the finite element method (FEM). While analytical derivation is more accurate and preferred, it can only work in limited situations with appropriate approximations. However, the FEM can provide generalized solutions to all types of TENGs.[75-79] In this section, the fundamental capacitive models for each TENG working mode are summarized.

2.1.1.1 Vertical Contact-Separation Mode

There are two typical models of vertical contact-separation triboelectric nanogenerators (CSTENGs) based on the materials of the triboelectric surfaces: dielectric-to-dielectric and conductor-to-dielectric types. They are shown in Figure 2.3(a) and (b), respectively.[75] As can be seen in Figure 2.3(a), there are four layers in the CSTENG: the two dielectrics whose thicknesses are d_1 and d_2 and permittivities are ε_1 and ε_2 are stacked face to face with the same surface areas as *S*, just like a standard parallel capacitor. At the back of them are attached metal

layers as electrodes. The distance x between the two dielectrics can be changed with the external mechanical force. Physical contact between the two middle layers will create oppositely charged surfaces with an equal charge density of σ as the result of electrification, so the amount of transferred charges on the triboelectric surfaces are $\pm\sigma S$. On dielectrics surfaces, uniform distribution and minimal decay of the charges are assumed. When an external force changes x, a potential difference between the two electrodes will be induced. The transferred charge amount between the two electrodes is defined as Q.[75] The model for conductor-to-dielectric type CS TENG can be similarly established (Figure 2.3(b)). The difference is that the amounts of charges on metal 1 and dielectric 2 are $S\sigma$-Q and Q, respectively.

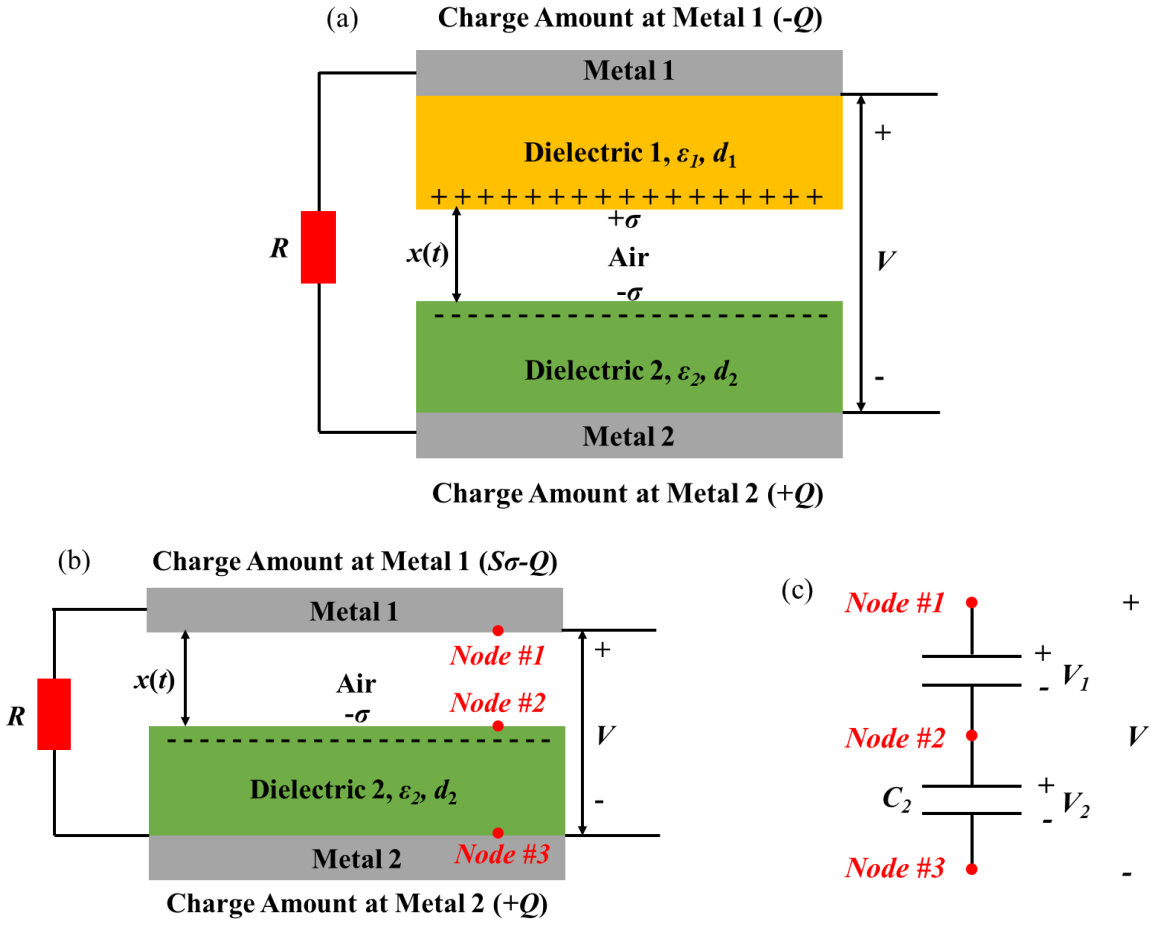

Figure 2.3 Theoretical models for a) dielectric-to-dielectric vertical CSTENG and (b) conductor-to-dielectric vertical CSTENG. (c) Equivalent circuit diagram for (b). [75]

With the model in Figure 2.2(a), the following equations can be obtained from the Gauss theorem:

$$E_1 = -\frac{Q}{S\varepsilon_1} \tag{2.4}$$

$$E_2 = -\frac{Q}{S\varepsilon_2} \tag{2.5}$$

$$E_{air} = -\frac{-\frac{Q}{S} + \sigma(t)}{\varepsilon_0} \tag{2.6}$$

where S is the area size, E_1 is the electric field in dielectric 1, E_2 is the electric field in dielectric 2, E_{air} is the electric field in the air gap between the two dielectrics, and ε_0 is the dielectric constant in the vacuum. The voltage between the two metal layers can be expressed as follows:

$$V = E_1 d_1 + E_2 d_2 + E_{\text{air}} x \tag{2.7}$$

Plugging in Eq. 2.4 - 2.6 into equation 2-7, we have the *V*-*Q*-*x* relationship:

$$V = -\frac{Q}{S}\left(\frac{d_1}{\varepsilon_1} + \frac{d_2}{\varepsilon_2} + \frac{x(t)}{\varepsilon_0}\right) + \frac{\sigma x(t)}{\varepsilon_0} \tag{2.8}$$

Similarly, the *V*-*Q*-*x* relationship for conductor-to-dielectric CSTENG can be expressed as follows:

$$V = -\frac{Q}{S}\left(\frac{d_2}{\varepsilon_2} + \frac{x(t)}{\varepsilon_0}\right) + \frac{\sigma x(t)}{\varepsilon_0} \tag{2.9}$$

It is apparent that Eq. 2.9 is the same as Eq. 2.8 when d_1 is 0. With the definition of relative effective thickness:

$$d_0 = \sum_{i=1}^{n} \frac{d_{\text{i}}}{\varepsilon_{\text{ri}}/\varepsilon_0} \tag{2.10}$$

The *V*-*Q*-*x* relationship can be unified as follows:

$$V = -\frac{Q}{S\varepsilon_0}\left(d_0 + \frac{x(t)}{\varepsilon_0}\right) + \frac{\sigma x(t)}{\varepsilon_0} \tag{2.11}$$

There are two extreme conditions: open-circuit (OC) and short-circuit (SC). In the OC condition, no charge is transferred between the two electrodes, meaning that Q is 0. In the SC condition, V is

0. Therefore, the open-circuit voltage, transferred charges between electrodes, and the short-circuit current can be obtained as follows:[75]

$$V_{\mathrm{OC}} = \frac{\sigma x(t)}{\varepsilon_0} \tag{2.12}$$

$$Q_{\mathrm{SC}} = \frac{S\sigma x(t)}{d_0 + x(t)} \tag{2.13}$$

$$I_{\mathrm{SC}} = \frac{dQ_{\mathrm{SC}}}{dt} = \frac{S\sigma d_0}{(d_0 + x(t))^2}\frac{dx}{dt} = \frac{S\sigma d_0 v(t)}{(d_0 + x(t))^2} \tag{2.14}$$

The *V*-*Q*-*x* relationship can also be derived from the detailed electrostatic induction mechanism, which could provide the fundamental working principles of the TENGs. The nodes, which correspond to equipotential volumes, are shown in Figure 2.2(c). Though every two nodes can form a capacitor, Node 1 and 3 are blocked by Node 2, and, thus, there are only two capacitors in the system. Under the short-circuit condition, Node 1 and Node 3 are connected and hence have the same potential. From charge conservation and Kirchhoff's Law, Q_{Node3} can be obtained as follows:

$$Q_{\mathrm{Node3}} = \frac{\sigma S}{1 + \frac{C_1(x)}{C_2(x)}} \tag{2.15}$$

Therefore, Q_{SC} can be obtained by subtracting the transferred charge with $Q_{\mathrm{Node3}}(x = 0)$:

$$Q_{\mathrm{SC}} = \frac{\sigma S}{1 + \frac{C_1(x)}{C_2(x)}} - \frac{\sigma S}{1 + \frac{C_1(x=0)}{C_2(x=0)}} \tag{2.16}$$

With the parallel-plate capacitor properties, Eq. 2.12 - 2.14 can be obtained. It is clear that the change of the C_1/C_2 ratio, which is induced by the relative position change of the two triboelectric surfaces, is the underlying physics of the working mechanism of the CSTENG.[75]

Based on the theories above, the output characteristics of the CSTENG can be summarized as follows. V_{OC} is linearly proportional to the separation distance *x*, while the capacitance is inversely proportional to *x*. Q_{SC} will reach 90% of the saturation value (σS) when *x* changes from 0 to $10d_0$.

I_{SC} is dependent on Q_{SC} and dx/dt. If x is already comparable to the size of the device, the edge effect will dominate the performance, meaning that V_{OC} and Q_{SC} will no longer follow the linearity relationship with x.[75] However, x is usually much smaller than the device size for stability. The typical structures will be reviewed in Section 2.3.

2.1.1.2 Lateral-sliding Mode

Similar to the CS TENG, the lateral sliding triboelectric nanogenerators (LSTENG) has two typical models, which are shown in Figure 2.4.[69] It is assumed that the length and width are much larger than the dielectric thickness so that the edge effect can be ignored. The parameters in the LSTENG models are similar to those of the CSTENG. Instead of moving vertically, the surfaces move laterally to induce changes in electrical potential.

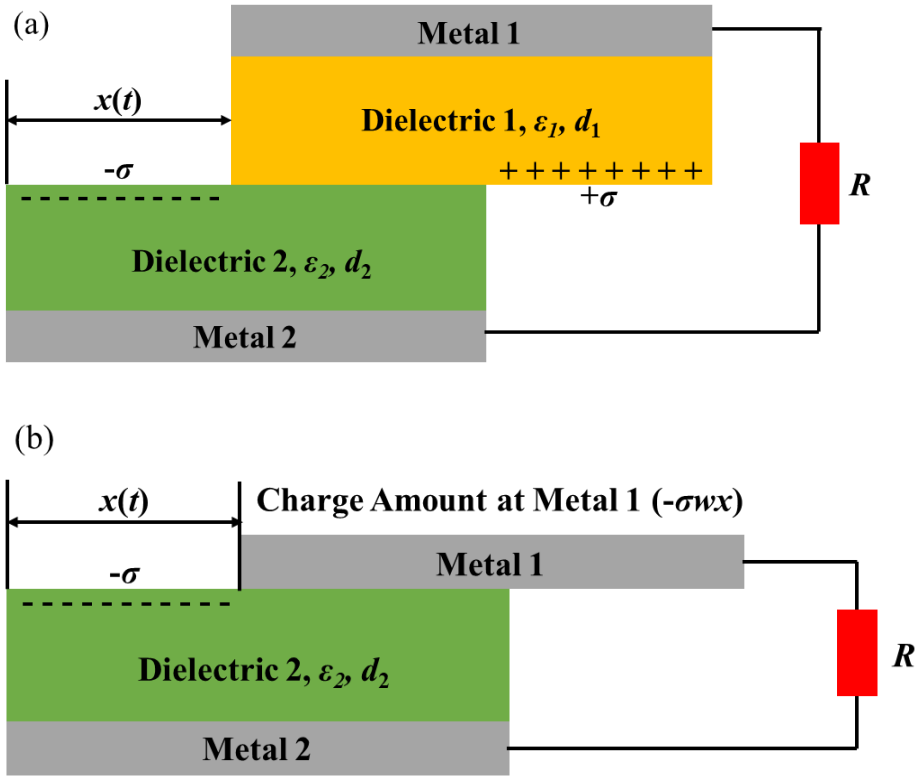

Figure 2.4 Theoretical models for (a) dielectric-to-dielectric LSTENG and (b) conductor-to-dielectric LSTENG [69]

In these models, x represents the separation distance, and l is the length of the surfaces. When l is much larger than d_1 and d_2, and x is always smaller than $0.9l$, an approximate analytical V-Q-x relationship is obtained by neglecting the edge effects.

$$V = -\frac{d_0}{w(l-x)}Q + \frac{\sigma d_0 x}{\varepsilon_0 (l-x)} \tag{2.17}$$

where w is the width of the surfaces, and d_0 is the effective dielectric thickness. V_{OC} can be expressed as follow:

$$V_{OC} = \frac{\sigma x}{\varepsilon_0 (l-x)}\left(\frac{d_1}{\varepsilon_1} + \frac{d_2}{\varepsilon_2}\right) \tag{2.18}$$

The output characteristics of the LS TENG can be summarized as follows. Q_{SC} is linearly proportional to the separation distance x, while the capacitance is inversely proportional to $(l - x)$. Q_{SC} will dramatically increase when x is close to l due to the quick decrease of the capacitance.[69] The edge effect can usually be neglected in these one-unit LSTENGs. However, in grating LS TENGs, an advanced type of LS TENG that comprises of many one-unit LSTENGs, the edge effect needs to be taken into consideration.[80-82]

2.1.1.3 Single-electrode Mode

Because the two types of single electrode triboelectric nanogenerator (SETENG), contact mode and sliding mode, show almost same characteristics, the theoretical analysis for the contact mode is summarized here.[34] The conductor-to-dielectric contact mode SE TENG and the equivalent circuit model are shown in Figure 2.5.

The length and the width of the triboelectric surfaces are l and w, respectively. The thicknesses of the Dielectric 1 and metal electrode (primary electrode) are d_1 and d_m, respectively. The reference electrode is located under the primary electrode with a distance of g. While the two electrodes are fixed, Dielectric 1 can be moved by mechanical actuation, and the distance between it and the

primary electrode is *x*. After contact triboelectrification, the charge density on the surfaces are ±σ, as shown in Figure 2.5(a).[77]

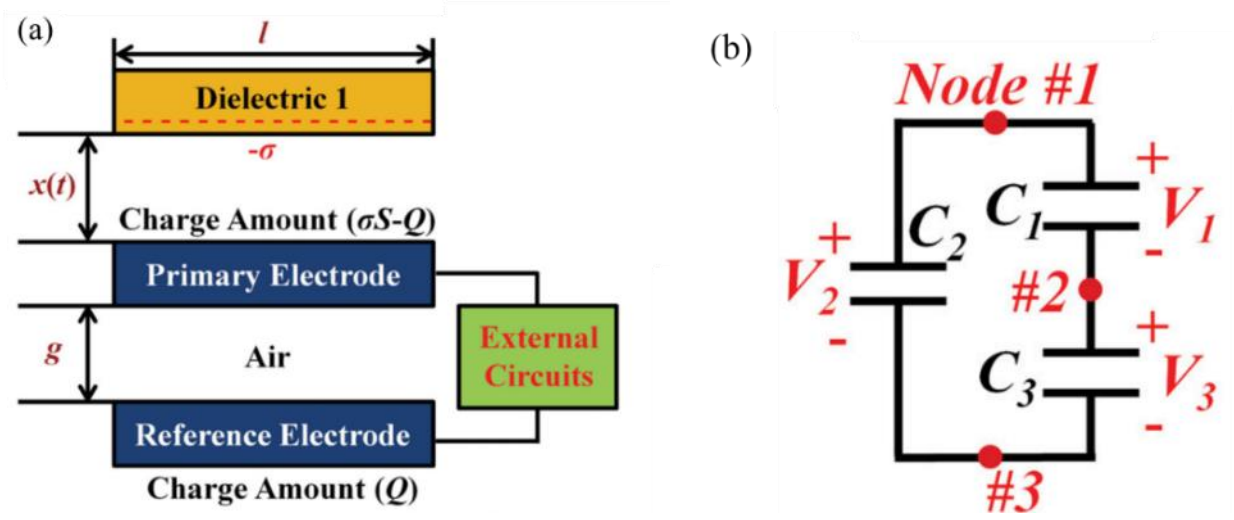

Figure 2.5 (a) Theoretical models and (b) equivalent circuit model for conductor-to-dielectric SETENG [77]

The numerical calculation of SE TENG shows that its characteristics are completely different from the CSTENG. Firstly, the capacitance of SETENG is almost a constant with the increase of *x* because of the immobile electrodes, while the capacitance changes significantly with *x* in CSTENG. Secondly, in SE TENG, V_{OC} saturates at a much smaller x than it does in CSTENG. The reason is that when Dielectric 1 moves away from the electrodes, its impact on the potential distribution around them decreases significantly. Thirdly, in SE TENG, Q_{SC} slowly saturates at only $Q/2$ because Q is almost evenly allocated to the two electrodes. Besides, the degradation of output performance of SE TENG mainly originates from the electrostatic shield effect of the primary electrode, and the edge effect also needs to be taken into consideration when *w* is small.[77]

However, the model in Figure 2(a) assumes that all three components have the same area size and the two electrodes have the same volume. In practice, Dielectric 1, which may be precharged, can be much bigger than the electrodes, and the reference electrodes can be much bigger than the

primary electrode. Thus, when x is large, Dielectric can still have a huge impact on the potential distribution around the electrodes, and Q_{SC} can saturate at Q.

2.1.1.4 Freestanding Triboelectric-layer Mode

Two typical free-standing triboelectric layer triboelectric nanogenerators (FTTENG) are shown in Figure 2.6. In the dielectric FTTENG (Figure 2.6(a)), the free-standing materials contain dielectrics only, and in the dielectric and metal FTTENG (Figure 2.6(c)), the free-standing materials contain both dielectric and metals. Because the working principles of them are very similar, the analysis for the former is summarized here. The equivalent circuit model of the dielectric FTTENG is shown in Figure 2.6(b). [78]

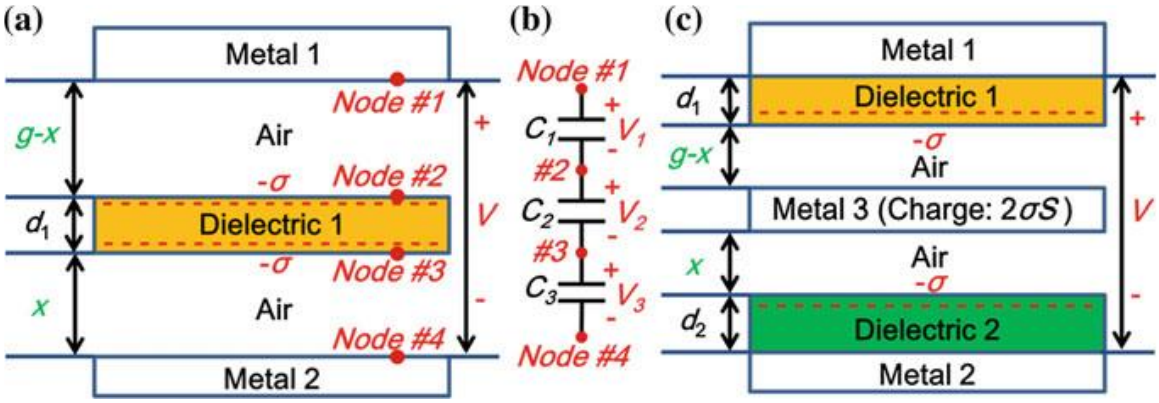

Figure 2.6 Theoretical models of FTTENGs (a) model of a typical dielectric freestanding layer CFTENG. (b) equivalent circuit model of the dielectric FTTENG electrostatic system. (c) model of a typical metal freestanding layer FTTENG. [78]

In practice, the effective dielectric thickness is negligible compared with the air gap. Therefore, the charges on metal 1 and 2 can be approximated as follows:

$$Q_1 \approx \frac{2\sigma S}{1+\frac{C_3}{C_1}} \tag{2.19}$$

$$Q_2 \approx \frac{2\sigma S}{1+\frac{C_1}{C_3}} \tag{2.20}$$

The working mechanism of the FTTENG is based on the change of C_1 and C_3 due to the external mechanical actuation. The short-circuit current and open-circuit voltage can be calculated as follows:

$$Q_{SC} = Q_1(x) - Q_1(x = 0) = \frac{2\sigma S x}{d_0 + g} \tag{2.21}$$

$$V_{OC} = \frac{2\sigma x}{\varepsilon_0} \tag{2.22}$$

The *V*-*Q*-*x* relationship can thus be obtained as follow:

$$V = -\frac{1}{C}Q + V_{OC} = -\frac{d_0 + g}{\varepsilon_0 S}Q + \frac{2\sigma x}{\varepsilon_0} \tag{2.23}$$

This type of FTTENG is like a stacked model of the CFTENG. However, in FTTENG, the inherent capacitance is constant and independent of *x*, and Q_{SC} is linearly proportional to *x*. This linearity makes it ideal for converting the mechanical vibration signals to electrical signals.[78]

2.1.2 Displacement Current Analysis

In 2017, Wang unified the explanation for all modes of TENGs with Maxwell's displacement current.[35] The Ampere's circuital law with Maxwell's addition presented as follows:[83]

$$\nabla \times \boldsymbol{H} = \boldsymbol{J}_f + \frac{\partial \boldsymbol{D}}{\partial t} \tag{2.24}$$

where $\boldsymbol{H}$ is the magnetizing field, $\boldsymbol{J}_f$ is the free electric current density, and $\boldsymbol{D}$ is the displacement field. $\boldsymbol{D}$ can be further expanded as follows:

$$\boldsymbol{D} = \varepsilon_0 \boldsymbol{E} + \boldsymbol{P} \tag{2.25}$$

where ε_0 is the permittivity in the vacuum, and $\boldsymbol{P}$ is the polarization field. In equation 2.24, the second term is Maxwell's displacement current that is defined as follow:

$$\boldsymbol{J}_D = \frac{\partial \boldsymbol{D}}{\partial t} = \varepsilon_0 \frac{\partial \boldsymbol{E}}{\partial t} + \frac{\partial \boldsymbol{P}}{\partial t} \tag{2.26}$$

where $\boldsymbol{E}$ is the electric field.

With the example of the classic four-layer CSTENG (Figure 2.7), the displacement current that corresponds to the TENG model is as follow:

$$\boldsymbol{J}_D = \frac{\partial \boldsymbol{D}_z}{\partial t} = \frac{\partial \sigma_1(z,t)}{\partial t} = \sigma_c \frac{dz}{dt} \frac{d_1\varepsilon_0/\varepsilon_1 + d_2\varepsilon_0/\varepsilon_2}{[d_1\varepsilon_0/\varepsilon_1 + d_2\varepsilon_0/\varepsilon_2 + z]^2} \tag{2.27}$$

where σ_C is the surface charge density on the dielectric surface, $\sigma_1(z,t)$ is the charge density on the top electrode, which is a function of the gap distance $z(t)$. This equation shows that the displacement current density is proportional to the charge density on the dielectric surface and the speed of the mechanical movement. A similar analysis can also be established for other modes of TENGs.

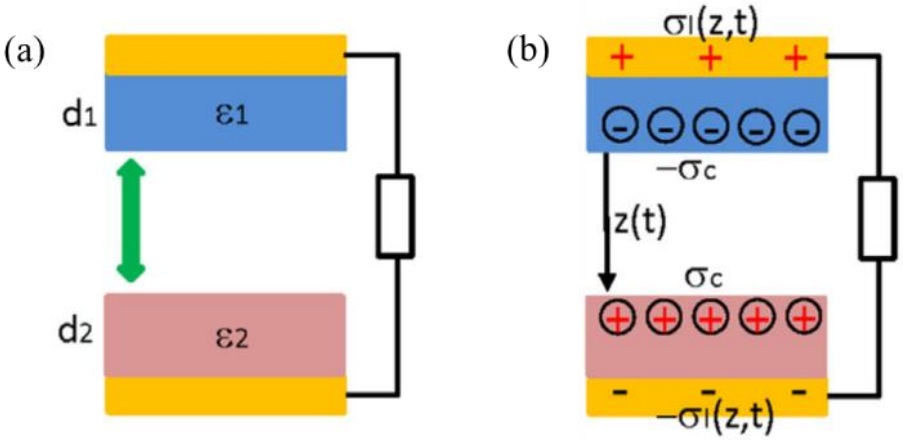

Figure 2.7 Illustrations about the working mechanisms of TENG
(a) Original state (b) after contact and separation [83]

2.1.3 Discussion

In this section, the fundamental working mechanisms of the four modes of TENGs are summarized. It is worth noting that tens of types of TENGs have been designed based on these basic structures.[34] The device can comprise of a single or multiple TENG units, which can work in different modes.[74, 84, 85] To establish a standard to evaluate the performance of the TENGs, Zi

et al. have reported the figure-of-merits (FOM) for TENGs, which is composed of a structural FOM and a material FOM. [86]

Numerical simulations were conducted for the structural FOM, and the result is as follows:

$$FS > CS > LS > SE \tag{2.28}$$

In the simulations, the same surface charge density and area were set in all the modes. In practice, the working environments also need to be taken into consideration. For example, in the SE mode, the transferred charge can only reach $Q/2$ because the primary and reference electrodes were set to have the same size. However, a much larger reference electrode can be employed to allow the transferred charge to be just slightly than Q, therefore substantially improving the output performance.[86] Besides, modes with higher structural FOM may suffer from limited x_{max}, so the output cannot be optimized. Therefore, the working mode needs to be carefully designed according to the real application.

The charge density σ of the triboelectric surface is the only material-related parameter in the performance figure-of-merit. The output performance will be significantly enhanced if σ is optimized because the performance is proportional to σ^2.[86] There are two typical approaches to optimize σ. Firstly, introducing nanostructures on the triboelectric surfaces can enlarge the contact area, thus offering more potential charges for transferring. Secondly, the tendencies of materials to gain or lose electrons have been quantitatively tested and listed in a triboelectric series (Table 2.1). [87] Under the same condition, if the two contacted materials are more separated in the series, more charges will be transferred between them. Ideally, the two triboelectric surfaces are made of materials that are located at the two ends of the triboelectric series. In practice, there are several other properties to consider when selecting materials for wearable devices, including flexibility, breathability, stretchability, scalability, cost, weight, softness, fabrication complexity and speed.

Table 2.1 Triboelectric series of materials and their triboelectric charge density (TECD)[87]

Materials	Abbr.	Average TECD ($\mu C\ m^{-2}$)	STDEV
Chemical-Resistant Viton® Fluoroelastomer Rubber		−148.20	2.63
Acetal		−143.33	2.48
Flame-retardant garolite		−142.76	1.49
Garolite G-10		−139.89	1.31
Clear cellulose		−133.30	2.28
Clear polyvinyl chloride	PVC	−117.53	1.31
Polytetrafluoroethylene	PTFE	−113.06	1.14
Abrasion-resistant polyurethane rubber		−109.22	0.86
Acrylonitrile butadiene styrene	ABS	−108.07	0.50
Clear polycarbonate (Glossy)	PC	−104.63	1.79
Polystyrene	PS	−103.48	2.48
Ultem polyetherimide	PEI	−102.91	2.16
Polydimethylsiloxane	PDMS	−102.05	2.16
Polyester fabric (Plain)		−101.48	1.49
Easy-to-machine electrical-insulating garolite		−100.33	1.79
Food-grade high-temperature silicone rubber		-94.03	0.99
Polyimide film	Kapton	-92.88	2.58
DuraLar polyester film	PET	-89.44	0.86
Polyvinylidene fluoride	PVDF	-87.35	2.06
Polyetheretherketone	PEEK	-76.25	1.99
Polyethylene	PE	-71.20	1.71
High-temperature silicone rubber		-69.95	0.50
Wear-resistant garolite		-68.51	1.99
Low-density polyethylene	LDPE	-67.94	1.49
High impact polystyrene		-67.37	1.79
High-density polyethylene	HDPE	-59.91	1.79
Weather-resistant EPDM rubber		-53.91	0.99
Leather strip (Smooth)		-53.61	1.31

Table 2.1 continued

Oil-filled cast nylon 6		-52.75	0.99
Clear cast acrylic	PMMA	-49.59	1.31
Silicone		-48.73	1.49
Abrasion-resistant SBR rubber		-47.30	1.31
Flexible leather strip (Smooth)		-40.13	0.86
Noryl polyphenyl ether		-34.40	0.86
Poly(phenylene Sulfide)	PPS	-31.82	0.86
Pigskin (Smooth)		-30.10	0.86
Polypropylene	PP	-27.23	1.31
Slippery nylon 66		-26.09	0.50
Weather- and chemical-resistant santoprene rubber		-25.23	0.50
Chemical- and steam-resistant aflas rubber		-22.65	1.31
Polysulfone		-18.92	0.86
Cast nylon 6		-18.35	0.99
Copy paper		-18.35	0.50
Chemical-resistant and low-temperature fluorosilicone rubber		-18.06	0.86
Delrin® Acetal Resin		-14.91	0.50
Wood (marine-grade plywood)		-14.05	0.99
Wear-resistant slippery garolite		-11.47	0.50
Super-stretchable and abrasion-resistant natural rubber		-10.61	0.50
Oil-resistant buna-N rubber		2.49	0.23
Food-grade oil-resistant buna-N/vinyl rubber		2.95	0.13

Note: STDEV refers to the standard deviation.

2.2 Typical Structures of TENG

2.2.1 Vertical Contact-Separation Mode

As described in section 2.1.1.1, the two electrodes need to be connected via an external circuit in the CSTENGs. This requirement could be a double-edged sword. It ensures the device's compactness. However, the separation distance between the triboelectric surfaces is also limited, thus limiting the output performance. Therefore, CSTENGs are best to be deployed in places where the separation amplitude is already limited, e.g., the insoles. Currently, the separations in CSTENGs are generally realized by spacers.

A typical spacer-based CSTENG is shown in Figure 2.8(a).[88] The spacer is placed at the edges between the two triboelectric surfaces, so they can contact each other when there is pressure and separate when the pressure is released. Because the rigid spacer is not flexible enough, x_{max} is limited by the thickness of the spacer and the elasticity of the triboelectric materials. The spring spacers were employed to enlarge x_{max}. As can be seen in Figure 2.8(b), the conventional spacer is replaced with four springs at the corners.[89] The elasticity of the springs makes x_{max} much longer than the thickness of the squeezed springs. This elasticity can also come from the triboelectric materials, and with this advantage, the spacing can come from the well-designed structure. An arch-shaped CSTENG and porous material-based CSTENG are shown in Figure 2.8(c) and (d), respectively.[90, 91] Besides these single units of CSTENGs, multiple units can be stacked up to scale up the output of the CSTENGs (Figure 2.8 (e)).[92]

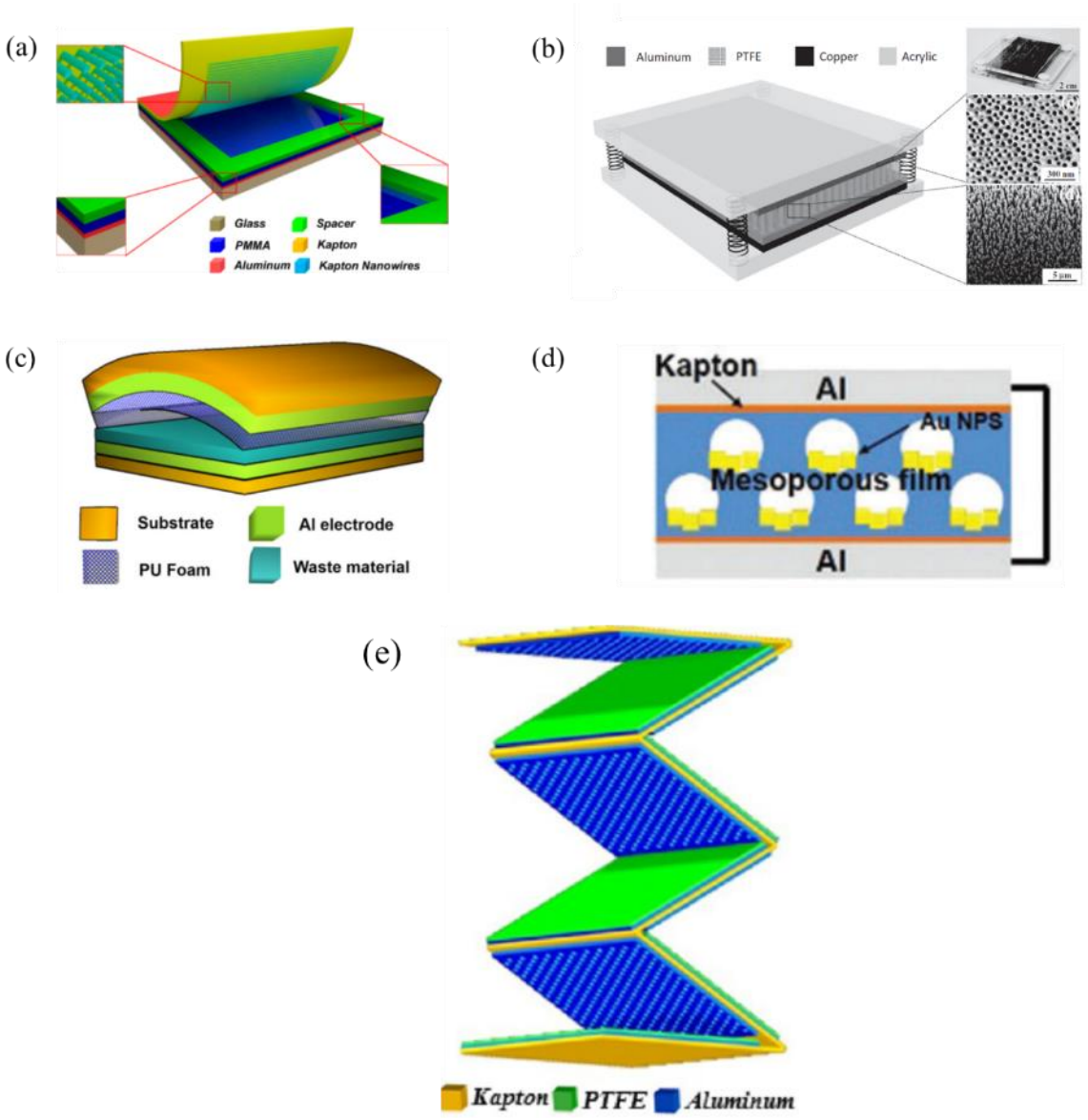

Figure 2.8 Typical vertical contact-separation mode TENGs. (a) Typical spacer based CSTENG (b) spring spacer-based CSTENG (c) arch-shaped CSTENG (d) porous material-based CSTENG (e) multilayered CSTENG [88-92]

2.2.2 Lateral-sliding Mode

While the LSTENGs aim to harvest energy that drives the device moving in the lateral direction, they can have the same structures as the CSTENG or the SETENG (Figure 2.9).[69, 93] Compared with the CSTENG, LSTENG does not need the spacer to maintain the gap between two triboelectric surfaces, making the device more compact.

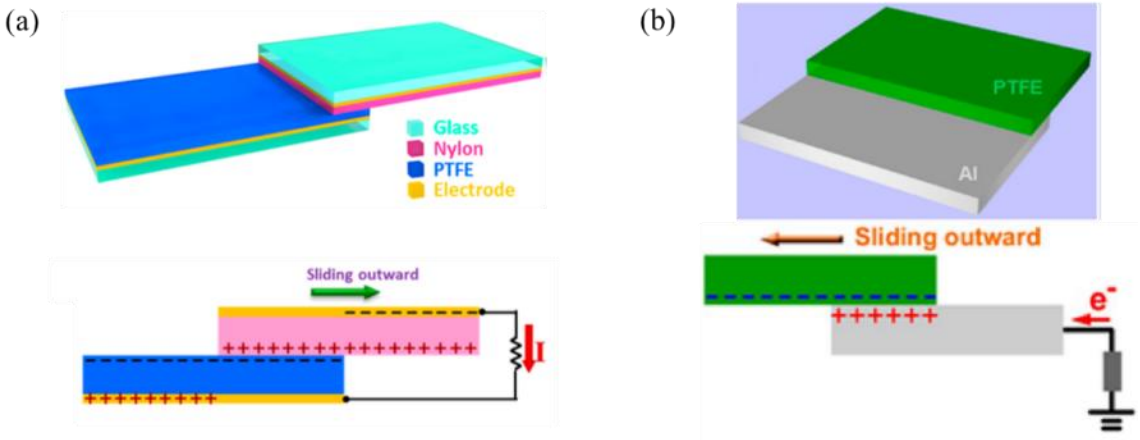

Figure 2.9 Basic lateral-sliding mode TENGs. (a) CSTENG with lateral movement (b) SETENG with lateral movement [69, 93]

Similar to the CSTENG, LSTENG can also be scaled up by integrating multiple units to enhance output performance. There are multiple approaches to realize integration. Firstly, the LSTENGs can be stacked up to enlarge the device area (Figure 2.10(a)).[94] Secondly, the LSTENGs can be aligned in-plane, forming a linear grating (Figure 2.10(b)).[82] Thirdly, the LSTENGs can be aligned circularly, forming a disk or cylinder grating (Figure 2.10(c) and (d)).[95, 96] The edge effect will help to enhance the output in these LSTENG gratings.

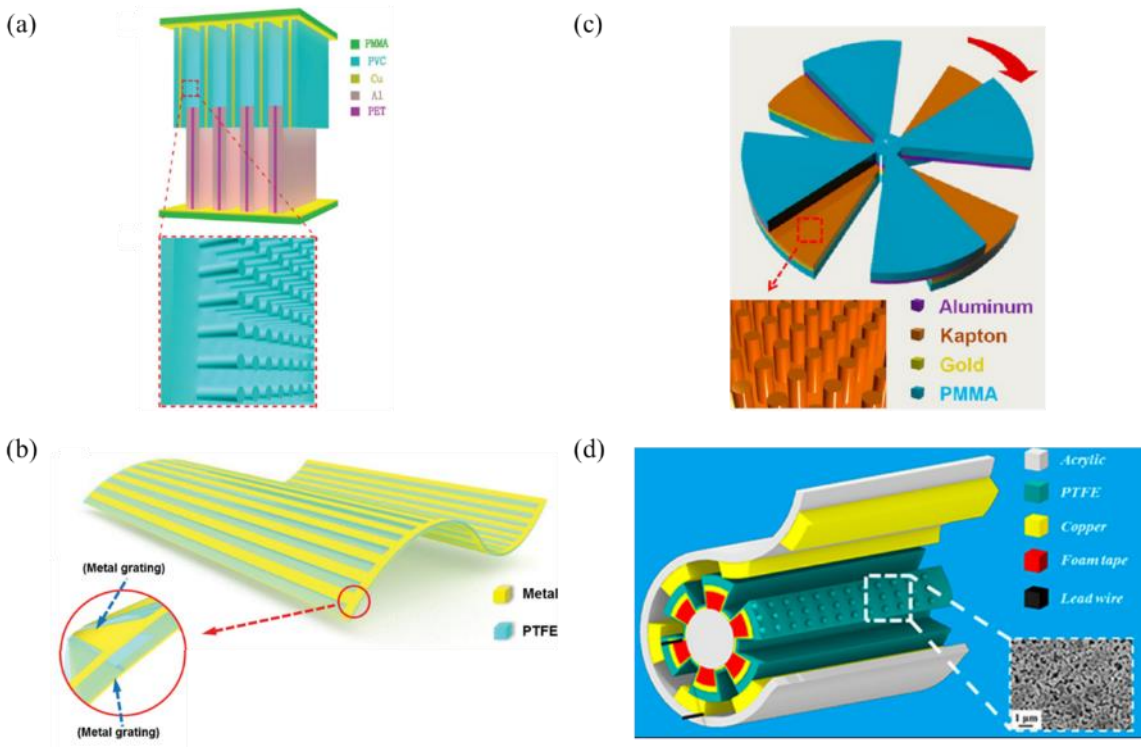

Figure 2.10 Advanced lateral-sliding mode TENGs (a) stacked-up LSTENGs (b) SETENG with lateral movement (c) rotational disk-shaped LSTENG circular gratings (d) rotational cylindrical LSTENG circular gratings [82, 94-96]

2.2.3 Single-electrode Mode

The SETENG structure can be as simple as a piece of a conductor. As can be seen in Figure 2.11(a), the SETENG only consists of a piece of metal, which serves as both one of the triboelectric surfaces and the electrode. The motions of the moving object will induce currents flowing between the metal and the ground back and forth. It is worth noting that the moving object is not connected to the fixed part of the device in this mode, thus allowing more freedom of the movement and more applications. Most of the SETENGs are based on this simple structure with leakage protection, advanced materials for stronger electrification, and additional functionalities.

One typical approach to preventing current leakage is by covering the conductor with insulators. As shown in Figure 2.11(b), the aluminum electrode is sandwiched by a paper layer and a PTFE layer.[97] Because PTFE can obtain electrons easily via friction, it is regarded as a good triboelectric material for excellent output performance. Similarly, in Figure 2.11(c) and (d), the electrodes are either attached to or shielded by insulators.[98, 99] These different shapes, namely plane, arch, and sphere, aim to harvest different forms of mechanical energies, *i.e.*, pressure, squeezing, and vibration. Many more devices have been developed with similar strategies.[70, 71, 100-104]

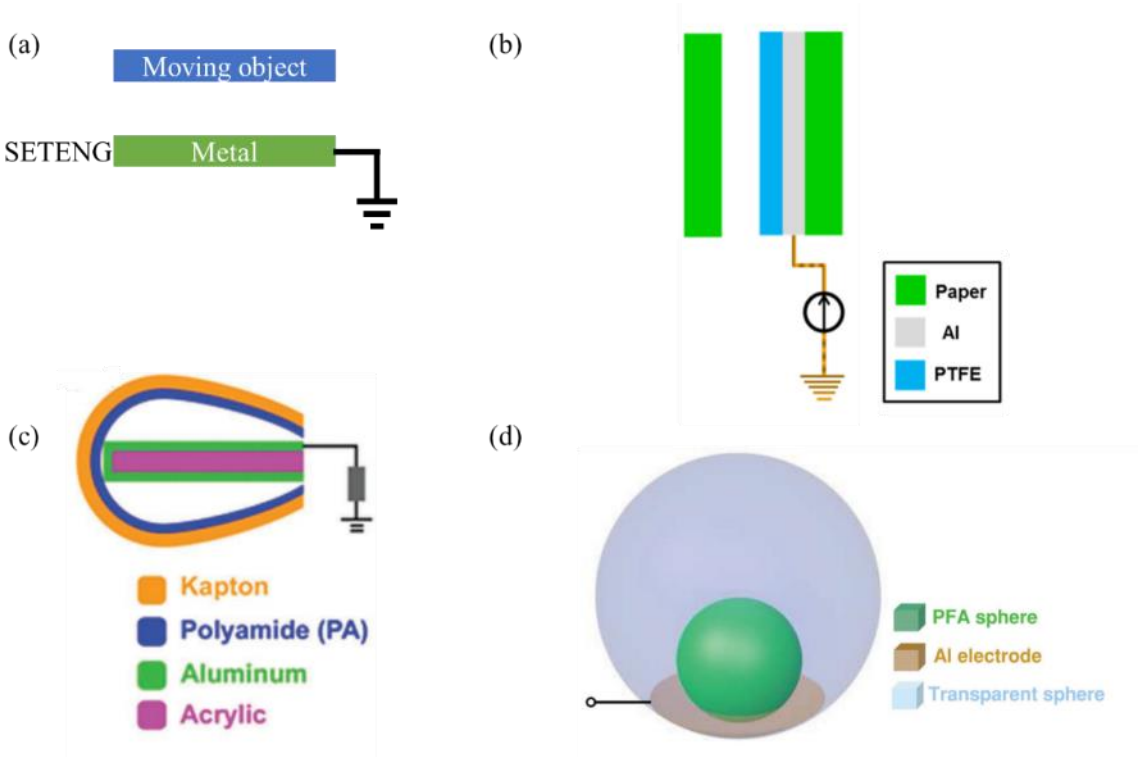

Figure 2.11 Basic single-electrode mode TENGs (a) SETENG that has only a layer of conductor (b) SETENG with planar shields (c) SETENG with planar and arch shields (d) SETENG with spherical shields. [97-99]

It is worth noting that the moving object can either be included in the SETENG or not. When it is not a part of the device, it is changeable, meaning multiple materials or objects can be used for energy harvesting. For example, in Figure 2.12(a), the counter object can be multiple materials, e.g., dialysis cellulose membrane and human skin.[105] This strategy has been employed by many devices, especially in wearable devices, because it is friendly to users by giving them more options to wear. In Figure 2.12(b), the cotton cloth can be changed to other materials, such as nylon, acrylic, and polyethylene, which are common materials for textiles and are more positive than PTFE in the triboelectric series.[106] In Figure 2.12(c), the device can still work if there is a glove on the hand because contact electrification will occur between the glove (leather/cotton) and the graphene oxide.[107]

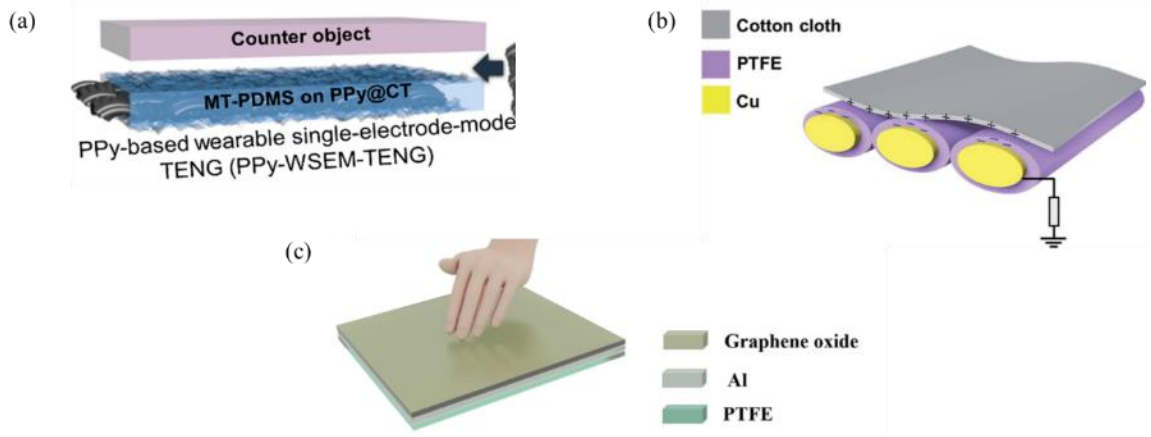

Figure 2.12 SETENGs with a changeable moving object (a) and (b) textile-based SETENGs (c) film-based SETENG [105-107]

2.2.4 Free-standing Mode

Similar to the CSTENG, the FSTENG also has two connected electrodes. However, the moving object is not attached to either of them, thus improving the convenience of fabrications and operations.[34] Because the relative position of the electrodes is fixed, the mechanically driven free-standing object can create electrical potential changes in the electrodes, leading to currents flowing between them back and forth.

As can be seen in Figure 2.13(a) and (b), the electrodes in the FSTENGs can be put side by side or parallelly.[108, 109] The free-standing layers move laterally or vertically to generate the currents. However, the moving direction of the free-standing layer is not limited to these directions (Figure 2.13(c) and (d)).[110, 111] Movement in random directions can also result in currents because of the potential change they created.

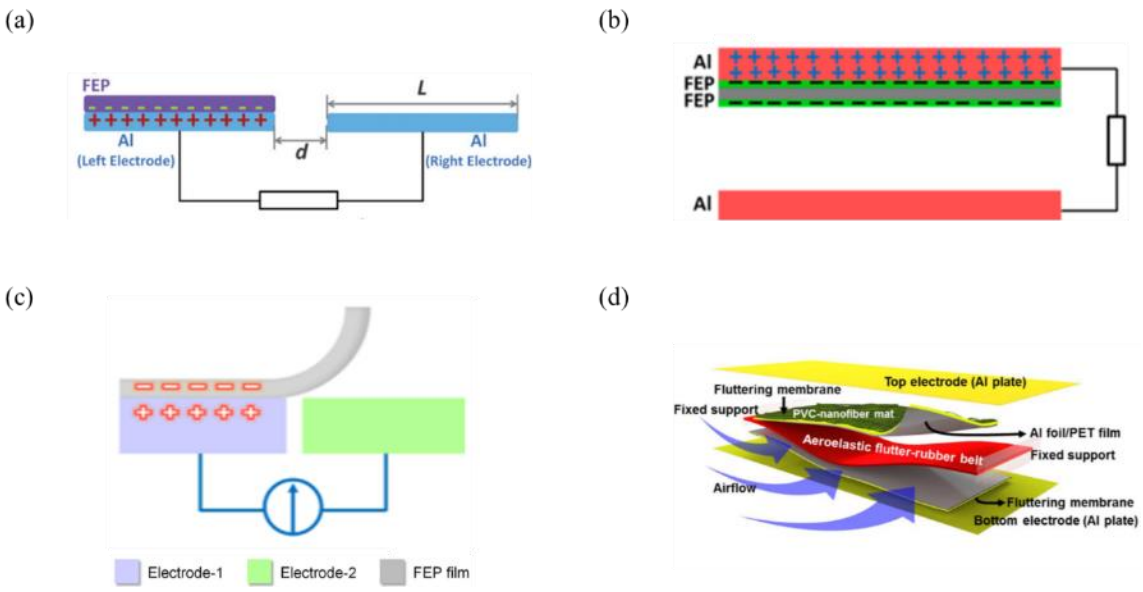

Figure 2.13 Basic FSTENG structures. (a) side-by-side electrodes with laterally moving freestanding layer (b) parallel electrodes with vertically moving freestanding layer (c) side-by-side electrodes with randomly moving freestanding layer (d) parallel electrodes with randomly moving freestanding layer [108-111]

To scale up the harvested energy in one motion cycle, researchers have designed FSTENG gratings. For example, in Figure 2.14(a), a linear FSTENG consists of four electrodes that are separated but connected with electrical circuits. The free-standing layer also has multiple segments. Finer grating units will lead to better output performance. [74] In Figure 2.14(b), two FSTENG devices share one free-standing layer, leading to two outputs with one motion.[112] Circular FSTENGs have also been reported for improving the output power by incorporating multiple energy conversion cycles in a single cycle of mechanical motion. For example, in Figure 2.14(c), the electrode grating is fixed under a rotational free-standing FEP fan, and it can be mounted on a tire.[113] In Figure 2.14(d), the electrode grating is surrounding the freestanding FEP grating. This structure is similar to a motor.[114]

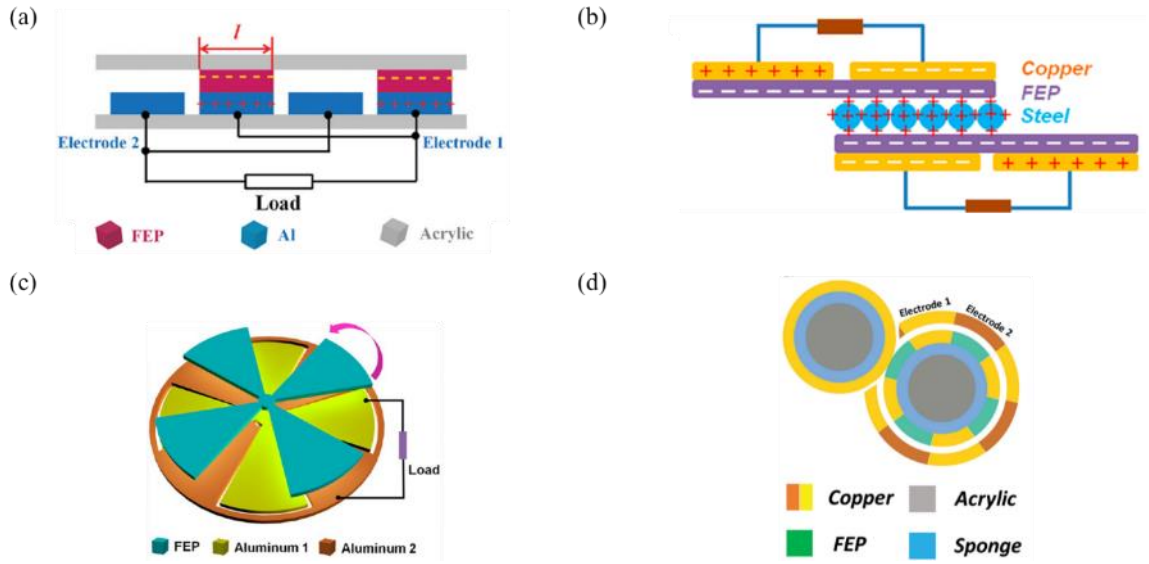

Figure 2.14 Advanced FSTENG structures. (a) linear electrodes grating (b) a pair of side-by-side FSTENGs (c) rotational disk electrode grating (d) the cross-section of a rotational cylindrical electrode grating [74, 112-114]

2.2.5 Discussion

In this section, the basic and advanced structures of TENGs working in four modes are briefly reviewed. The output performance of the devices has been reported in terms of power density (*PD*, power per area), short-circuit current (I_{SC}), open-circuit voltage (V_{OC}), and transferred charges (Q_{SC}). There are several strategies for improving performance. Firstly, deciding the best TENG mode according to the working environment is essential to the design of the device structure. Though the structure FOM shows a comparison of performance among different working modes, the highest one may not be applicable in practice. Secondly, searching for the best materials according to the material FOM or the triboelectric series will directly increase the output. However, limited by their own properties, some materials are not compatible with particular fabrication techniques. The coordination of the material and the fabrication method will have a significant impact on the performance. Thirdly, increasing the contact area will lead to more transferred charges, thus improving the performance. Currently, nanomaterials and nanostructures are widely used to achieve this purpose. However, the degradation and high cost of the nanomaterials need to be taken into consideration.

Up to date, the *PD* and V_{OC} have reached orders of 1 W m^{-2} and 10 kV, respectively.[115, 116] However, in the reports, the tests are generally under different conditions, meaning that the contact force, separation distance, and the moving frequency of the object are not the same. The comparison will be more reasonable if the output can be normalized. Besides, the volume and weight also need to be evaluated when discussing the power density, especially for wearable devices.

Chapter 3 Thermally Drawn Fiber-based TENG for Industrial Loom Weaving

The fiber-based triboelectric nanogenerators (FTENGs) are promising wearable energy harvesters in the era of the internet of things. [117-131] To be integrated into textiles and clothing by industrial looms, they need to be fabricated on a large scale with fast speed. In this chapter, we introduce the thermal drawing process to fabricate scalable, washable, and lightweight triboelectric-energy-generating fibers, which have been woven into textiles both by hand and by an industrial dobby loom. The fabrication process, the output performance, and the applications are presented.

3.1 Fiber-based TENG

It is well-known that food, clothing, and shelter are the barest essentials of human life.[132] Among them, the clothing, whose fundamental element is fibers, has been widely used by humans for thousands of years to cover the soft and curved human body. The fiber-based clothing system possesses many unique features for wearable use. Firstly, the clothing is mechanically robust. The softness and flexibility of the fibers ensure them to maintain structural integrity under external mechanical deformations, including stretching, twisting, bending, and shearing forces. Also, the large number of fibers in the assemblies prevents catastrophic failure of the structure that can be commonly found in solid films. Secondly, the clothing could create a comfortable environment for human activities. The high porosity and large surface area of the clothing allow warmth retention in cold weather and offer channels for air and water vapor to leave the human body in hot weather. Besides, clothing can reduce or even block physical damages such as sunburn, cutting, and pricking. Thirdly, clothing is a popular platform for artistic displays because of its various styles, patterns, and colors.[20, 39] All of these characteristics contribute to the excellent wearability of

the fibers. Nowadays, because of the advancement of fabrication techniques of electronic devices, the requirement of clothing by people is far beyond the mechanics, protection, and aesthetics mentioned above. More functionalities can be seamlessly added to clothing while introducing no extra burden for the users. With the rapid development of electronics, information technology, and data science, fibers have integrated electronic devices, transferring from the conventional passive textiles to an interactive, or 'smart' interface for humans and machines. [133]

As introduced in chapter 1, the triboelectric nanogenerators have various merits as energy harvesters, such as easy availability of energy sources. Integrated into fibers or textiles for wearable use, TENGs can be more potent. A person wearing the fiber-based triboelectric nanogenerators can be regarded as both an inexhaustible and cost-free power source and multiple signal generators. FTENGs can not only convert the energy from the body motions but also act as self-powered active sensors to collect information from different body parts.[39] What's more, because the fibers can be distributed all over the body, they can make the full use of all of the person's body motions. This self-supplied electronic system can operate consistently without external electricity input. We can expect FTENG to bring humans a more consistent, functional, and intelligent era.

3.1.1 Smart Textiles

Smart textiles are functional devices with textile appearances. The components of the textiles can be categorized as 0D, 1D, 2D, and 3D structures based on the complexity. The 0D materials are those with small lengths but yet much smaller diameters, e.g., staple fiber and filament. They can be assembled to 1D fibers by means of twisting, twining, or blending. The 1D fibers can also be fabricated directly with other techniques, such as extrusion and coating. They can be directly used in applications or further integrated into 2D or 3D textiles. The 2D textiles are the most common

type for wearable use. They can be fabricated from 1D fibers by various methods, including weaving, knitting, stitching, braiding, and felting. Almost all of the 2D textiles can be stacked to 3D structures with extra bracing fibers. The classification of textiles in terms of structure dimensions and manufacturing methods can be seen in Figure 3.1.[39] Clearly, the 1D fiber is the basic unit of most of the presented structures. Therefore, the smart textile should be focusing on integrating the functionalities into the 1D fibers.

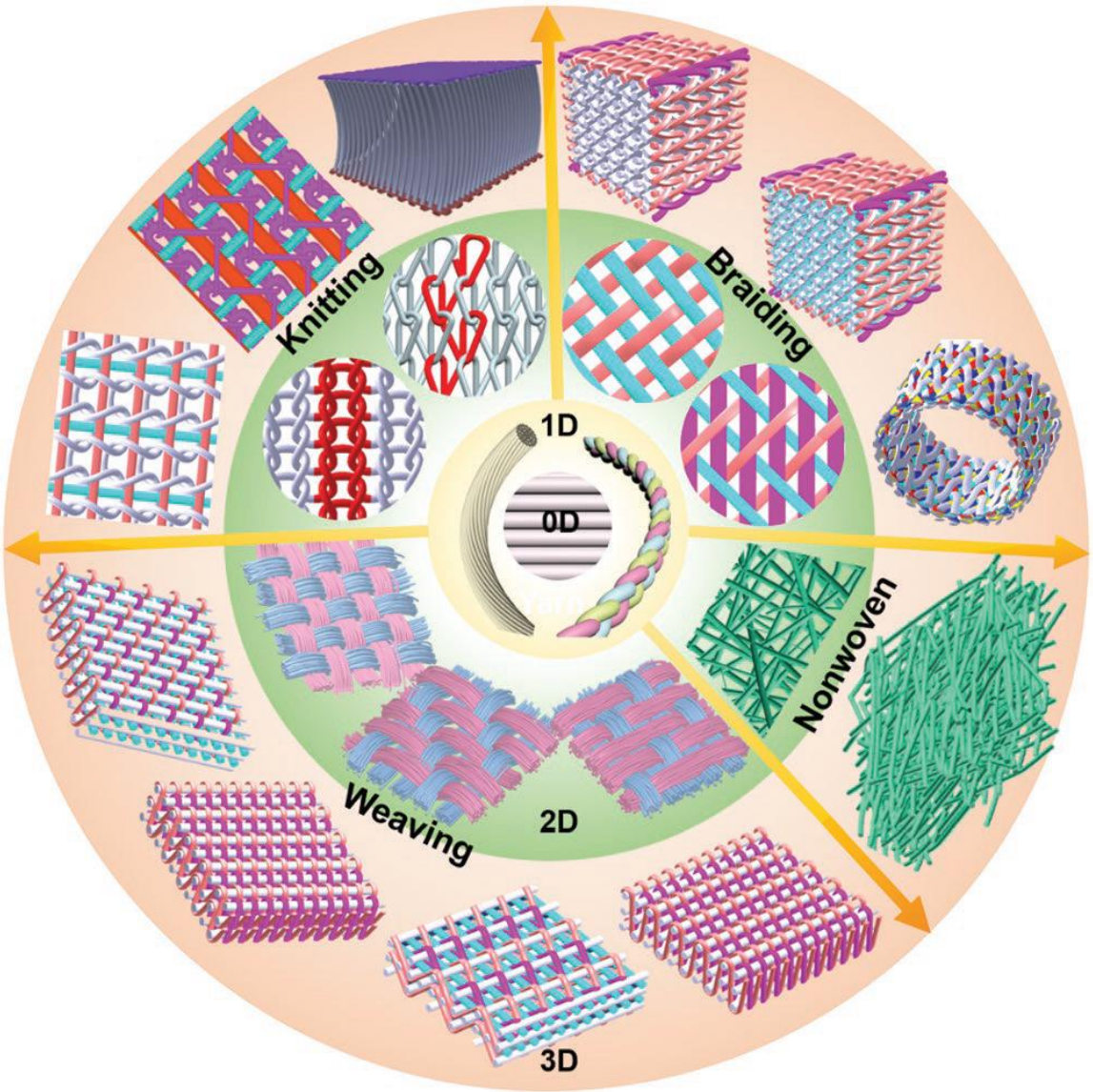

Figure 3.1 Classification of textiles in terms of structure dimensions and manufacturing methods [39]

Because smart textiles rely on electricity and electrical signals, conductive materials are essential components in them. The most straightforward material is metals and their derivatives because they are readily available and possess high conductivities. However, we can rarely see people wearing metal clothing due to their weight and low flexibility. Researchers have been looking for other conductors to make the smart textiles more user-friendly. The ideal conductor for smart textiles is supposed to have high conductivity, flexibility, mechanical robustness, and environmental stability and low cost, weight, and toxicity. Recently, a lot of candidates have sprung out, namely conducting polymers,[134-138] carbonaceous fillers,[139-141] liquid electrodes,[142, 143] and hybrid fillers.[144-148] Their characteristics are summarized in Table 3.1.[39] While it is not possible to have all the ideal features, each of them can find their best applications based on their merits.

Table 3.1 Summary and comparison of frequently used conductive materials for smart textiles [39]

Classification	Categories	Advantages	Disadvantages
Metals and its derivatives	Metal, alloy, semi-conductor, metallic nanoflakes/nano-particles/nanowires	High conductivity, high mechanical robustness, good stability, ease of process	Unconformable, low flexibility, easy to rust, easy to oxidize
Conducting polymers	PPy, PEDOT/PEDOT:PSS, PANi, PAc, PTh, PPV, Pfu, PPP	High flexible, solution processable, easily controlled	Relatively high cost, different to prepare, low electrical con-ductivity, poor stability
Carbonaceous fillers	Carbon black/particle/fiber, CNT, CMF/CNF, carbon aerogel, G/GO/rGO	High aspect ratio, nanoporous architecture, superior mechanical property, environmental stability	Difficult in structure control, poor solution dispersion
Liquid electrodes	Liquid metals (e.g., EGaIn), liquid electrolytes (e.g., NaCl)	Soft, high electrical conductivity, good thermal conductivity, excellent flowability	Heavy, oxidize and leakage, toxicity, expensive
Hybrid fillers	Combination of different conductive materials (e.g., Ag NWs/CNTs)	Synergistic effect	Increased preparation cost and workload

3.1.2 Structures and Fabrication Methods of FTENG

FTENGs are the basic units for textile-based TENGs. Based on the working mode, they can be classified into single-electrode FTENGs and vertical contact-separation FTENGs. The SE mode ones usually consist of a coaxial structure of conductive and dielectric materials, and the CS mode ones usually have a core-sheath structure, where there are gaps between the core and the sheath. Compared with the CS mode FTENGs, the SE mode ones are usually easier to fabricate because there is no need to create the extra space between the layers.[39, 149]

The simplest SE mode FTENG has a conductive electrode covered by dielectric materials. The typical fabrication methods are shown in Figure 3.2. By coating (Figure 3.2(a)), dielectric gels, such as PDMS and silicone rubber, can be wrapped around the solid electrodes, such as stainless steel and copper.[150, 151] By twisting (Figure 3.2(b)), the commercial yarns can be twined around the solid electrode.[152] By pumping (Figure 3.2(c)), the liquid metal can fill the hollow channel of polymer tubings.[153] Based on the mechanical properties, the fibers can be then integrated into textiles by sewing, weaving, knitting, or braiding.[150-152, 154]

Though the fabrication is straightforward, there are several problems to be addressed. First, the diameters of the solid electrodes are usually large to be coated evenly and to survive the big strain during twisting, resulting in significant weight and low flexibility. The coating makes the diameter even larger, making the fiber not compatible with industrial looms. Second, liquid metal can suffer from leakage when the textile is physically damaged, thus being neither electrically nor environmentally stable. Third, the length of the coated fiber is limited by the length of the mold (~1 m), while the textile industry requires long fibers (>100 m). Fourth, because the coating process is usually time-consuming (~10 h), fast and scalable production is difficult. Last, the stretchability of the above fibers is very small.

A lot of efforts have been devoted to improving the stretchability of the single-electrode mode FTENG. Helix electrodes are widely used. Two typical fabrication methods are shown in Figure 3.2. In Figure 3.2(d), a solid electrode is twined on a stretchable polymer to form a helix. Then, the supported helix is coated with another layer of polymer.[155] In Figure 3.2(e), an already established electrode helix is inserted in a stretchable polymer tubing.[156] Also, the liquid metal-based FTENG will be stretchable if the tubing material is changed to stretchable ones, such as silicone.[142] Another strategy to improve stretchability is to integrate the fiber into internally stretchable structures, such as serpentine and knitted ones. [150, 151]

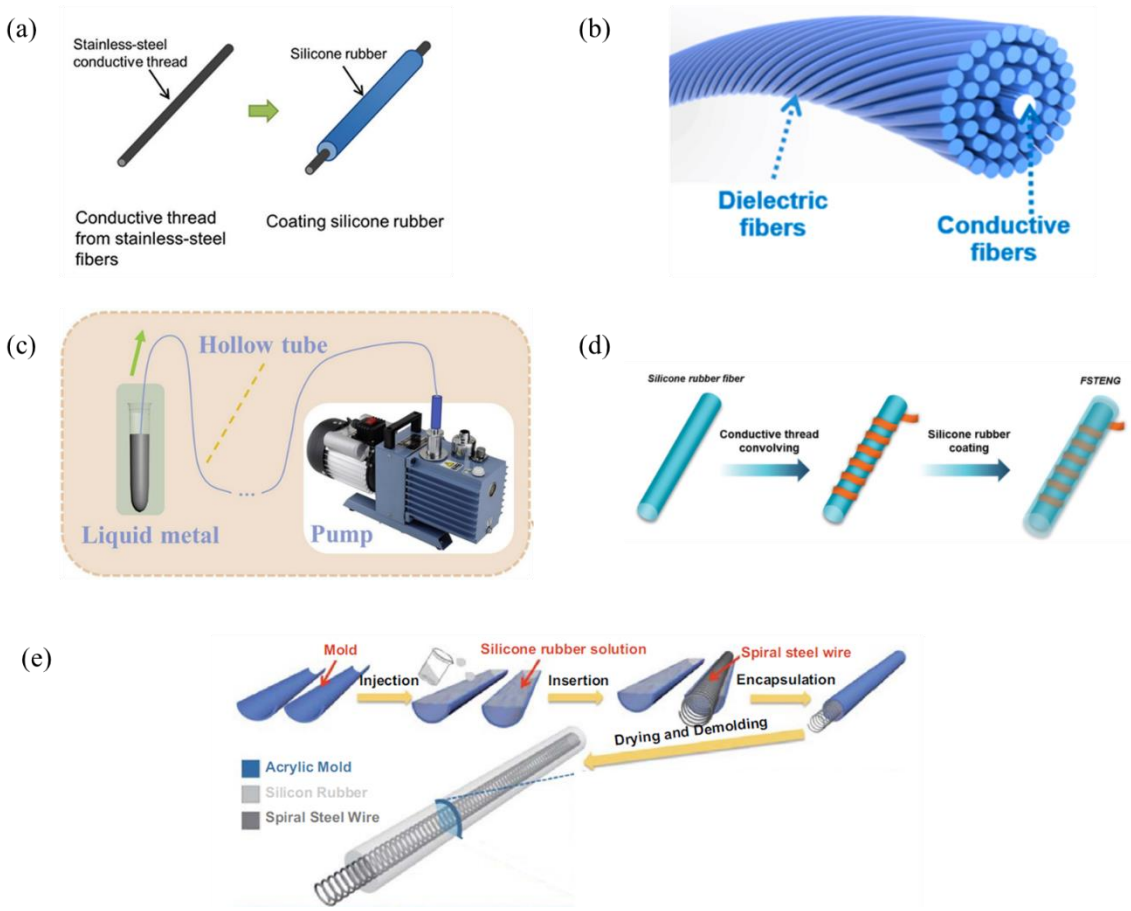

Figure 3.2 Typical fabrication methods for single-electrode mode FTENG. (a) coating (b) twisting (c) pumping (d) helix electrode on stretchable polymer rod (e) helix electrode inserted in stretchable polymer tubing [150-154]

3.1.3 Discussion

For wearable use, the FTENGs should be compatible with the industrial looms, which have several requirements. First, the diameter of the fiber should be on the sub-millimeter scale. Second, the fiber length should be on the sub-kilometer scale or even longer for continuous weaving. Third, the fiber should be flexible yet strong enough to survive the twisting, pulling, and beating forces. Unfortunately, the current fabrication methods can hardly meet all of them. Moreover, the fabrication speeds of the state-of-arts methods are also hindering the scaling-up process of FTENGs. Therefore, we introduce the thermal drawing process, which is a well-established technique for multifunctional fiber fabrication.

3.2 The Thermal Drawing Process

The thermal drawing process (TDP) has been applied to the mass production of advanced multifunctional fibers for a few decades.[157] Kilometers of fibers that integrate different materials with disparate optical, electronic, and optoelectronic properties can be drawn from a macroscopic scaled-up model of the fiber called a preform, where functional materials are well-positioned based on the designed sophisticated structure. The fibers that maintain the preform cross-section structure at scale and complex functionalities can be produced in a straightforward and unprecedentedly scalable way. [158] Multiple independent devices can be arranged in the preform, and the subsequent thermally drawn fiber consists of a high density of devices with various functionalities. The dimension of the cross-section of the fiber can be controlled during the drawing process, and the feature size can span several orders of magnitude: from micrometers to a few nanometers[159]. In Figure 3.3, we can see the diameter of the feature size in thermally drawn fibers can be scaled down from ~100 μm to ~10 nm scale, and the length of the fiber can be up to ~10,000 km scale.[159, 160] The miniature cross-section and extreme length enable the

fibers to be compatible with the industrial looms. Therefore, the multifunctional fibers can find a wide range of wearable applications, including optics, communications, sensing, energy harvesting and storage, and artificial muscles.[56, 161-165]

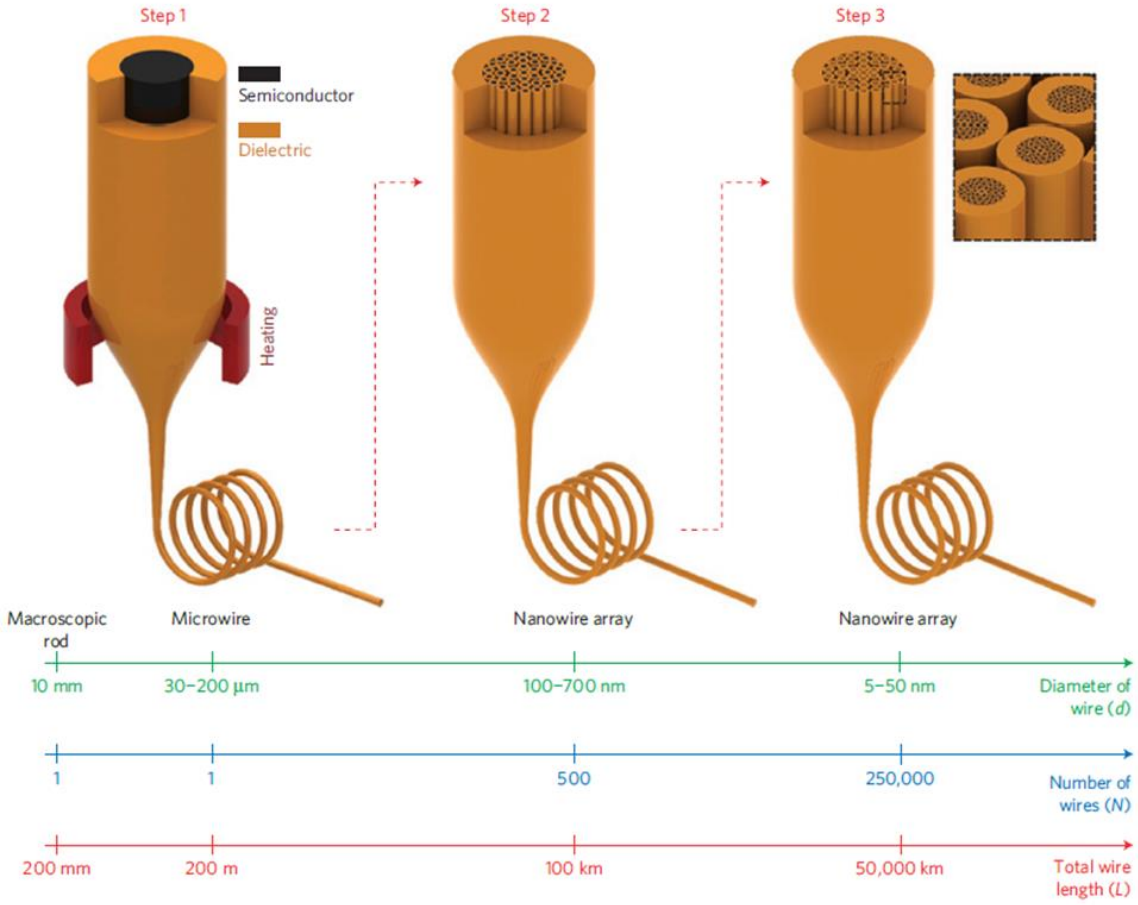

Figure 3.3 A macroscopic multimaterial preform is reduced to ordered arrays of nanowires by thermal size reduction in a protective polymer matrix in successive steps [159]

The general thermal drawing process is shown in Figure 3.4 with the draw tower at Virginia Tech. A bulk preform is mounted on the holder and then inserted into the three-zone furnace. It is heated to a temperature that is above its glass transition point. When it is soft enough, the capstan at the bottom starts to rotate, thus pulling the preform downward. The viscosity of the softened preform, the feeding speed, and the tension applied by the capstan jointly decide the diameter ratio of the

fiber to the preform, which is called the draw-down ratio (DDR). The diameter of the fiber can be measured in real-time with the laser micrometer.

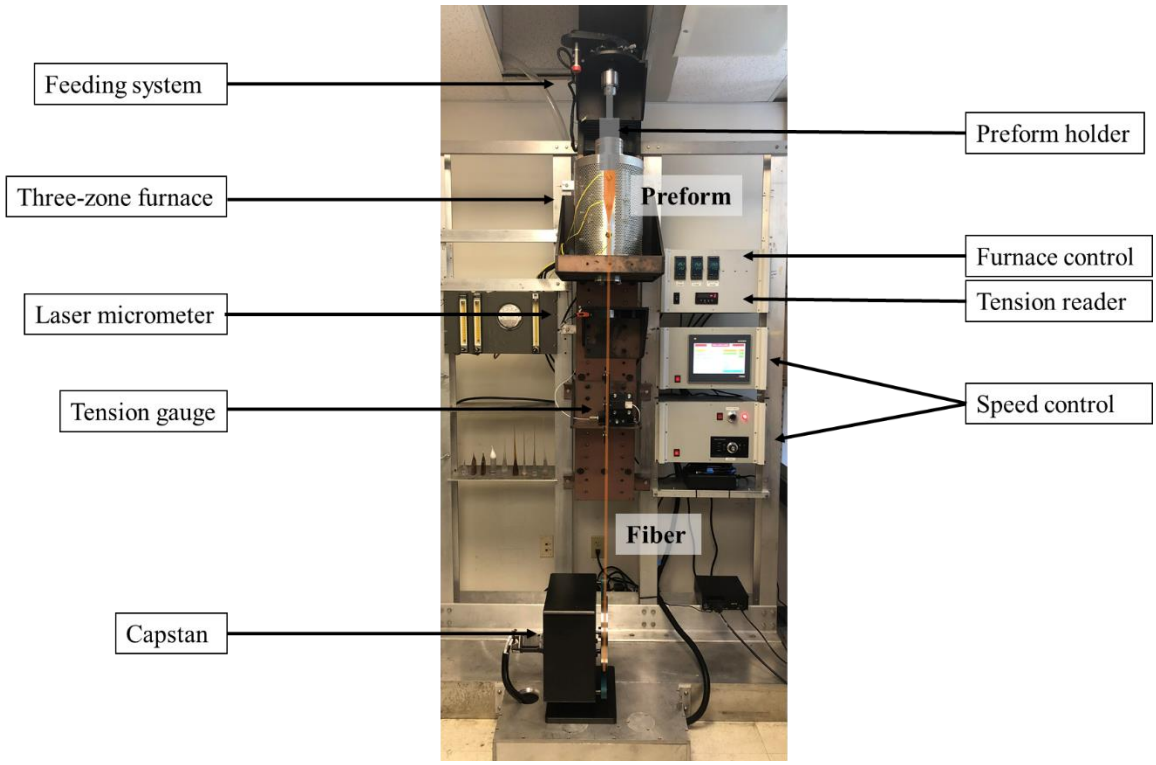

Figure 3.4 Illustration of the general thermal drawing process with the draw tower at Virginia Tech and a virtual preform and fiber

3.3 Fabrication of Thermally Drawn FTENG

3.3.1 Structure Design and Material Selection

The designed structure is shown in Figure 3.5. It is the simplest single-electrode mode FTENG, which has a conductive core and a dielectric cladding. The cladding also serves as the triboelectric surface. Because the FTENG is aimed to be compatible with industrial looms, the diameter of it is designed to be on ~350 μm scale.

While we planned to use metal wires as the electrodes, the diameter of them should be small so that the fiber will be light and flexible. The wires yet need to be strong enough to survive the pulling and beating forces during the thermal drawing and the looming processes and our daily life use. Therefore, tungsten wires with a diameter of 50 μm were employed in the fiber. We also used copper (Cu) wires with a diameter of 80 μm in the thermal drawing process to demonstrate that the electrode material is changeable.

There are a few requirements for the dielectric cladding material. Firstly, it should be one of the thermoplastic materials, which are thermally drawable because they have a temperature window for softening when being heated. The thermoplastic materials can be categorized as amorphous ones and semicrystalline ones. The semicrystalline ones (e.g., polypropylene) have relatively smaller windows than the amorphous ones (e.g., PMMA) have. If a semicrystalline is used as the functional material, it is best to house it with an amorphous layer for protection. The protection layer can be peeled off or etched off afterward, thus referred to as the sacrificial layer. If an amorphous material is used as the functional material, no sacrificial layer is needed. Secondly, considering the output performance of the FTENG, we are supposed to use a rather polarized material in the triboelectric series. Thirdly, to make the fiber flexible, we need to use soft materials, meaning that Young's modulus of the material should be small. Besides, for wearing use, washability should also be taken into consideration. Hydrophobic materials will be preferred. Based on the requirement above, we selected one semicrystalline material and one amorphous material for the thermally drawn FTENG. They are polypropylene (PP) and polycarbonate (PC), respectively.

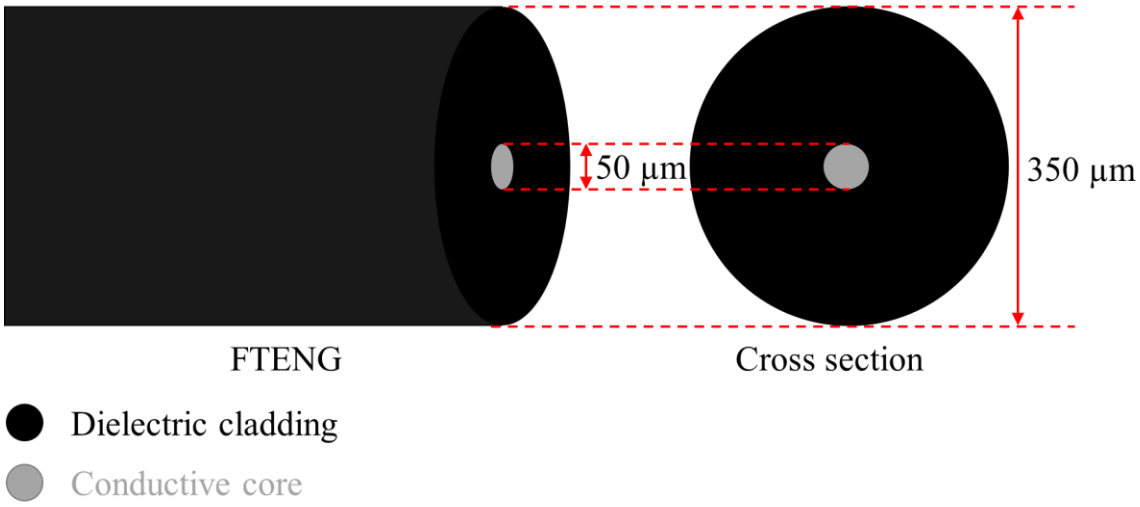

Figure 3.5 The structure of the designed thermally drawn FTENG

3.3.2 The Thermal Drawing of FTENG

3.3.2.1 FTENG with PP cladding

The fabrication process of the preform is shown in Figure 3.6(a). PMMA films (SolaTuf) were wrapped around a PP tubing (McMaster-Carr, 1859T16). They were baked in a vacuum oven for consolidation at 140 °C for 30 min. During the consolidation, the air in between of the PMMA films was vacuumed out, and the PMMA films were consolidated into one sacrificial layer. The diameter of the hollow channel, the outer PP tubing, and the outer PMMA were 5 mm, 20 mm, and 26 mm, respectively. The length of the preform was 15 cm.

The preform was then inserted in the three-zone furnace in the draw tower (Figure 3.6(b)). The temperatures of the three zones of the furnace were 145 °C (top), 245 °C (middle), and 100 °C (bottom), respectively. During the drawing, the tungsten wire (McMaster-Carr, 3775K11) was fed into the hollow channel of the preform. Because the drawing temperature was much higher than

the melting point of PP (~160 °C), PP would attach to the tungsten wire during the TDP when the DDR is high enough. The DDR was controlled by tuning the speeds of the capstan and the feeding system to stabilize the fiber diameter at 455 µm. The fabrication speed could reach 4 m min^{-1}. The fiber diameter was measured by a laser micrometer (LaserLinc, TLAser 222) in real-time. After the drawing, the sacrificial layer was mechanically peeled off (Figure 3.6(c)), exposing the PP/tungsten fiber (Figure 3.6(d)). The cross-section of as-fabricated fiber is shown in Figure 3.6 (e). A single PP/tungsten fiber of 100 m is shown in Figure 3.6 (f). In Figure 3.6 (g), we can see that the fiber have excellent flexibility.

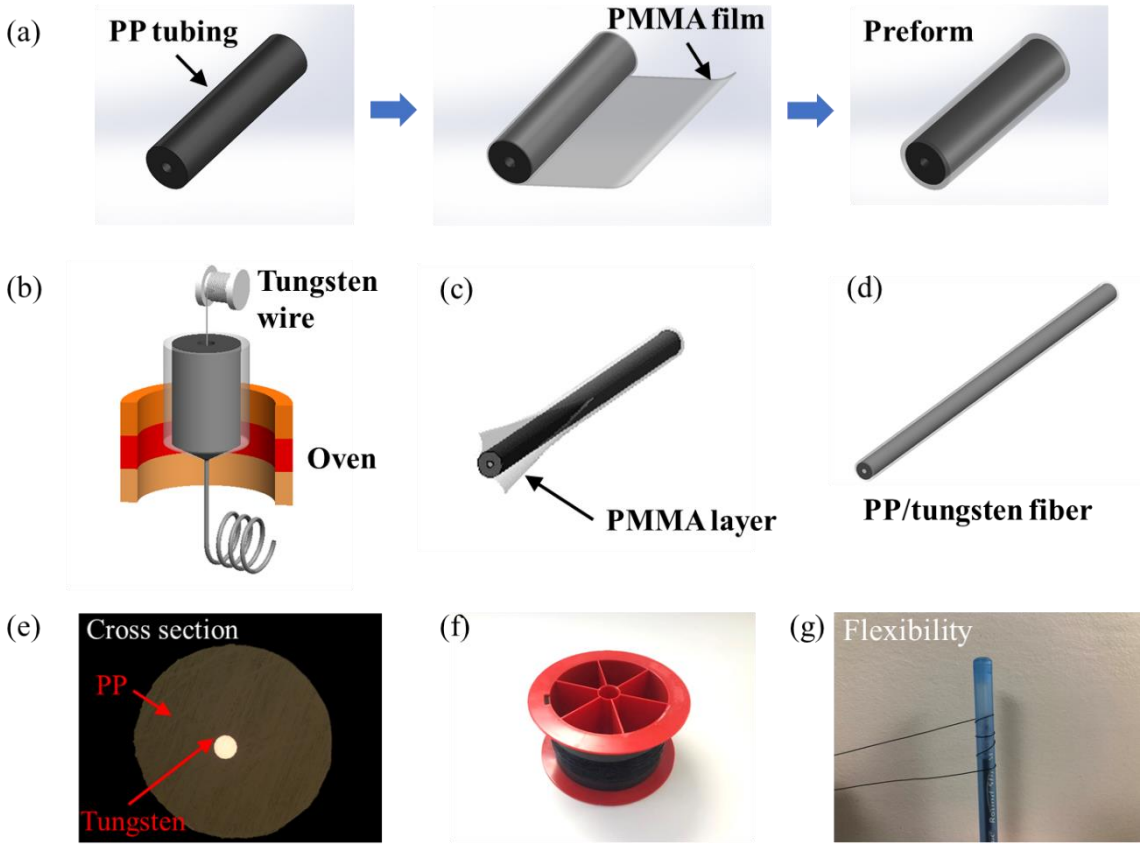

Figure 3.6 Thermally drawn PP/tungsten FTENG (a) Illustration of the fiber preform fabrication. (b) Illustration of the fiber thermal drawing process. (c) and (d) The post-drawing process to remove the sacrificial PMMA layer and the final PP/tungsten fiber. (e) The cross-section of the as-fabricated FTENG. (f) A single PP/tungsten fiber of 100 m. (g) Flexible FTENG wrapped on a pen.

Because TDP is a platform for FTENG fabrication, the materials can be customized. We also demonstrated thermally drawn (PP/Cu) fiber (Figure 3.7).

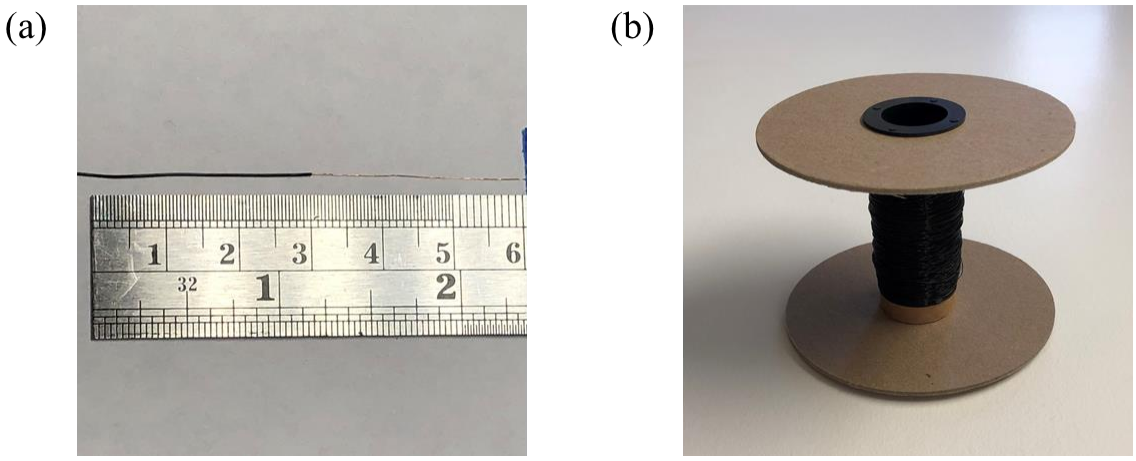

Figure 3.7 Thermally drawn PP-cladding FTENGs with 80 um-diameter Cu wires. (a) PP/Cu fiber with the right half cladding removed. (b) A single PP/Cu fiber of 50 m.

3.3.2.2 FTENG with PC cladding

The fabrication process of the preform is shown in Figure 3.8(a). PC films (Polymershapes, LEXAN FR83) were wrapped around a Teflon rod. The films were consolidated in a vacuum oven at 190 °C for 30 min. The Teflon rod was extracted after consolidation. The inner and outer diameter of the PC tubing were 3.175 mm (1/8") and 22.225 mm (7/8"), respectively. The length of the preform was 15 cm.

The thermal drawing process of the PC-cladding fiber (Figure 3.8(b)) was similar to that of the PP-cladding one. The temperatures of the furnaces were 150 °C (top), 285 °C (middle), and 120 °C (bottom), respectively. No post-drawing step is needed as there is no sacrificial layer in the fiber (Figure 3.8(c)). The cross-section of as-fabricated fiber is shown in Figure 3.8 (d). A single PC/tungsten fiber of 200 m is shown in Figure 3.8(e).

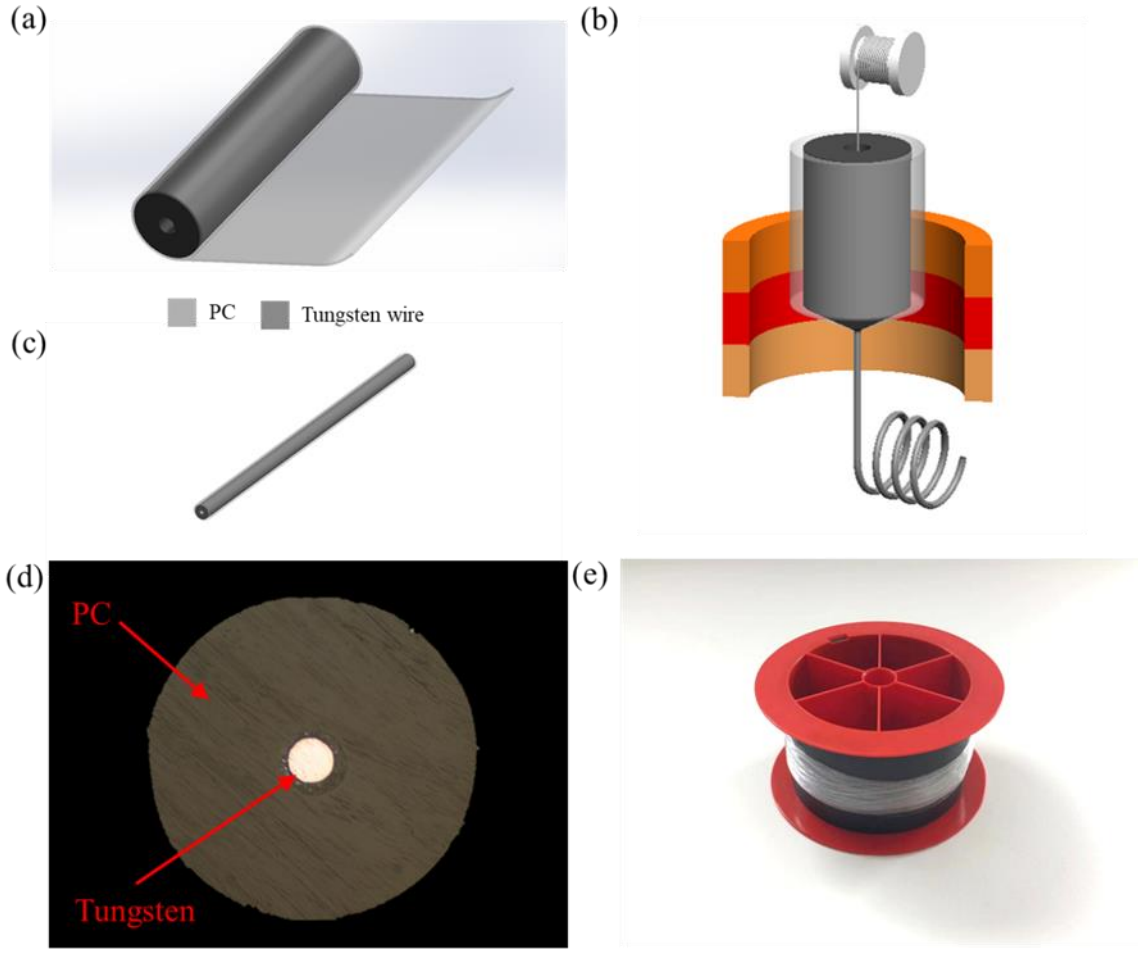

Figure 3.8 Thermally drawn PC/tungsten FTENG (a) Illustration of the fiber preform fabrication. (b) Illustration of the fiber thermal drawing process. (c) The final PC/tungsten fiber. (d) The cross-section of the as-fabricated FTENG. (e) A single PC/tungsten fiber of 200 m.

Again, fibers with Cu electrodes were demonstrated (Figure 3.9). Because PC is transparent, We can see the color of the electrode. Therefore, the aesthetic requirement can be met by choosing electrodes with the proper color.

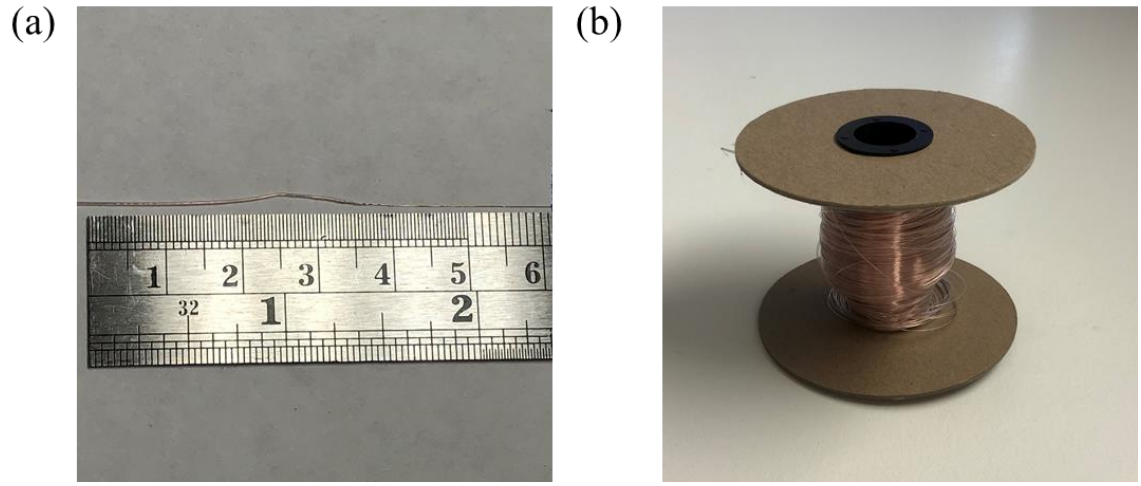

Figure 3.9 Thermally drawn PC-cladding FTENGs with 80 um-diameter Cu wires. The orange color is from the copper. (a) PC/Cu fiber with the right half cladding removed. (b) A single PC/Cu fiber of 300 m.

3.3.3 Textiles Woven with FTENGs

We have woven with the PP/tungsten and PC/tungsten fibers into textiles, respectively. The structure for hand weaving and industrial loom weaving and the as-woven textiles are illustrated in Figure 3.10 and 3.11, respectively. The industrial dobby loom used for weaving is shown in Figure 3.11 (b). In the loom-woven textile, the FTENG was woven with the standard cotton yarns. As can be seen in Figure 3.11 (d-f), continuous FTENG twill, FTENG-cotton twill, and plain weaving patterns are demonstrated.

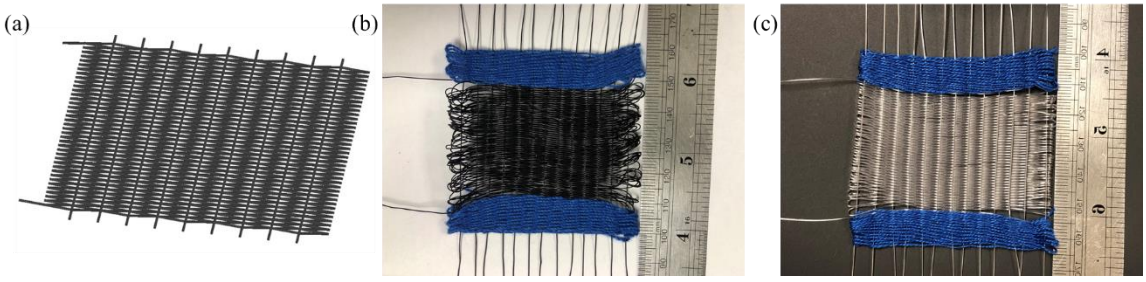

Figure 3.10 Hand-woven FTENG textile (a) Illustration of the textile structure. (b) Hand-woven PP/tungsten FTENG textile. (c) Hand-woven PC/tungsten FTENG textile.

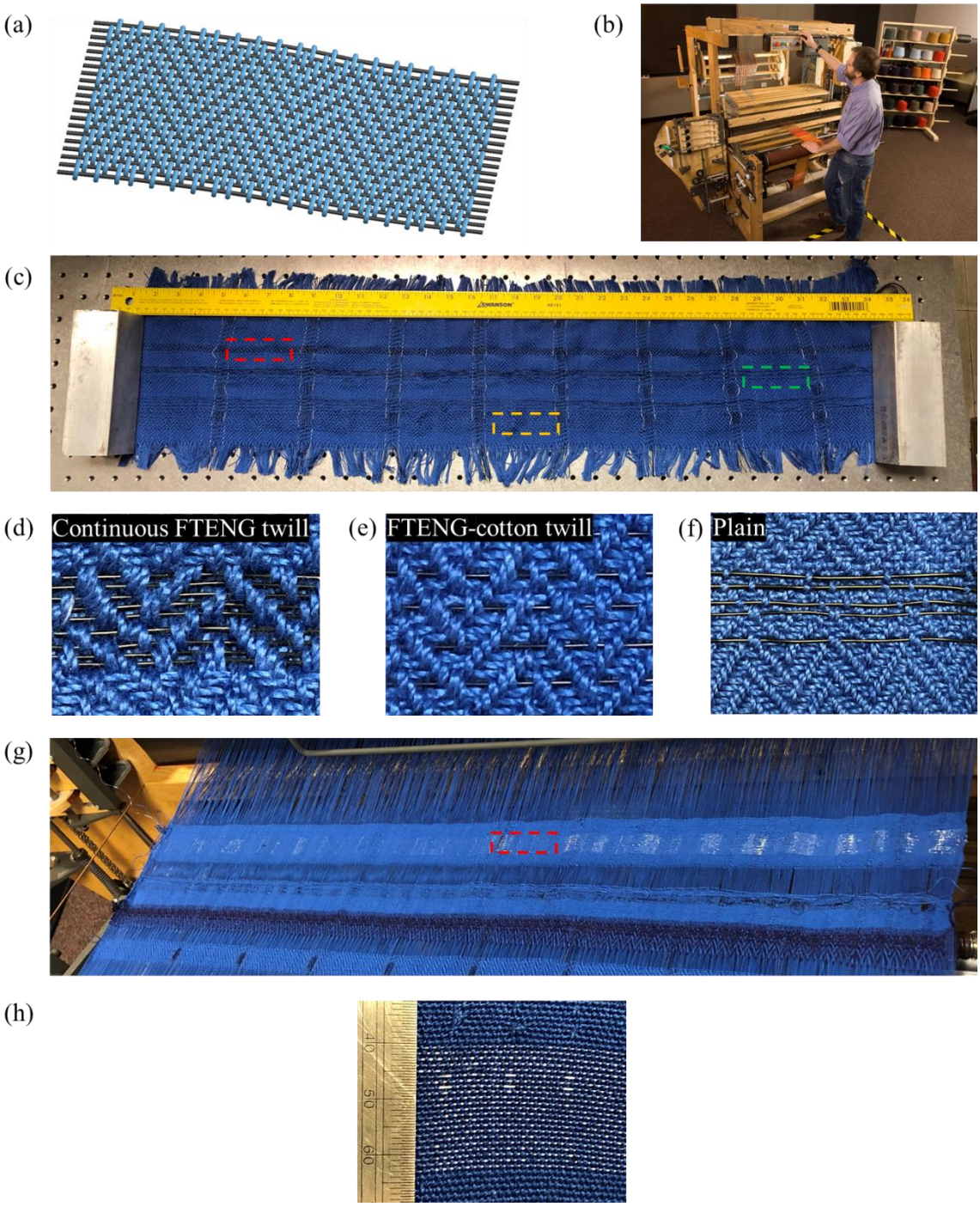

Figure 3.11 Industrial loom-woven FTENG textile (a) Illustration of the textile pattern. (b) The industrial dobby loom used for weaving. (c) Industrial loom-woven PP/tungsten FTENG textile. (d-f) Three areas in (c). (d) Red box: continuous-FTENG twill weaving; (e) Yellow box: FTENG-cotton twill weaving; (f) Green box: plain weaving. (g) Industrial loom-woven PC/tungsten FTENG textile. (h) The boxed area in (g).

As shown in Figure 3.12, the textile that was shown in Figure 3.11(c) could be mechanically folded both horizontally and vertically and stretched diagonally. Therefore, the FTENG proves good flexibility after woven into textile by the industrial loom.

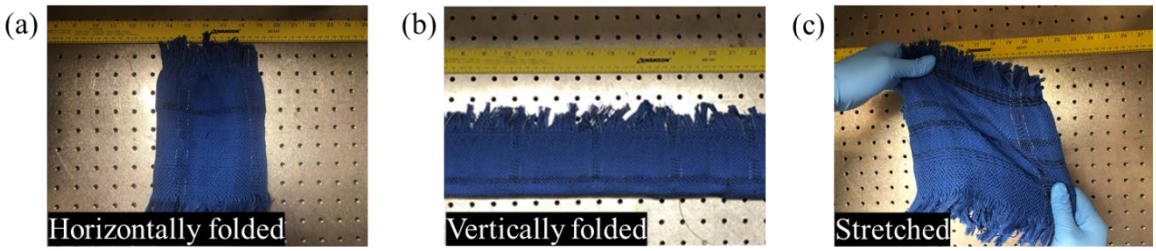

Figure 3.12 Industrial loom-woven FTENG textile being (a) folded horizontally, (b) folded vertically, and (c) stretched diagonally.

To evaluate the breathability of the FTENG swatches, we conducted air permeability tests following ASTM D737 with a commercial air permeability tester (SDL Atlas M021A, Fig. 3.13). Under the pressure of 125 Pa, the air permeabilities of the textiles shown in Figure 3.10(b) and (c) are 523.0 and 394.8 $cm^3\ cm^{-2}\ s^{-1}$, respectively. These numbers prove excellent breathability, which can be attributed to the space between the fibers and the slick surfaces of the fiber cladding.[39]

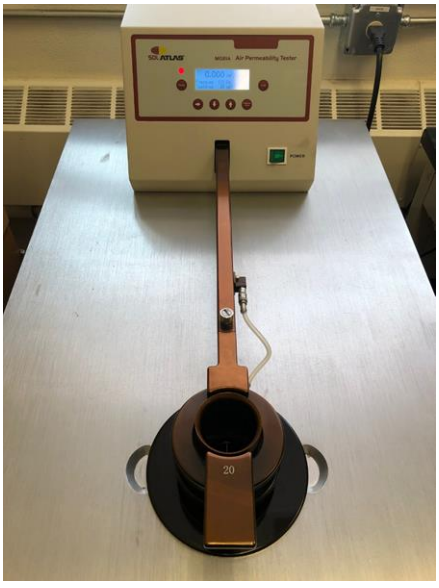

Figure 3.13 The air permeability tester used for breathability tests

In summary, both hand-woven and loom-woven textiles have been demonstrated with the thermally drawn FTENGs. The fibers can be woven with the regular cotton yarns by the industrial dobby loom. This compatibility is attributed to the length, flexibility, and strength of the fiber. Besides, the woven textiles also show good flexibility and breathability, which are essential to wearable use.

3.4 Electrical Performance of FTENG

3.4.1 Working mechanism

The thermally drawn FTENGs work in the single-electrode mode described in section 2.1.1.3. The schematic of the working mechanism can be seen in Figure 3.14(a). When external materials get into contact with the cladding, the triboelectric effect takes place. For example, if leather contacts a PP-cladding FTENG, negative charges will transfer to and accumulate on the PP surface. When the two surfaces are separated, the electrostatic induction effect will lead to a time-varying electrical potential field. The current will flow from the ground to the PP/tungsten interface with the increase of the gap. When the gap becomes smaller, the current will flow back to the ground. Such alternating currents will flow back and forth with the approaching-separating motions. Because any conductor can serve as the ground, we used a piece of aluminum foil because of its lightweight and flexibility. To better understand the triboelectrification-generated potential distribution, we did a numerical simulation using the finite element method with the COMSOL software. The results are shown in Figure 3.14(b). The charge density on the contacted surfaces was set to be 1 $\mu C\ m^{-2}$, and the maximum gap length was 5 cm. When external material is away from the FTENG, the electrical potential around the external material increased significantly, while the potential around the FTENG stayed at zero.

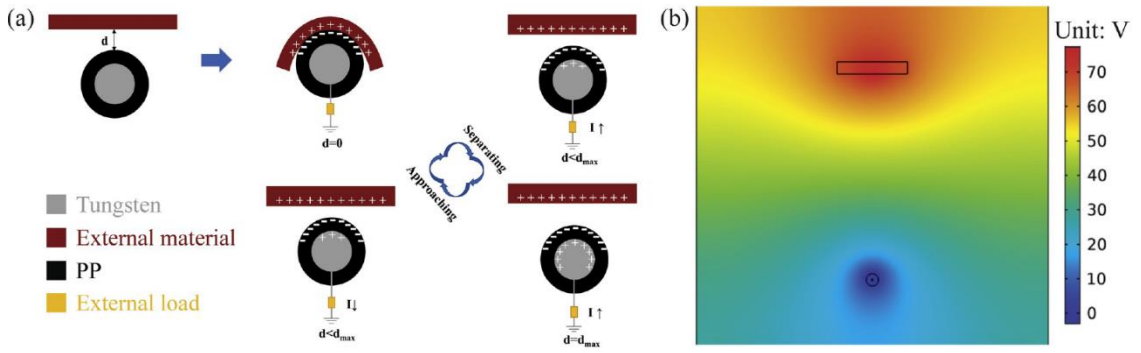

Figure 3.14 The working mechanism of FTENG. a) Schematic of the working mechanism of the FTENG in single-electrode mode. The core/cladding ratio is much larger than the actual fiber for better illustration b) Numerical simulation of the potential distribution when external material and FTENG are contacted and separated by COMSOL software.

3.4.2 Cyclic tests

The electrical output of the textile shown in Figure 3.10(b)(PP/tungsten) was quantitatively tested with a homemade apparatus(Figure 3.15). A 1" x 1" nylon plate was driven by a linear motor to apply forces on the FTENG textile cyclically.

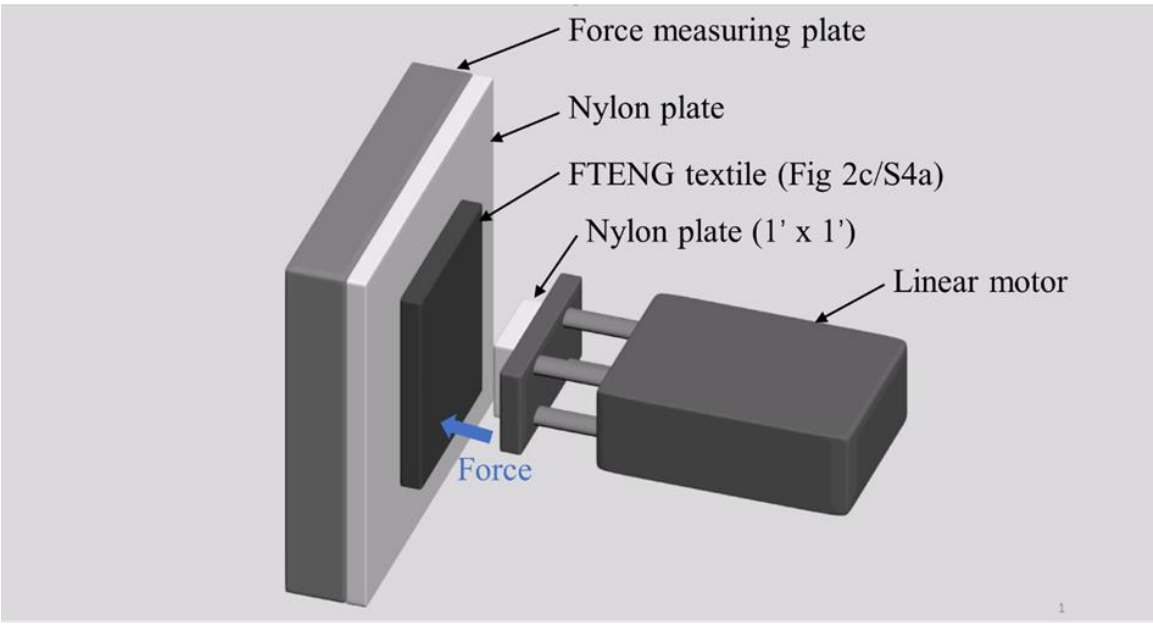

Figure 3.15 Schematic of the cyclic test system

As can be seen in Fig. 3.16, we investigated the effects of the applied force and the cycle frequency on the outputs. When the cycle frequency was fixed at 8 Hz (Figure 3.16(a)), the short-circuit transferred charge (Q_{SC}) went up from 6.2 nC to 10.0 nC when the force was increased from 30 N to 90 N. This change was because a larger force will result in a larger contact area and, subsequently, stronger triboelectrification. As both the open-circuit voltage (V_{OC}) and the maximum short-circuit currents (I_{SC}) are dependent on the charge amount, they also increased when the force increased, going from 12.9 V and 0.42 μA to 21.4 V and 0.78 μA, respectively. When the applied force was fixed at 70 N (Figure 3.16(b)), Q_{SC} and V_{OC} remain constant at around 8.8 nC and 18.9 V, respectively. The peak short-circuit currents (I_{SC}) was increased from 0.11 μA to 0.68 μA when the moving frequency increased from 2 Hz to 8 Hz. This significant change was based on the formula: $I = Q/t$. Since Q_{SC} was nearly a constant in this test series, I_{SC} was inversely proportional to the frequency. When the force and frequency were fixed at 70 N and 8 Hz, the fabric's output current was measured with different external loads, and the power density (*PD*) was accordingly calculated with the following formula.

$$PD = \frac{I^2 R}{m} \tag{3.1}$$

where I is the maximum current, R is the external resistance, and m is the mass of the functioning FTENG. As mentioned in Ref [39], there is currently no universal standard to evaluate the electrical output of FTENGs. While power per area is popularly used for evaluation, the diameter and the mass density, which are essential parameters in wearable devices, cannot be reflected. Thus, we propose using power per weight that takes all the parameters mentioned above into consideration. The *PD* peaked at 43.0 mW kg^{-1} with an external load of 80 MΩ (Figure 3.16(c)). To evaluate the durability of the FTENGs, we did a cyclic test for 100,000 cycles. The results (Figure 3.16d) showed no obvious change in output in terms of I_{SC}. Besides, in the washability

tests (Figure 3.16e), the contaminant was first poured onto the fabrics (Fig. 3.17) and then washed with flowing water and naturally dried. The output was stable after each wash cycle.

The output of the textile loomed with PC cladding FTENG shown in Figure 3.10(c) was also quantified and displayed in Figure 3.16. The trends were the same as that of the PP cladding FTENG textile. When the cycle frequency was fixed at 8 Hz, Q_{SC}, V_{OC}, and I_{SC} went up from 10.77 nC, 21.8 V, and 0.55 μA to 15.2 nC, 30.6 V, and 0.96 μA, respectively; when the applied force was fixed at 70 N, Q_{SC} and V_{OC} stabilized around 14.1 nC and 27.8 V, and I_{SC} went up from 0.14 μA to 0.86 μA. The highest *PD* was 67.4 mW kg^{-1}.

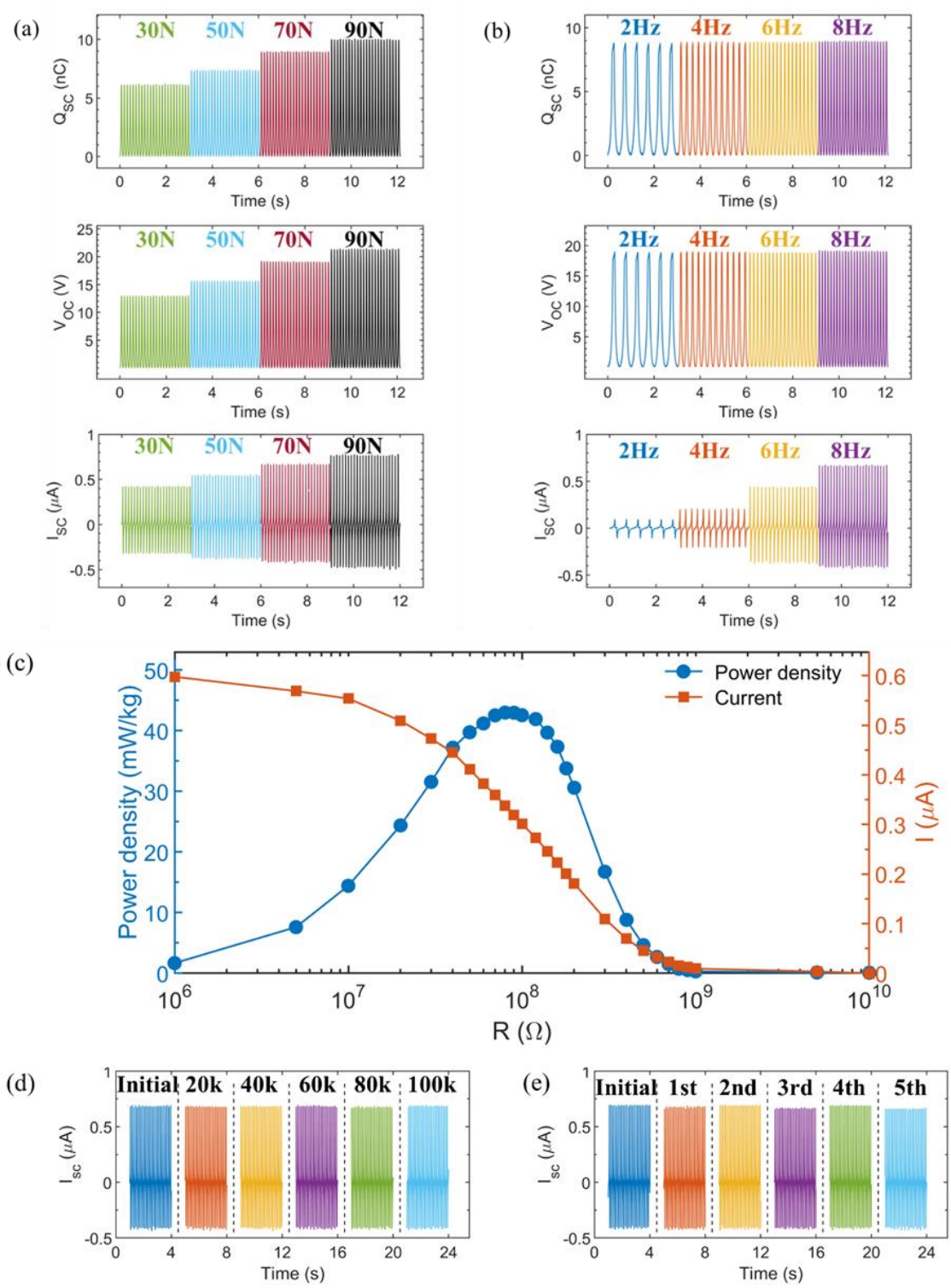

Figure 3.16 The electrical output of PP/tungsten FTENG. Q_{SC}, V_{OC}, and I_{SC} of the textile shown in Figure 3.10(b). The (a) applied force and (b) cycle frequency were fixed during the test. (c) The current and power density (power per kilogram of fiber) of FTENG when connected to different external loads. (d) Durability test. (e) washability test.

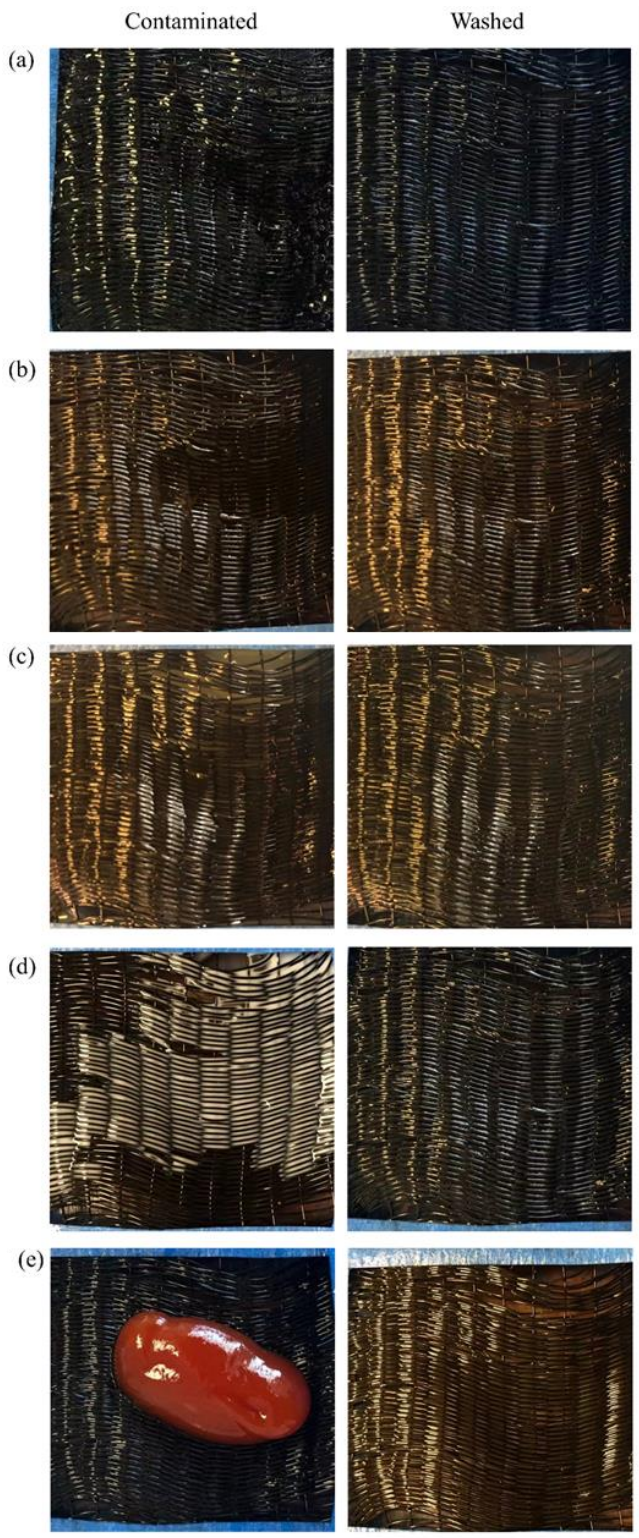

Figure 3.17 Washability tests. FTENG swatch was contaminated and washed by flow water. a) Coke, b) coffee, c) orange juice, d) milk, e) ketchup.

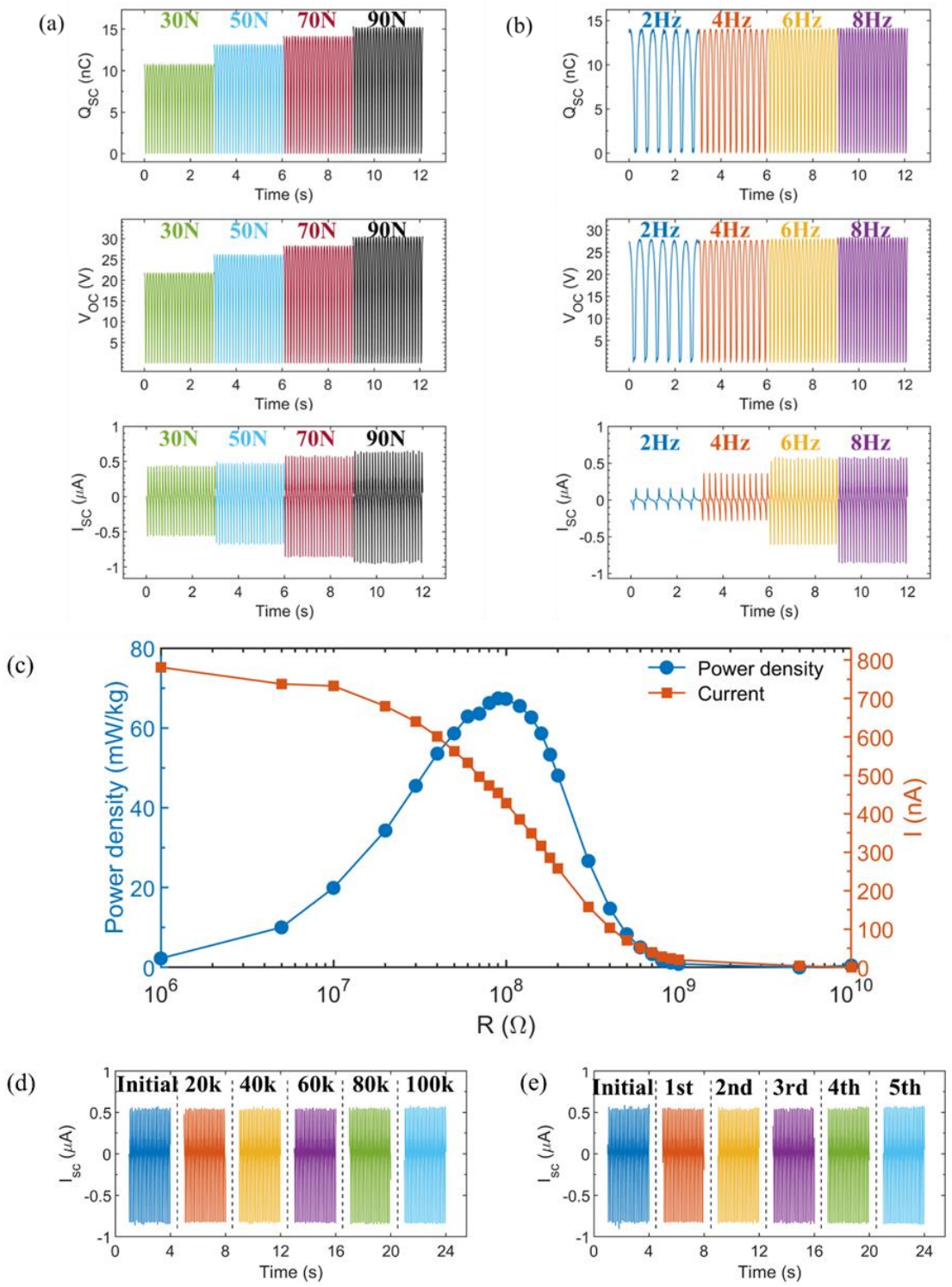

Figure 3.18 The electrical output of PC/tungsten FTENG. Q_{SC}, V_{OC}, and I_{SC} of the textile shown in Figure 3.10(c). The (a) applied force and (b) cycle frequency were fixed during the test. (c) The current and power density (power per kilogram of fiber) of FTENG when connected to different external loads. (d) Durability test. (e) washability test.

3.5 Applications

3.5.1 Power Sources

The energy generated by the FTENG textiles could be consumed instantly or stored for later uses. For instant use, we have demonstrated that a series of 62 commercial green LEDs were immediately lit up (Figure 3.19(a)) by the FTENG textile, where the brightness was dependent on the current. For energy storage, we charged three commercial capacitors with different capacitances with the FTENG textile. The charging curves are shown in Figure 3.19(b). The standard rectifier circuit was used in the charging. For the three capacitors, which are 0.1 μF, 0.22 μF, and 0.47 μF, respectively, the saturation voltage (55 V) was reached with charging times of 0.8 min, 1.8 min, and 3.6 min, respectively. The charging time is determined by the following formula:

$$Q = CU = It \tag{3.2}$$

where Q is the charge stored in the capacitor, C is the capacitance, U is the saturation voltage, I is the charging current, and t is the charging time. The charging power was calculated to be 3.2 μW with the following formula.

$$P = \frac{1}{2} CU^2/t \tag{3.3}$$

where C is the capacitance, U is the voltage, and t is the charging time. The stored energy could be used to power a commercial calculator (Figure 3.19(c)). In real applications, because the force and speed of human motions can easily exceed the ones used in the tests, we can expect much higher energy harvesting amount to power larger electronics and generate more energy for storage.

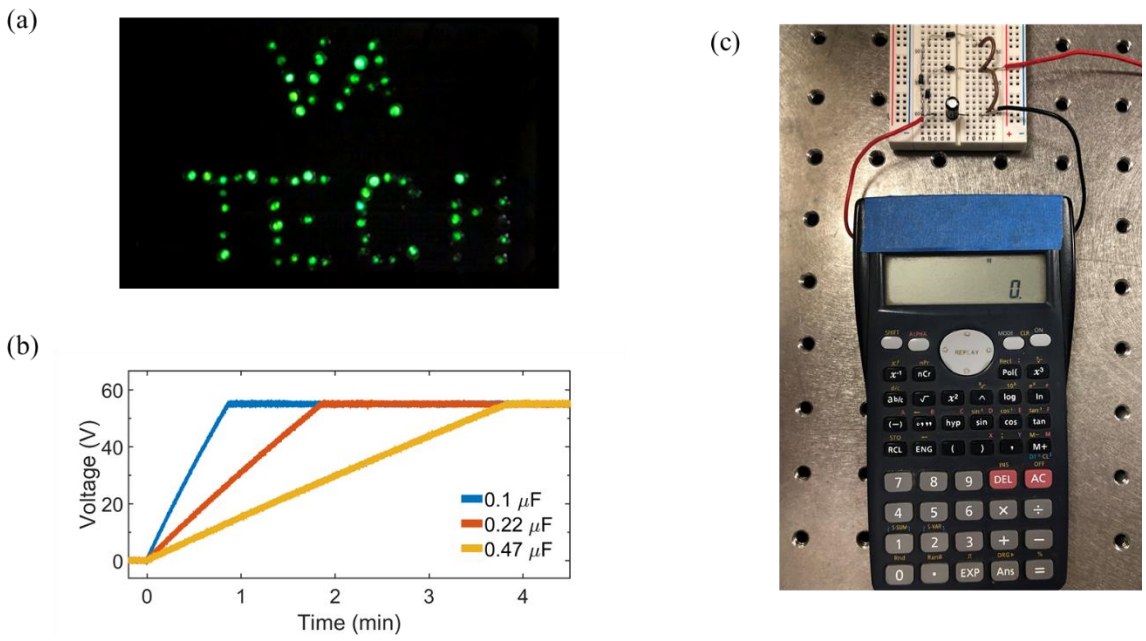

Figure 3.19 FTENGs works as power sources. a) A series of 62 commercial green LEDs lit up by rubbing a ~20 cm^2 textile on a cotton shirt. b) Charing curves of three commercial capacitors. c) Commercial calculator powered by the FTENG. The force applied was 70 N with an 8 Hz frequency.

3.5.2 Self-powered Sensors

FTENG allows for sensors to be distributed on multiple points of the body while being locally powered. Distributing sensors across the body has advantages over a lone sensor at one point on the body because it enables much finer-grained activity classification by monitoring the movements of different locations on the body.[166-170] Besides, the FTENG sensors offer more comfortability than the traditional accessory-based sensors, e.g., watches and glasses, because they are flexible and lightweight. We have demonstrated the self-powered sensors for bio-monitoring and communication uses. As can be seen in Figure 3.20(a), the FTENGs were mounted at the backside and the inner sides of the leg for movement sensing. At the inner side, the FTENG was used as a pedometer by sensing the relative movement between the two legs. Because the open-circuit voltage is proportional to the distance between the two legs, each step corresponds to a peak

in Figure 3.20(b). At the backside, the FTENG was used as a sitting timer by sensing the relative distance between the leg and the chair. When the leg approached the chair, the open-circuit voltage decreased accordingly, and vice versa. Users can also customize the threshold of the sitting voltages (Fig. 3.20(c)).

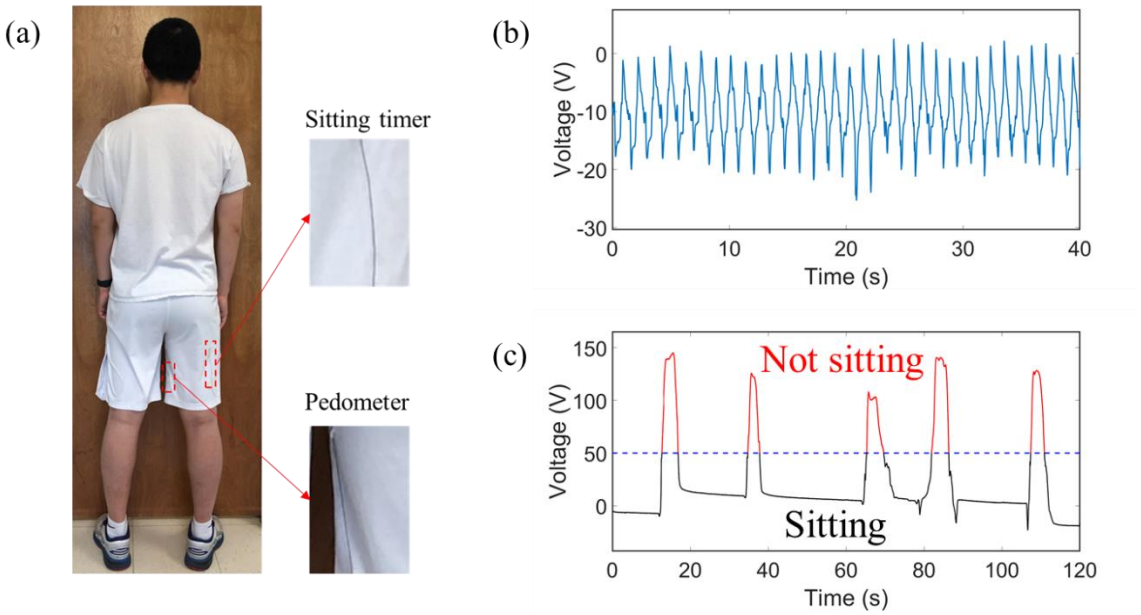

Figure 3.20 FTENGs working as wearable self-powered sensors (a)FTENG mounted on clothes (b) Pedometer signals (c) Sitting timer signals

Another typical self-powered FTENG sensor is to extract the Morse codes generated by tapping (Figure 3.21(a)). The dots and dashes in voltage curves can be controlled by the contacting time (Figure 3.21(b)). With the advantage of the length of the fiber, such a sensor will be useful for long-distance communication in emergencies (e.g., earthquake and oil well explosion) in which plant power and other electronics are damaged. In these cases, the FTENG-based self-powered sensors offer users accuracy, customization, comfortability, and security.

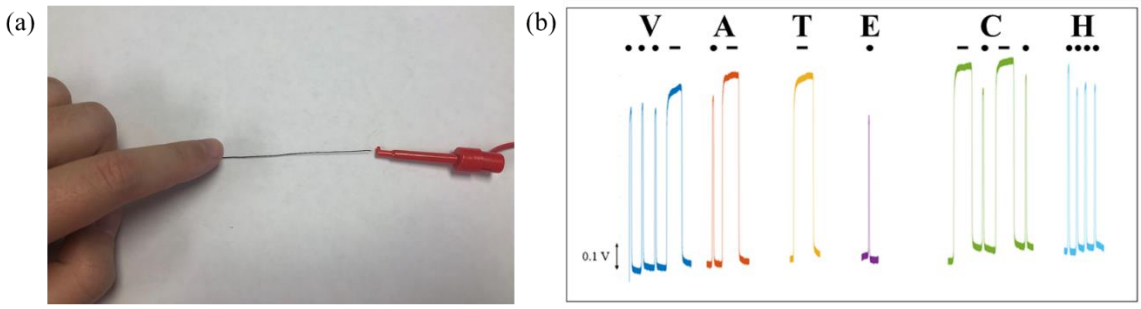

Figure 3.21 FTENG working as a Morse code generator for distributed deployment

3.6 Summary

In summary, the thermal drawing process is introduced to FTENG fabrication to bridge the gap between the FTENG and the weaving industry. We used an ultrathin metal wire core as the electrode and polymer cladding as the triboelectric material. The fiber's weavability has been significantly improved due to its small diameter, large scalability, and high productivity. The FTENG was ~350 μm diameter and ~100 m long. The drawing speed was up to 4 m min^{-1}. Both semicrystalline and amorphous materials have been successfully demonstrated as cladding materials in the thermal drawing. The broad options of materials could satisfy not only the electrical but also the aesthetic needs. The fibers were woven into flexible textiles and can be further tailored to clothes for wearable use.

The harvested energy was instantly released to light up 62 commercial LEDs and stored in a capacitor to power up a commercial calculator. The durability and washability tests showed that the electrical output was stable after 100,000 cycles and 5 washing cycles, and the textiles showed good breathability in the air permeability tests, ensuring its great potential for wearable applications. Serving as self-powered sensors, FTENG has the advantage of being mounted in various locations of the human body to be more user-friendly. It can be used to track the body

motions with good flexibility and lightweight. Also, it offers an efficient way for emergency communication while being almost imperceptible at other times. The thermally-drawn FTENG makes it possible to distributedly harvest energy and power up electronics. Its versatility as self-powered sensors offer a new direction for biological and communication use. What's more, it could realize these functions by seamlessly embedding itself in the clothes. Such a multifunctional device can serve people with great comfort in the era of IoTs.

Chapter 4 3D-Printed Conformal Stretchable FTENG-based Sensors

In the previous chapter, we reported a method for scalable production of FTENGs for textiles. The flat textiles can be tailored for general wearable use. However, in some situations, conformal structures are needed. 3D printing is a reliable method to produce devices with multiple shapes. In this chapter, we report a process for 3D-printed core-cladding FTENG and stretchable devices based on it. The devices can be printed in forms of mesh, hollow 3D structures, and membranes on planar, rotating, and non-planar anatomical substrates. The materials for the core and cladding are copper wire and elastomeric silicone rubbers. Because of the serpentine and helix structures of the copper wires and the internal elasticity of silicone, the devices and be stretchable.

Wearable mechanosensors for organ and human activity monitoring have been demonstrated. Specifically, the perfusion induced kidney edema can be monitored in real-time, and speech in the absence of sound production by the speaker (i.e., 'silent speech') can be recognized with machine learning-based signal demodulation. The devices are form-fitting to the applied organs. Overall, these sensors encourage the use of 3D-printed FTENG-based devices for self-powered sensing applications in biomanufacturing, medicine, and defense. [63]

4.1 State-of-the-art Conformal TENGs

In many applications, conformal structures are desired because they can offer high accuracy and more comfortability. While some of the organs are in regular shapes, e.g., circular wrists and relatively flat thighs, many of them are not, and they can differ significantly. For example, the

chins, palms, and kidneys have their unique contours. The state-of-the-art conformal TENGs are reviewed as follows.

Chu et al. designed conformal SETENGs that offer good adhesion to human skin. PET, graphene, and PDMS served as the substrate, electrode, and the triboelectric layer, respectively. The TENGs could be attached to a human palm and forearm for energy harvesting.[171] Yi et al. reported a scalable approach to fabricate the shape-adaptive TENG unit, in which the conductive liquid electrode was encapsulated by a rubber layer. Its good conformability was mainly due to the unique capability of liquid. The TENGs could be attached to a shoe and looped around a human arm.[172] Zheng et al. developed a multilayer CSTENG, in which magnesium films and biodegradable films served as electrodes and triboelectric surfaces, respectively. The TENG was mounted on the subdermal dorsal region of an SD rat for degradation test.[173] Pu et al. reported a soft skin-like TENG, in which PAAm-LiCl hydrogel was sealed between two elastomer films (PDMS or VHB). The VHB-based TENG could undertake a strain of 1000%. The skin-like TENG could be mounted on a curvy hand.[174] Liu et al. demonstrated a stretchable, deformable, and transformable TENG using shape memory polymer films. The conductive liquid was used as the electrode. The TENGs could be mounted on the side surface of a tube and a human wrist. The shape memory polymer could adapt to the mounting configurations.[175] Deng et al. developed a self-healable, flexible, and deformable TENG by combining a vitrimer elastomer film with a silver nanowire conducting network. The healing could be enabled on a demanded reconfiguration of shape by a thermal stimulus. 2D cross-shaped and 3D cube-shaped devices have been demonstrated.[176] Yu et al. reported a highly skin-conformal wearable tactile sensor based on piezoelectric-enhanced TENG. The triboelectric signals originated from the interaction between nonpolarized m-PZT&PDMS film and m-Cu. The sensor could be mounted on a human wrist to detect pulse and be mounted on

a computer mouse to detect finger motions.[177] Lan et al. fabricated a sandwich-structured stretchable TENG, where 1D silver nanowires and 2D metallic MoS_2 nanosheets were employed as the electrode. They were encapsulated in two layers of PDMS, which served as the triboelectric surfaces. The TENG could be attached to a plant leaf for wind speed monitoring.[178] Xiong et al. integrated a flexible light-weight encapsulated TENG into a self-powered system. Copper, Kapton, PTFE, and Al films were used as functional materials by the TENG. It could be mounted on the wrist to sense human pulses.[179] Park et al. demonstrated a one-step route for developing rapid wet-processable surface-conformal triboelectric nanoporous films. A heavily P-doped silicon substrate was used as the electrode, and FOTS self-assembled monolayers-coated PDMS elastomer films were used as the triboelectric surfaces. The nanoporous films could conformal to the attached surface, e.g., a human finger or a leaf.[180] Yu et al. reported a CSTENG consisting of ultra-flexible micro-frustum-array PDMS film and Cu electrodes. The TENG could achieve self-powered weak physiological singal monitoring with great comfort. It could be mounted on a plant leaf or on a human wrist.[181]

In summary, most of the state-of-the-art conformal TENGs are based on flexible films, such as PDMS and rubber ones. Because the employment of metal films may hinder the overall flexibility, conductive nanomaterials are used as electrodes. The size of the devices can be limited by the materials because the rubbers commonly need curing in ovens or desiccators with rigid substrates during the fabrication. The conformability is mainly dependent on how small the features can reach on the films. Even though some films are soft and flexible, when it is attached to an irregular surface, it is hard for the device to conform perfectly to it. Therefore, irregular shape-conformal TENGs are still yet to be produced.

4.2 3D-Printed FTENG

4.2.1 Fabrication of 3D-printed FTENG

Multi-material 3D printing processes have been leveraged extensively for the fabrication of structural electronics,[182-186] bionics,[187-190] and wearable devices[191-194]. For example, stereolithography processes have enabled the fabrication of gaming pieces composed of polymer-embedded electronics, including LEDs, microprocessors, accelerometers, and silver interconnects.[183] Micro-extrusion 3D printing processes have allowed the fabrication of bionic tissues and active 3D electronics, such as tissues that contain integrated stretchable antennas and lenses containing integrated light-emitting diodes, respectively.[187, 195] However, the use of conductive and functional inks poses challenges to the design and fabrication of 3D-printed triboelectric devices because of high resistance, high cost, high-temperature post-processing steps (e.g., sintering), and poor mechanical properties, including limited flexibility and durability under cyclical loading.[196] Thus, it is desirable to expand the conductive and functional materials palette for 3D printing processes. To overcome the limitations above, researchers have been exploring the feasibility of robotically interweaving high-quality drawn wires with 3D-printed constructs. For example, an integrated micro-extrusion 3D printing and pick-and-place process enabled the integration of platinum wires into silicone scaffolds, which was applied to the fabrication of custom-sized nerve cuffs.[197, 198] A fused deposition modeling (FDM) process with active wire integration capabilities was developed for encapsulating conductive metal wires in an extrudable matrix of styrene block copolymers.[196] While important from the perspective of integrating highly-conductive materials with 3D-printed constructs, the use of thermoplastics makes the process relatively unattractive from the perspective of fabricating triboelectric devices because of their poor performance as triboelectrically-negative materials and limited elasticity. In

contrast, silicone rubber, a widely 3D-printed material in micro-extrusion processes,[197-201] has been widely recognized as a promising candidate for use in triboelectric systems. It has a high electronegativity, temperature-independent properties, resilience, and elasticity, thus being a perfect material for wearable TENGs.[87, 202-205] However, it is currently difficult to achieve wire encapsulation within elastomeric materials.

Here, we present a 3D printing process for the production of copper-core silicone-cladding FTENG-based devices using a coaxial micro-extrusion method (Figure 4.1(a)). Fabrications of 1D fiber, 2D membranes, and 3D meshes and hollow structures are demonstrated on stationary and moving substrates(Figure 4.1 (b), (e), and (i)). The copper and silicone serve as the electrode and the triboelectric surface, respectively. The TENG can work in the vertical contact-separation mode or the single-electrode mode based on the external circuit connection. The coaxial multi-material micro extrusion process of the basic FTENG can be seen in Figure 4.1(b). The 3D printing system consisted of a three-axis robot (MPS75SL; Aerotech), a digital pressure regulator (Ultimus V; Nordson), a motion controller (A3200; Aerotech), and a coaxial extrusion nozzle (i.e., dispensing barrel-manifold assembly). Cu wire (36 AWG), which served as the metallic core material, was first loaded on the top portion of the manifold. The preloaded manifold was then transferred into a dispensing barrel (10 cc; Nordson EFD) with an 18-gauge tapered tip. Silicone, which served as the elastomeric cladding material, was subsequently loaded in the coaxial extrusion barrel. Prior to printing, the metal core was anchored on the substrate by locally curing the cladding. FTENGs were printed by a continuous extrusion of silicone using a pressure of 15 psi at a constant vertical feed rate of 2 mm s^{-1}. Following printing, the fibers were cured at room temperature. Fibers of varying compositions were fabricated by changing the core material (28 AWG Al wire and 40 AWG Cu wire) and the printing nozzle diameter (16- and 20-gauge tapered tips) and appropriately

modulating the extrusion pressure in the range of 10–20 psi. A photograph of the 3D-printed silicone-Cu fiber and micrograph of the fiber cross-section are shown in Figure 4.1(c) and (d), respectively. The fiber is highly flexible because of the low bending modulus of the Cu wire and the high elasticity of the silicone cladding. The fiber diameter (840 ± 8 μm) reasonably approximates the nozzle's inner diameter (838 μm), indicating a minimal die-swell effect during extrusion.

Customized manifolds for 3D printing of FTENG were designed with a computer-aided design (CAD) software (Onshape). Each manifold was designed as a hollow two-part structure. The top and bottom portions of the manifold served as a source of wire (core material) and die for passive wire feeding based on drag extruded silicone that surrounded the wire, respectively. The bottom portion of the manifold also served to provide structural integration with the surrounding dispensing barrel in which the elastomer was contained (Figure 4.2(a)). The 3D design and engineering drawing of the customized manifold are shown in Figure 4.2(b) and (c). The manifolds were fabricated using a commercial desktop 3D printer (LulzBot mini 2; LulzBot) using vendor-provided slicing software (Cura; LulzBot) and protocols (Figure 4.2(d) and (e)).

In addition to 1D FTENG printed on planar stationary substrates, higher dimensional devices were printed on continuously rotating substrates. As shown in Figure 4.1e, FENGs printed on continuously rotating mandrels enabled the fabrication of 3D hollow structures, including cylinders and cones (Figure 4.1(f) and (g)). The process was scalable through modification of the mandrel diameter, thus enabling the fabrication of wearable systems, such as the wristbands shown in Figure 4.1(h). Similarly, cuboid- and star-shaped structures (Figure 4.1 (i-k)) can be printed on planar stationary substrates that contained distributed anchors. The CAD design of customized substrates with anchor pins are shown in Figure 4.2 (f-h). In practice, conformal TENGs can be

realized on substrates with irregular shapes. We have printed a 2D film that can be mounted on the human chin and a 3D spacious mesh that is conformal to a kidney. The details will be presented in sections 4.3 and 4.4.

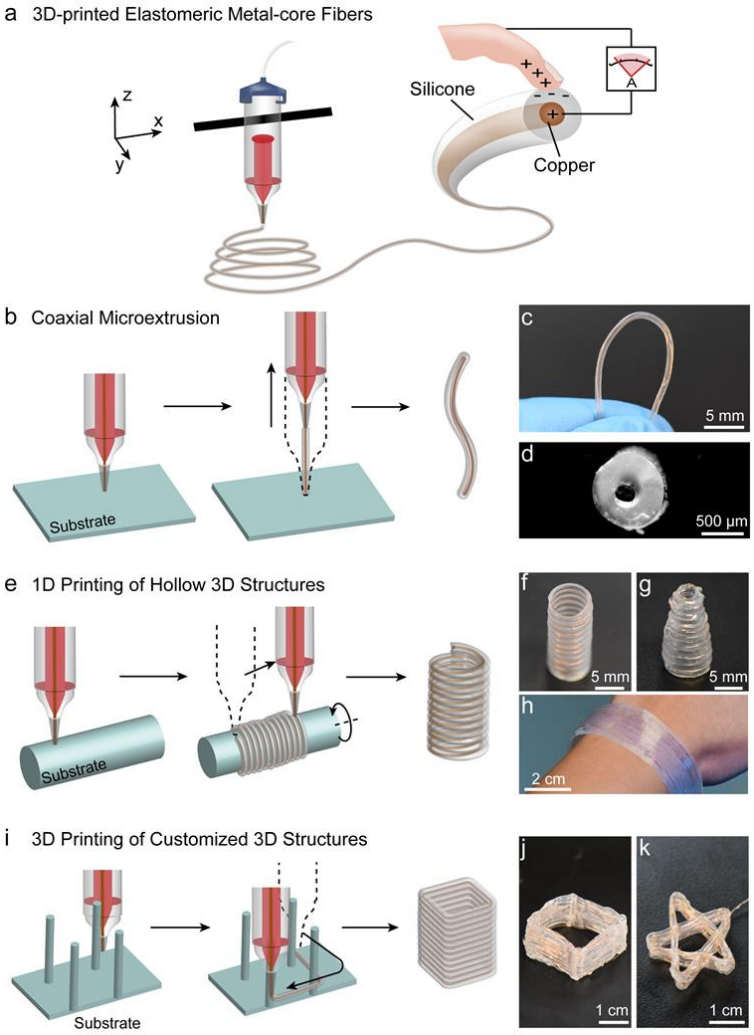

Figure 4.1 Description of the 3D Printing process of the FTENG. (a) Concept of 3D printing Cu/silicone FTENG (b) Schematic illustrating micro-extrusion 3D printing of Cu/silicone fibers through a terminal anchoring process. (c) Photographs of flexible 3D-printed FTENG. (d) Micrograph of the fiber cross-section. (e) Schematic illustrating the fabrication of 3D hollow structures via 3D printing on continuously rotating substrates. Photographs of 3D-printed (f) hollow cylinder and (g) cone triboelectric constructs. (h) Demonstration of device scalability through the fabrication of triboelectric wristbands. (i) Schematic illustrating 3D printing on planar substrates containing distributed anchors. Photographs of 3D-printed triboelectric (j) cuboid- and (k) star-shaped structures.

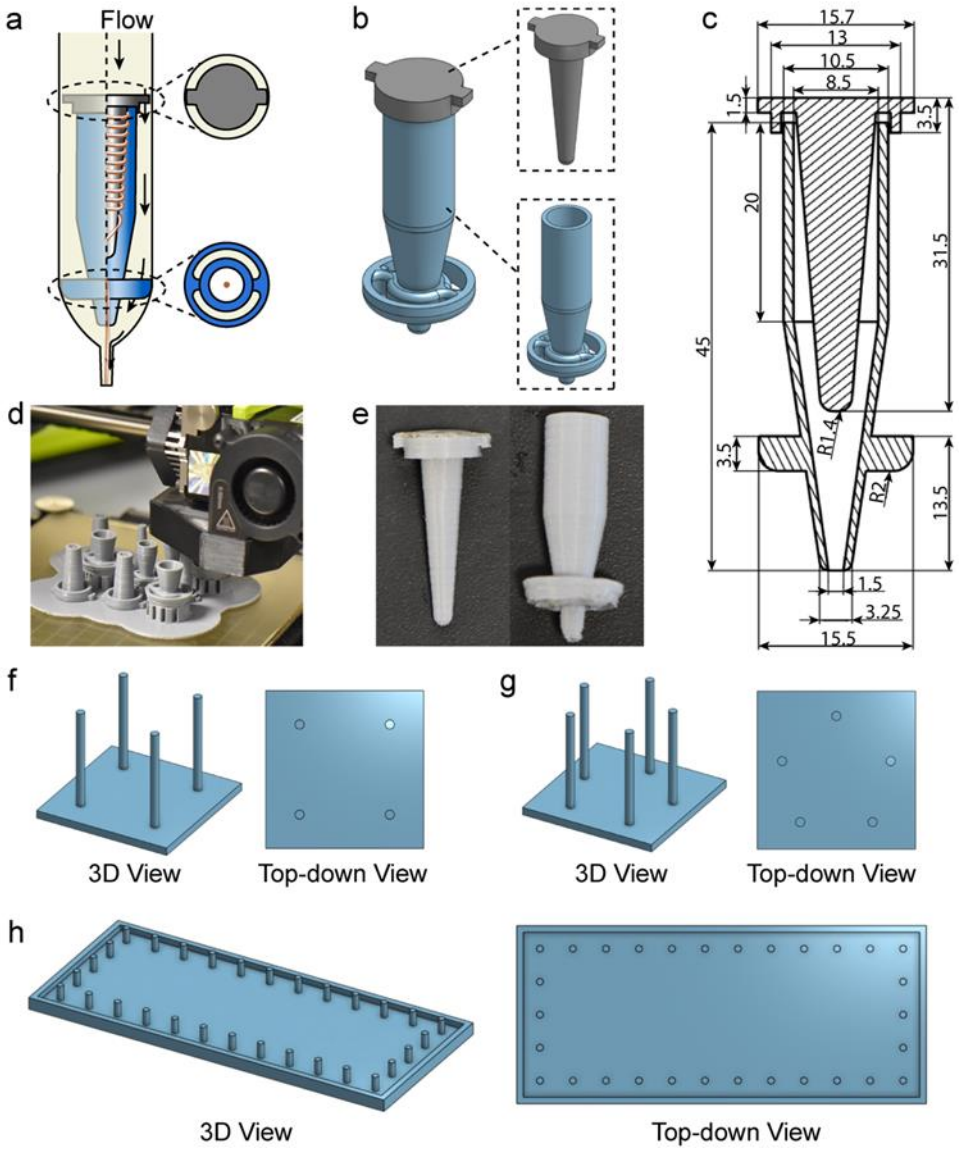

Figure 4.2 Design of Customized Manifolds and Printing Substrates. (a) Schematic of the mechanism of coaxial fiber microextrusion with customized manifolds. (b) CAD model of the two-part customized manifolds. (c) Design drawing of the assembled customized manifolds. (d) Photographs of the fabrication process and (e) the finished customized manifolds. CAD design of customized substrates with anchor pins for fabricating (f) cuboid-, (g) star-shaped 3D structures, and (h) fiber-based sensing pads.

4.2.2 Electrical performance of 3D-printed FTENG

As wearable triboelectric mechanosensors described in the following sections, the Cu wire was directly connected to the test samples (e.g., the skin or the organ), and the triboelectric fiber worked in the contact-separation mode. The working mechanism is shown in Figure 4.3(a). The skin served as one of the triboelectric material and the ground, and the silicone cladding of the FTENG served as the other triboelectric material. As can be seen in Figure 4.3(a), contact between the skin and silicone results in electrons in the skin being transferred to silicone because the latter lies in a more negative location in the triboelectric series. When the skin moves away, the accumulated negative charges on silicone induce a positive charge in the Cu wire for compensation, creating a current flowing from the skin to the fiber. Similarly, when the skin re-contacts the silicone, the current returns to the skin. No current is present when equilibrium is reached. Thus, triboelectric fibers generate alternating current associated with repetitive triboelectric charge transfer cycles, during which the electrical potential of the Cu wire increases with decreasing separation distance between the two triboelectric materials (i.e., skin and silicone). The amplitude of the induced current depends on the amount of the transferred charge and the frequency of the contact event. The numerical finite element simulation of the working mechanism by COMSOL is shown in Figure 4.3(b).

The triboelectric responses of a single FTENG (diameter = 700 μm; length = 2.5 cm) and 3D-printed wristbands (testing contact area = 1 × 1 cm^2) were quantified with cyclic loading tests. A schematic of the apparatus and the circuit connection are provided in Figure 4.5(a) and (b), respectively. The short-circuit current (I_{SC}), transferred charge (Q), and open-circuit voltage (V_{OC}) are provided in Figure 4.3(c)–(e) and Figure 4.4(a)-(c), respectively. The single fibers exhibited I_{SC}, V_{OC}, and Q maxima of 0.38 μA, 5.75 V, and 2.65 nC, respectively, while the wristbands

exhibited maxima of 0.46 μA, 8.01 V, and 3.97 nC, respectively. Studies were also conducted using various loads to examine the corresponding power density (*PD*). The corresponding *PD* was calculated as $PD = I^2R/A$, where *I* is current, *R* is the resistance of the external load, and *A* is the contact area. As can be seen in Figure 4.3(f) and 4.4(d), the single FTENG fibers and wristbands exhibit maximum *PD*s of 31.39 and 23.94 mW m^{-2}, respectively. The decreased maximum *PD* of the wristband relative to the single fiber is associated with the wristband's relatively decreased Cu-to-silicone volume ratio, which caused a relatively lower induced charge for the same loading conditions.

To further verify the durability of the 3D-printed TENG fibers, we conducted a 5000-cycle loading test using a force amplitude of 50 N. We selected 50 N based on its established use as the upper limit of the dynamic range associated with force sensors for human motion monitoring applications.[206-208] As shown in Figure 4.3(g), no visible decay in I_{SC} was observed after 5000 loading cycles, which indicated that the FTENG and 3D-printed constructs could serve as reliable transducers for sensing and energy harvesting applications.

A single FTENG was used to charge commercial capacitors. The circuit and charging curves are shown in Figure 4.3(h) and (i), respectively. The voltage saturated at 55 V after 4.5 min and 10.1 min for the 0.1 and 0.22 μF capacitors, respectively. The generated energy could also be consumed instantaneously. In Figure 4.3(j), 20 commercial LEDs could be lit up. Given biomedical applications may establish humid testing environments, we also investigated the effect of humidity on the fiber output. The experimental apparatus and fiber responses are shown in Figure 4.5(c) and (d), respectively. Changes in relative humidity caused a minimal effect on the maximum I_{SC}, which decreased from 0.41 to 0.35 μA upon a relative humidity increase from 20% to 70%. Importantly, the fiber remained functional in the presence of humid environments.

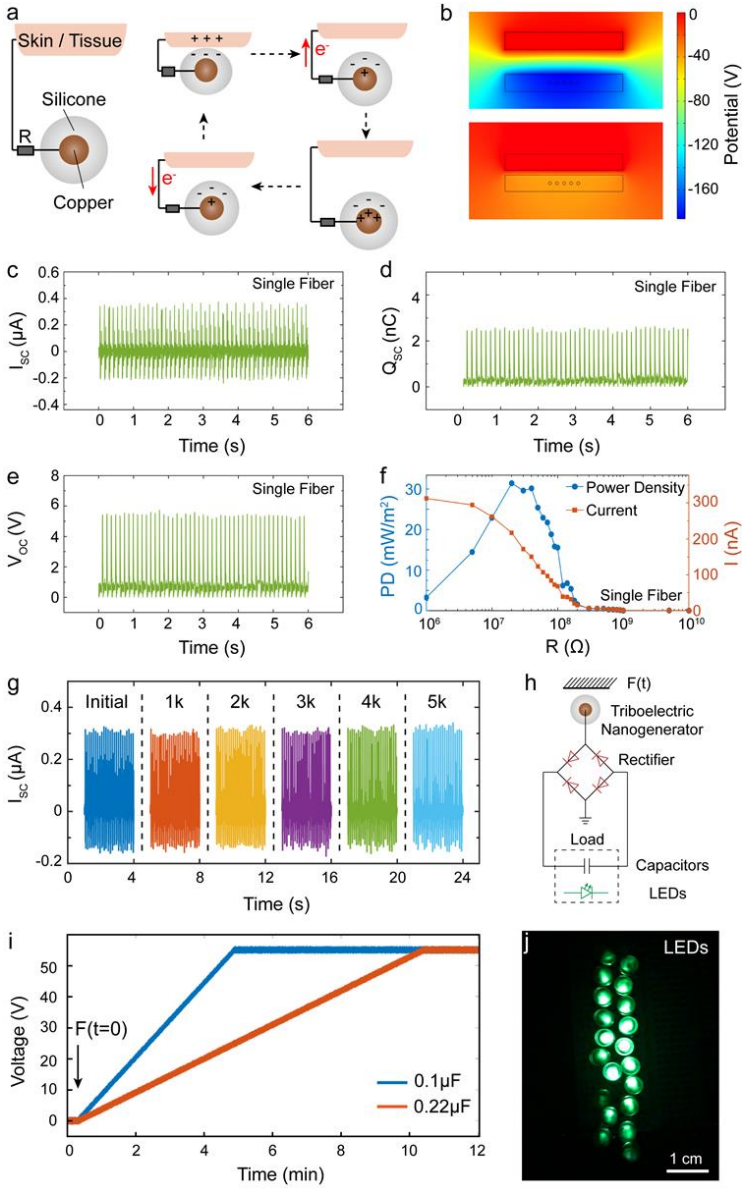

Figure 4.3 Characterization of the electrical output of 3D-printed FTENG (a) Schematic illustrating the working mechanism of the FTENG in the contact-separation mode. (b) Numerical simulation of the electrical potential distribution created upon dynamic contact-separation of silicone and skin. (c-e) Short-circuit current, transferred charge, and open-circuit voltage of the FTENG. (f) Current generated for different external loads and corresponding power densities. (g) Short-circuit current generated in the durability tests. (h) Circuit for charging capacitors and lighting up LEDs with FTENG. (i) Charging curves for two commercial capacitors using a single FTENG. (j) Photograph showing powering of 20 LEDs using a single FTENG.

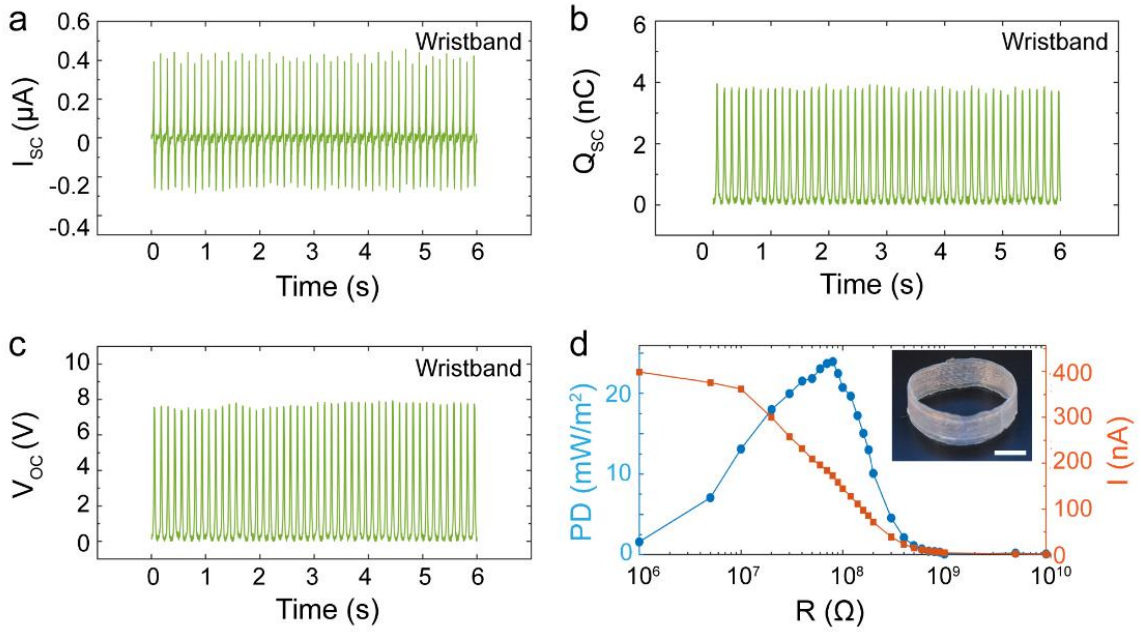

Figure 4.4 Electrical performance of a 3D-printed Wristband. (a) I_{SC}, (b) Q_{SC}, and (c) V_{OC} of the 3D-printed TENG. (d) Currents with different external loads and corresponding power densities.（scale bar = 2 cm). The contact area was ~100 mm^2.

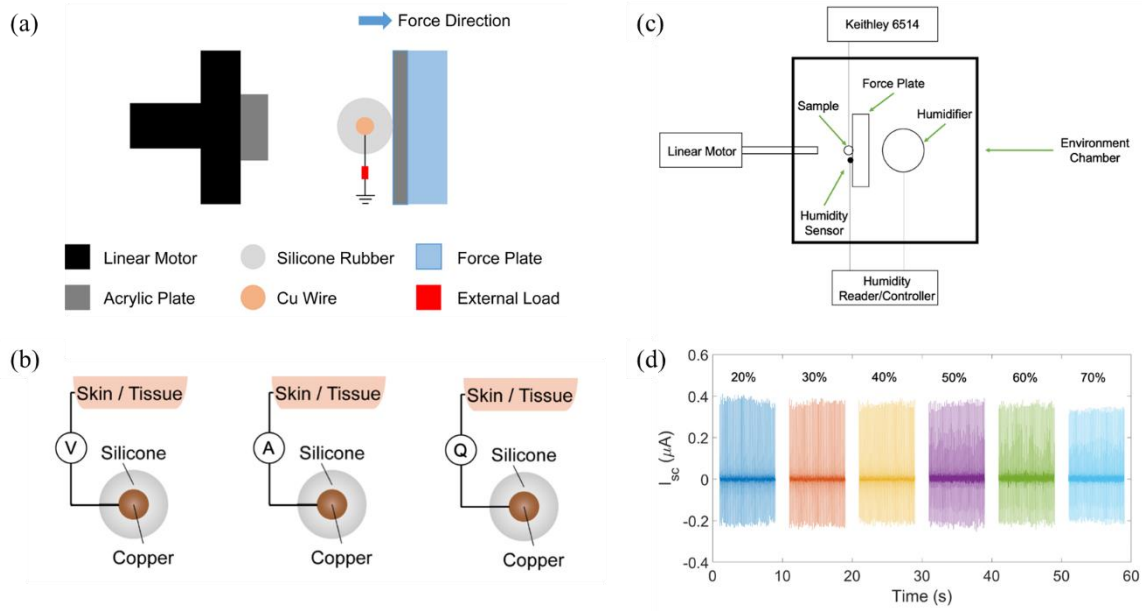

Figure 4.5 (a) Apparatus for cyclic testing of FTENGs. (b) Connection of testing circuit in the cyclic tests. (c) Apparatus for cyclic testing of FTENGs with humidity changes. (d) I_{SC} in the cyclic tests under different humidities.

4.3 Self-powered Flexible Silent Communication Sensor

'Silent communication', also referred to as 'silent speech' or 'silent talk', is defined as sound-free communication among humans.[209] We investigated if a wearable 3D-printed triboelectric device could reliably detect and classify user speech in the absence of sound production by the speaker without the use of image-based facial expression monitoring.

4.3.1 FTENG-based Flexible and Stretchable Membrane

FTENG-based membrane was printed on a planar substrate (Figure 4.2(h)) that contained a 50 × 120 × 3 mm^3 cavity and 30 edge anchors using an 18- gauge tapered tip, extrusion pressure of 15 psi, and printing speed of 2 mm s^{-1}. The toolpath consisted of a zig-zag pattern with a 45-degree inclination relative to the substrate edge. An additional layer of silicone was printed on top of the patch to smoothen the surface. The printed structures were cured overnight prior to release from the substrates.

As shown in Figure 4.6(a), the integration of a 3D-printed FTENG-based membrane (1.8 mm thick) in a surgical mask provided effective mechanical coupling between the device and the speaker's face. Movement of the user's face caused membrane deformation and thus changed in the device-skin contact area. Interwoven 3D-printed TENG fibers enabled the transduction of facial movements associated with silent speech to electrical response through the triboelectric effect (i.e., I_{SC}) (Figure 4.6(b) and (c)).

As shown in Figure 4.6(d) and (e), the 3D-printed membrane exhibited an elastic response up to engineering strains of ~20% in both vertical and horizontal directions. In contrast to single fibers, which were highly flexible but exhibited limited stretchability constrained by the elasticity of the metal copper, 3D-printed constructs could be printed with tool-paths that resulted in highly

stretchable devices (e.g., serpentine patterns). The mechanical properties of the FTENG-based membranes obtained from tensile testing studies (Young's modulus and UTS) are provided in Table 4.1 and agreed with previously reported properties of 3D-printed silicone membranes.[199]

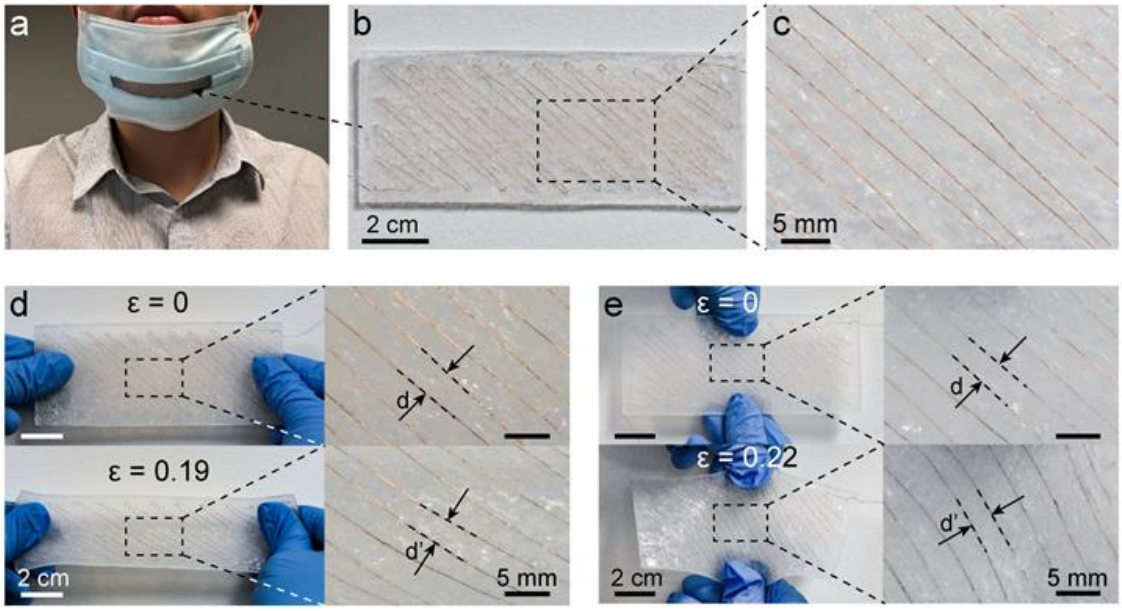

Figure 4.6 3D-printed stretchable wearable FTENG-based membrane for 'Silent communication' recognition (a) Photograph of a human subject wearing the triboelectric membrane-integrated facemask. (b) Photograph of the stretchable FTENG-based membrane's integrated transduction elements (TENG fibers) with a zoomed view (c). (d) and (e) Highlights of the FTENG-based membrane orthogonal stretchability with zoomed views showing fiber orientation in the absence and presence of strain.

Table 4.1 Mechanical properties of TENG membranes obtained from tensile testing (n = 3 samples). The referred values are from ref[199].

	Young's Modulus (MPa)	Ref.	UTS (MPa)	Ref.	Strain at Failure	Ref.
TENG Membrane	0.53 ± 0.07	0.44	0.25 ± 0.06	0.25	0.96 ± 0.04	1.5

4.3.2 Silent Communication Sensing

When the user puts on the membrane-loaded mask (Figure 4.6(a)), there will be unique signals of short-circuit current with different muscle motions of the chin. Therefore, the user does not need to speak with sound to generate signals for communication. Instead, the user just needs to pretend to be talking by moving the mouth and chin without making any sound. The current signals generated by the user's facial movements were subsequently used for real-time speech recognition via filtering, feature extraction, and classification based on the silent word spoken (the computational framework associated with speech classification is provided in Figure 4.8. Figure 4.7(a)-(c) show the data corresponding to the user speaking the number "*three*," the letter "*D*," and the word "*print*" silently. Each sound produced a distinguishable waveform, suggesting that the platform may provide opportunities for silent speech-based communication by combination with time-series data classification methods. The observation of distinguishable signals associated with each of the three sounds (*three*, *D*, *print*) was consistent among multiple human subjects (n=3).

We trained various supervised machine learning models to classify each word that was silently spoken, including Linear Discriminant Analysis, Linear Support Vector Machine (SVM), Quadratic SVM, Gaussian SVM, and K-nearest Neighbors models. Various models, including Linear SVM, Quadratic SVM, Gaussian SVM, and K-nearest Neighbors, enabled recognition of the silently spoken word with greater than 95% accuracy. The Linear Discriminant Analysis model exhibited the lowest word classification accuracy of 74.8%. The Quadratic SVM, Linear SVM, and K-nearest Neighbor models exhibited relatively higher word classification accuracies of 98.4, 98.4, and 98.1%, respectively. The Gaussian SVM model yielded the highest word classification accuracy of 99.2%. Figure 4.7(d) illustrates the effect of the training sample size on the word

classification accuracy for the Gaussian SVM model. Word classification accuracies exceed 95% accuracy for training sample sizes greater than 85 samples.

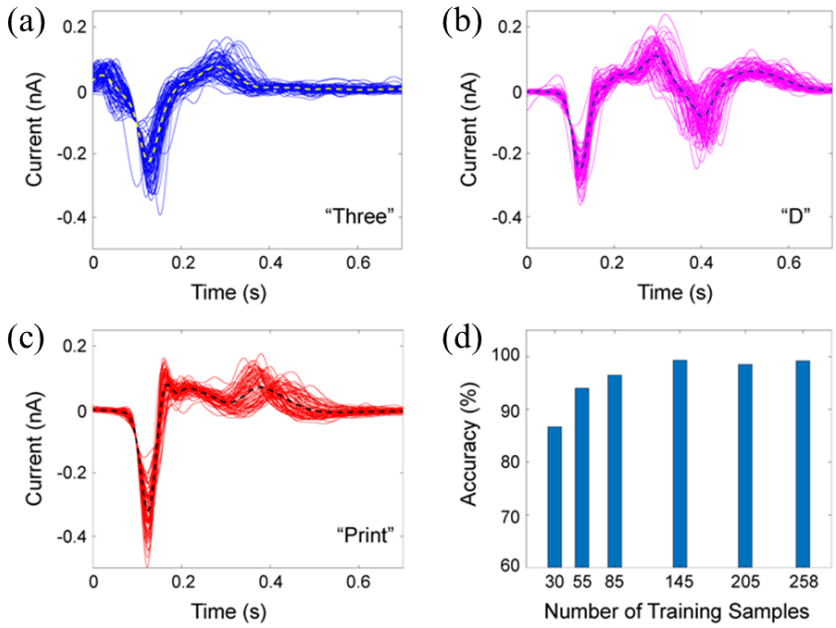

Figure 4.7 Filtered and averaged (dotted line) short-circuit current signals corresponding to silently speaking (a) the number "*three*" (b) the letter "*D*" and (c) the word "*print.*" (d) Accuracy of the online classification system for different training sample sizes.

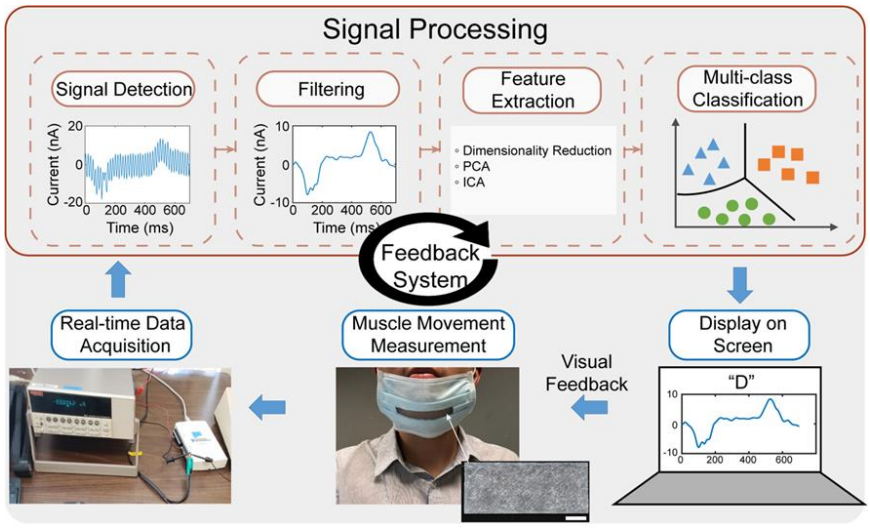

Figure 4.8 Framework of Signal Processing for Real-time Silent Communication（scale bar: 2 cm)

4.4 Self-powered Kidney-conforming Preservation Sensor

We next examined if the response of FTENG-based devices could enable sensing of mechanical motions associated with perfusion-induced organ edema, a significant problem encountered in *ex vivo* machine perfusion-based organ preservation processes.[210, 211] In addition to a suite of conformal bioanalytical devices for non-invasive isolation of biomarkers from perfused organs and biosensors for compositional analysis of perfusate and microfluidic biopsy samples,[201] next-generation *ex vivo* machine perfusion systems by necessity should incorporate low-power sensors for real-time monitoring of organ edema (i.e., swelling).

FTENG-based mesh sensors for organ monitoring studies were conformally printed on 3D-printed models of porcine kidneys.[201] Conformal tool paths were manually programmed based on uniform mesh geometry that spanned the bottom half of the kidney. Glass pins were mounted to the kidney model to provide fiber anchor points within the non-planar tool path. Printing was performed using an 18-gauge tapered tip, extrusion pressure of 15 psi, and printing speed of 2 mm s^{-1}. The printed structures were cured overnight prior to release from the substrates.

As shown in Figure 4.9(a)–(c), the process enabled the fabrication of an organ-conforming mesh-based triboelectric mechanosensor by conformal 3D printing of TENG fibers on anatomical models of porcine kidneys. During the perfusion test, the contact area between the mesh and the kidney dynamically change for three reasons. First, natural variance in the size and shape of kidneys from different animals establishes unavoidable discontinuities (i.e., gaps) between the mesh and the kidneys that were tested (i.e., while the mesh geometry was indeed fabricated based on a porcine kidney template, the kidney used for templating was not the same as the kidneys used for testing). Second, the fiber surfaces contain inherent variance in surface topography. Third, the organ and the silicone cladding can deform due to perfusion-induced increases in contact force.

Such swelling-associated changes in the organ-mesh contact area drove electron transfer between perfused kidney and the form-fitting triboelectric sensor, thus changing the electrical potential distribution.

As shown in Figure 4.9(d) (point cloud data), the perfused kidneys swelled ~ 20% in height over the course of a 2-h normothermic machine-perfusion interval. As shown in Figure 4.9(e), the real-time V_{OC} response of the sensor agreed reasonably with the surface displacement measured by 3D scanning (*i.e.,* point cloud data) throughout the preservation interval, which contained a 5-min baseline equilibration period (with no perfusion) followed by a 1-hour machine perfusion period. Following the 1-hour perfusion period, the perfusate flow was stopped, and the kidney was continuously monitored throughout a further 1-h post-perfusion period. Both the sensor V_{OC} and the kidney surface displacement increased monotonically throughout the preservation period. Stopping the perfusate flow caused a continuous decrease in both signals over the course of the next 6 min. V_{OC} increased to a maximum of ~70 V, which occurred at the end of the perfusion period, and ultimately stabilized at ~20 V at $t \approx 120$ min. Kidney displacement increased by a maximum of 32.7%, which similarly occurred at the end of the perfusion period, and decreased to a value of 19.7% at the end of the post-perfusion period and in the absence of perfusate flow. While the total surface displacement and the voltage response reached a maximum value when the perfusate flow was stopped, the voltage response of the TENG mesh stabilized ~10 min prior to the maximum of total surface displacement. This result could be attributed to various factors, including reaching the upper limit of the TENG device dynamic range, change in the mechanisms by which total surface displacement affects change in the device-organ contact area, or sensitivity of the TENG device to other perfusion-induced physiological changes in the perfused kidney (such as perfusion-induced injury). Given the organ swelling response was analyzed in terms of a total

surface displacement, we attribute the discrepancy in rates of decrease in the sensor response and total surface displacement to changes in the top region of the kidney that did not couple with the change in the device-organ contact area. In summary, the data in Figure 4.9(e) suggest that 3D-printed form-fitting constructs composed of FTENGs provide attractive self-powered, wearable mechanosensors for organ preservation and biomanufacturing applications, specifically real-time sensing of perfusion-induced edema.

Perfused kidneys were continuously imaged from a top-down perspective over the course of the perfusion process using a single camera-projector structured-light scanning system (HP 3D Structured Light Scanner Pro S3; HP). The system was calibrated in advance following vendor-provided protocols using a 60 mm calibration grid. Scans were collected every 2 min throughout the perfusion process, which resulted in a set of point clouds that quantify the out-of-plane displacement of the kidney during perfusion. The transient displacement was calculated as the distance between the first scan and subsequent scans. Quantification of the separation distance between two point clouds was performed using a commercially-available 3D CAD modeling software (Rhino 6; Rhinoceros). Specifically, a point object (P) was manually created above the point clouds (S_i), which marked the location of the midpoint of the organ in the x- and y-axes based on top-down projection. Following projection of the same point on each scan using the Project command (*i. e.*, the projection of point P on scan S_i resulted in the point P_i), the absolute organ surface displacement (d) of scan S_i was then defined as the distance between the projected point P_i and P_0, where P_0 is the projection of point P on the initial scan S_0. The initial organ surface level (h) was defined as the distance between P_0 and the height of the substrate on which the organ was resting as identified from the scanning data. Thus, the relative surface displacement was calculated as the ratio of the absolute height change to the original height (*i.e.*, $\frac{d}{h} \times 100\%$).

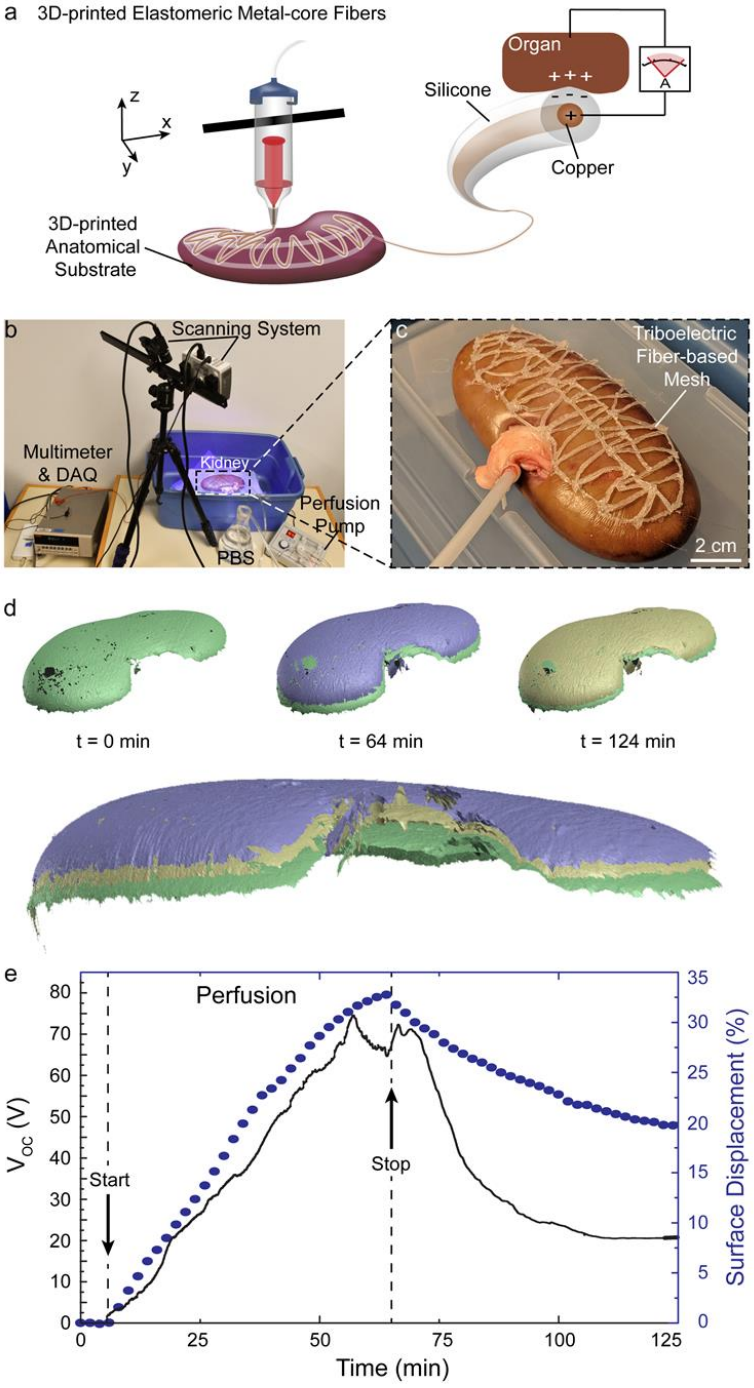

Figure 4.9 Form-fitting organ-conforming flexible and stretchable FTENG-based mesh for monitoring of perfused organs. (a) Schematic illustrating conformal 3D printing FTENG on objects with organic shape, specifically, a 3D-printed porcine kidney model, for fabrication of form-fitting wearable triboelectric devices. (b) Photograph of the custom machine perfusion apparatus. (c) Photograph of the 3D-printed kidney-conforming TENG fiber-based mesh sensor. (d) Representative point cloud data acquired via 3D scanning of perfused porcine kidneys at t = 0 (green), 64 (purple), and 124 min (yellow). (e) Real-time responses of organ displacement associated with perfusion-induced edema acquired using 3D scanning shown with the corresponding V_{OC} response of the 3D-printed FTENG-based mesh sensor.

4.5 Discussion

The coaxial micro-extrusion wire encapsulation process provides a unique capability for producing fibers with elastomeric claddings. Silicone and Cu were selected as the cladding and core, respectively. The 3D-printed conformal mesh also exhibits advantages relative to the use of shape-adaptive membrane TENGs for organ monitoring applications. Firstly, while shape-adaptive membranes can conform to objects with simple organic shapes, such as the arm, they must be crumpled or folded to conform with objects that exhibit complex organic shapes, such as internal organs. In contrast, the 3D-printed conformal mesh can fit accurately with objects that exhibit complex organic shape as they are fabricated based on a template of the object. Secondly, conductive liquids or coated metal nanowires are usually employed as electrodes to maintain both elasticity and conductivity in shape-adaptive membranes, which increases the device cost and internal resistance. Alternatively, the elasticity resides in the space between adjacent fibers for the case of the 3D-printed TENG mesh, which enables the metal core to serve as the electrode and results in a relatively decreased device cost and internal resistance. Thus, elastomeric metal-core silicone-Cu TENG fibers provide attractive material properties for wearable triboelectric systems. In addition to the large negative charge of silicone, making it an excellent candidate for triboelectric devices, silicone is an elastomer, which offers desirable mechanical properties in resultant fibers and devices. Silicone claddings also offer improved biomechanical matching characteristics relative to other fibers. For example, Young's modulus of silicone is 440 kPa, which is in the range of Young's modulus of skin (E=420–850 kPa) [212] and lower than other thermoplastic claddings, such as polysulfone (E≈2,600 kPa). The rheological properties of elastomers make them excellent candidates for micro-extrusion 3D printing. For example, elastomers can exhibit Herschel-Bulkley rheological properties, defined as a power-law fluid with

yield stress. Uncured silicone elastomers can exhibit yield stresses that are sufficient to enable 3D printing of free-standing constructs. In addition to desirable rheological properties, silicone also exhibits high self-adhesion and substrate adhesion, which facilitates layer-by-layer assembly of 3D structures and conformal 3D printing, respectively. As shown in Figures 4.1 and 4.9, silicone-Cu TENG fibers can be assembled into various structures and form factors via 3D printing, including 3D constructs and form-fitting systems. Considering the material and mechanical properties of the silicone-Cu TENG fiber systems, this work represents an advance in 3D printing of fiber-based functional materials and devices, which commonly exhibit single-fiber or woven device formats composed of fibers with relatively more rigid thermoplastic claddings. The continued, unmet demand for high-quality transplantable organs, such as kidneys, remains a driving force for the creation of novel organ preservation processes and sensors for real-time monitoring of organs,[213] from real-time organ bioanalysis to real-time characterization of organ biophysical and mechanical properties. Perfusion-induced organ edema (swelling) remains an important problem for organ preservation. While edema during the reperfusion phase is expected, excessive edema is detrimental to organ health.[214] Kidneys, as highly vascularized organs, will swell during perfusion caused by the reintroduction of fluid and tissue edema. In Fig. 3, we showed that 3D-printed TENG fiber-based meshes enabled real-time monitoring of machine perfused kidney swelling response (up to increases of 32.7%). The observed swelling response associated with perfusion-induced edema is consistent with previous reports.[214] The advantages of this 3D-printed triboelectric sensor in an organ preservation setting are self-powering capability, form-fitting design, and a real-time monitoring capability (sampling rate=1 kHz). The detection of organ swelling during machine perfusion could allow interventions that may lead to better organ preservation. Systems for silent communication, such as silent speech interfaces, have various

applications, including assisted communication among the soldiers and individuals affected by speech-related disabilities.[209, 215] A silent speech interface is traditionally defined as a device that allows speech communication without using the sound made when individuals vocalize their speech sounds, regardless of whether the sound is produced. The most commonly used silent speech interfaces are based on simultaneous monitoring of sound production and facial expression. Thus, they require high-dimensional image data and image processing methods, which are typically computationally intensive, as well as the use of imaging systems for facial monitoring, which increases power demands, creates the need for conventional power supplies, and limits system portability and human integration. Alternatively, 3D-printed silicone-Cu TENG fiber-based devices provide a self-powered wearable system for silent speech that offers various advantages, such as those associated with wearability, durability, power consumption, and compatibility with data-driven signal processing methods, such as machine learning. Overall, 3D-printed silicone-Cu TENG fiber-based devices provide attractive systems for silent speech without the need for sound production or image-based facial expression monitoring.

Chapter 5 Summary

The wearable triboelectric nanogenerators have proven to be reliable components as distributed power sources and self-powered sensors. They can complete the energy structure in the era of the Internet of things with traditional power plants. To increase the scalability, wearability, and functionality of the TENGs, we have introduced two methods to fabricate the fiber-based TENGs, namely the thermal drawing process and coaxial 3D printing.

By leveraging the thermal drawing process, we have designed and fabricated scalable, washable, and lightweight triboelectric-energy-generating fibers for industrial loom weaving. The common issues in traditional FTENGs are addressed. The diameter of the fiber is controllable and can be scaled down to 350 μm. The length of a single fiber can be scaled up to 200 m. The fabrication speed could reach 4 m min^{-1}. With these properties, the thermally drawn fiber has bridged the gap between the FTENG and the industrial looms. The demonstrated woven textiles expressed excellent flexibility, stretchability, power density, stability, washability, and breathability, thus being perfect wearable TENGs. These devices have been demonstrated as distributed power sources and self-powered sensors, which are essential in the IoTs.

Because conformal devices could lead to higher accuracy and better user experience, they are attractive in wearable systems. Though the film-based ones could offer flexibility and stretchability, the irregular shapes can hardly be perfectly form-fitted. We have introduced the 3D printing technique to fabricated conformal devices that are based on the 1D coaxial FTENG. Both 2D pad and 3D meshes have been demonstrated. The 2D pad was loaded to a commercial surgical mask to sense the facial movement for real-time silent communication, aiding users that have vocal problems. With the machine learning technique, we have demonstrated an accuracy of ~99% in

identifying three words. The 3D mesh printed on a kidney model is highly conformal to the real organ, and it has been used to monitor the perfusion rate in real-time, increasing the sampling rate by ~1,000 times.

For future works, there remain many directions to explore for FTENG fabrications and applications. Firstly, advanced materials can be used in FTENG. For example, stretchable polymers, such as the thermoplastic elastomer, and soft electrodes, such as conductive polymers and liquids, can enhance the stretchability of a single fiber. These stretchable fibers will be attractive in wearable devices and robotic systems. Secondly, thermally drawn FTENG with more sophisticated structures are to be developed for multiple purposes. Based on the deployment environment, the FTENG may generate more energy in specific working modes. For example, when the fiber is immersed in water, charge transfer can hardly occur on the fiber surface, so the single electrode mode FTENG cannot work typically. However, contact-separation mode FTENG can still work if there is a hollow channel inside the fiber. While it will be difficult and time-consuming to fabricate the FTENG with sophisticated structures with methods like extrusion, the thermal drawing method can deliver mass production. Thirdly, conformal devices that can be used on objects with entirely irregular shapes are still challenging to fabricate, especially those with subtle structures. The sizes of the basic unit need to be further reduced. Therefore, the materials need to be more miniaturized, and the controls in the fabrication need to be more accurate.

References

1. Fernández-Caramés, T.M. and P. Fraga-Lamas, *Towards the Internet of smart clothing: A review on IoT wearables and garments for creating intelligent connected e-textiles.* Electronics, 2018. **7**(12): p. 405.
2. Lim, H.R., H.S. Kim, R. Qazi, Y.T. Kwon, J.W. Jeong, and W.H. Yeo, *Advanced soft materials, sensor integrations, and applications of wearable flexible hybrid electronics in healthcare, energy, and environment.* Advanced Materials, 2020. **32**(15): p. 1901924.
3. Shi, Q., J. Sun, C. Hou, Y. Li, Q. Zhang, and H. Wang, *Advanced functional fiber and smart textile.* Advanced Fiber Materials, 2019: p. 1-29.
4. Pu, X., W. Hu, and Z.L. Wang, *Toward wearable self‐charging power systems: the integration of energy‐harvesting and storage devices.* Small, 2018. **14**(1): p. 1702817.
5. Arico, A.S., P. Bruce, B. Scrosati, J.-M. Tarascon, and W. Van Schalkwijk, *Nanostructured materials for advanced energy conversion and storage devices*, in *Materials for sustainable energy: a collection of peer-reviewed research and review articles from Nature Publishing Group*. 2011, World Scientific. p. 148-159.
6. Simon, P. and Y. Gogotsi, *Materials for electrochemical capacitors*, in *Nanoscience and technology: a collection of reviews from Nature journals*. 2010, World Scientific. p. 320-329.
7. Bankole, O.E., C. Gong, and L. Lei, *Battery recycling technologies: recycling wastelithium ion batteries with the impact on the environment in-view, J.* Environment Ecology, 2013. **4**: p. 14-28.

8. Liu, W., M.-S. Song, B. Kong, and Y. Cui, *Flexible and Stretchable Energy Storage: Recent Advances and Future Perspectives.* Advanced Materials, 2017. **29**(1): p. 1603436.

9. Dong, L., C. Xu, Y. Li, Z.-H. Huang, F. Kang, Q.-H. Yang, and X. Zhao, *Flexible electrodes and supercapacitors for wearable energy storage: a review by category.* Journal of Materials Chemistry A, 2016. **4**(13): p. 4659-4685.

10. Poonam, K. Sharma, A. Arora, and S.K. Tripathi, *Review of supercapacitors: Materials and devices.* Journal of Energy Storage, 2019. **21**: p. 801-825.

11. Muzaffar, A., M.B. Ahamed, K. Deshmukh, and J. Thirumalai, *A review on recent advances in hybrid supercapacitors: Design, fabrication and applications.* Renewable and Sustainable Energy Reviews, 2019. **101**: p. 123-145.

12. Pan, S., J. Ren, X. Fang, and H. Peng, *Integration: An Effective Strategy to Develop Multifunctional Energy Storage Devices.* Advanced Energy Materials, 2016. **6**(4): p. 1501867.

13. Whittingham, M.S., *Ultimate limits to intercalation reactions for lithium batteries.* Chemical reviews, 2014. **114**(23): p. 11414-11443.

14. Lee, T.D. and A.U. Ebong, *A review of thin film solar cell technologies and challenges.* Renewable and Sustainable Energy Reviews, 2017. **70**: p. 1286-1297.

15. Siddique, A.R.M., S. Mahmud, and B. Van Heyst, *A review of the state of the science on wearable thermoelectric power generators (TEGs) and their existing challenges.* Renewable and Sustainable Energy Reviews, 2017. **73**: p. 730-744.

16. Fan, F.-R., Z.-Q. Tian, and Z.L. Wang, *Flexible triboelectric generator.* Nano energy, 2012. **1**(2): p. 328-334.

17. Erickson, P., M. Lazarus, and G. Piggot, *Limiting fossil fuel production as the next big step in climate policy.* Nature Climate Change, 2018. **8**(12): p. 1037-1043.

18. Stoppa, M. and A. Chiolerio, *Wearable electronics and smart textiles: a critical review.* sensors, 2014. **14**(7): p. 11957-11992.

19. Xue, X., S. Wang, W. Guo, Y. Zhang, and Z.L. Wang, *Hybridizing energy conversion and storage in a mechanical-to-electrochemical process for self-charging power cell.* Nano letters, 2012. **12**(9): p. 5048-5054.

20. Zeng, W., L. Shu, Q. Li, S. Chen, F. Wang, and X.M. Tao, *Fiber-based wearable electronics: a review of materials, fabrication, devices, and applications.* Advanced materials, 2014. **26**(31): p. 5310-5336.

21. Fonash, S., *Solar cell device physics*. 2012: Elsevier.

22. J. Varma, S., K. Sambath Kumar, S. Seal, S. Rajaraman, and J. Thomas, *Fiber-type solar cells, nanogenerators, batteries, and supercapacitors for wearable applications.* Advanced Science, 2018. **5**(9): p. 1800340.

23. Cai, F., T. Chen, and H. Peng, *All carbon nanotube fiber electrode-based dye-sensitized photovoltaic wire.* Journal of Materials Chemistry, 2012. **22**(30): p. 14856-14860.

24. Bell, L.E., *Cooling, heating, generating power, and recovering waste heat with thermoelectric systems.* Science, 2008. **321**(5895): p. 1457-1461.

25. Lou, Z., L. Li, L. Wang, and G. Shen, *Recent Progress of Self-Powered Sensing Systems for Wearable Electronics.* Small, 2017. **13**(45): p. 1701791.

26. Nozariasbmarz, A., H. Collins, K. Dsouza, M.H. Polash, M. Hosseini, M. Hyland, J. Liu, A. Malhotra, F.M. Ortiz, and F. Mohaddes, *Review of wearable thermoelectric energy*

harvesting: From body temperature to electronic systems. Applied Energy, 2020. **258**: p. 114069.

27. Ylli, K., D. Hoffmann, A. Willmann, P. Becker, B. Folkmer, and Y. Manoli, *Energy harvesting from human motion: exploiting swing and shock excitations.* Smart Materials and Structures, 2015. **24**(2): p. 025029.
28. Wei, C. and X. Jing, *A comprehensive review on vibration energy harvesting: Modelling and realization.* Renewable and Sustainable Energy Reviews, 2017. **74**: p. 1-18.
29. Truitt, A. and S.N. Mahmoodi, *A review on active wind energy harvesting designs.* International Journal of Precision Engineering and Manufacturing, 2013. **14**(9): p. 1667-1675.
30. Choi, J., I. Jung, and C.-Y. Kang, *A brief review of sound energy harvesting.* Nano energy, 2019. **56**: p. 169-183.
31. Wang, Z.L., T. Jiang, and L. Xu, *Toward the blue energy dream by triboelectric nanogenerator networks.* Nano Energy, 2017. **39**: p. 9-23.
32. Beeby, S.P., R. Torah, M. Tudor, P. Glynne-Jones, T. O'donnell, C. Saha, and S. Roy, *A micro electromagnetic generator for vibration energy harvesting.* Journal of Micromechanics and microengineering, 2007. **17**(7): p. 1257.
33. Wang, X., *Piezoelectric nanogenerators—Harvesting ambient mechanical energy at the nanometer scale.* Nano Energy, 2012. **1**(1): p. 13-24.
34. Wang, Z.L., L. Lin, J. Chen, S. Niu, and Y. Zi, *Triboelectric nanogenerators*. 2016: Springer.
35. Wang, Z.L., *On Maxwell's displacement current for energy and sensors: the origin of nanogenerators.* Materials Today, 2017. **20**(2): p. 74-82.

36. Fan, F.-R., W. Tang, Y. Yao, J. Luo, C. Zhang, and Z.L. Wang, *Complementary power output characteristics of electromagnetic generators and triboelectric generators.* Nanotechnology, 2014. **25**(13): p. 135402.

37. Huang, T., C. Wang, H. Yu, H. Wang, Q. Zhang, and M. Zhu, *Human walking-driven wearable all-fiber triboelectric nanogenerator containing electrospun polyvinylidene fluoride piezoelectric nanofibers.* Nano Energy, 2015. **14**: p. 226-235.

38. Zi, Y. and Z.L. Wang, *Nanogenerators: An emerging technology towards nanoenergy.* APL Materials, 2017. **5**(7): p. 074103.

39. Dong, K., X. Peng, and Z.L. Wang, *Fiber/fabric-based piezoelectric and triboelectric nanogenerators for flexible/stretchable and wearable electronics and artificial intelligence.* Advanced Materials, 2020. **32**(5): p. 1902549.

40. Wu, C., A.C. Wang, W. Ding, H. Guo, and Z.L. Wang, *Triboelectric nanogenerator: a foundation of the energy for the new era.* Advanced Energy Materials, 2019. **9**(1): p. 1802906.

41. Wang, Z.L., *Nanogenerators, self-powered systems, blue energy, piezotronics and piezo-phototronics–a recall on the original thoughts for coining these fields.* Nano Energy, 2018. **54**: p. 477-483.

42. Hu, W., C. Zhang, and Z.L. Wang, *Recent progress in piezotronics and tribotronics.* Nanotechnology, 2018. **30**(4): p. 042001.

43. Gordon, D.H., *Triboelectric interference in the ECG.* IEEE Transactions on Biomedical Engineering, 1975(3): p. 252-255.

44. Wang, Z.L., *Triboelectric nanogenerators as new energy technology and self-powered sensors–Principles, problems and perspectives.* Faraday discussions, 2015. **176**: p. 447-458.

45. Donovan, J.E., *Triboelectric noise generation in some cables commonly used with underwater electroacoustic transducers.* The Journal of the Acoustical Society of America, 1970. **48**(3B): p. 714-724.

46. Zhu, G., Z.-H. Lin, Q. Jing, P. Bai, C. Pan, Y. Yang, Y. Zhou, and Z.L. Wang, *Toward large-scale energy harvesting by a nanoparticle-enhanced triboelectric nanogenerator.* Nano letters, 2013. **13**(2): p. 847-853.

47. Quan, T., Y. Wu, and Y. Yang, *Hybrid electromagnetic–triboelectric nanogenerator for harvesting vibration energy.* Nano Research, 2015. **8**(10): p. 3272-3280.

48. Lee, S., W. Ko, Y. Oh, J. Lee, G. Baek, Y. Lee, J. Sohn, S. Cha, J. Kim, and J. Park, *Triboelectric energy harvester based on wearable textile platforms employing various surface morphologies.* Nano Energy, 2015. **12**: p. 410-418.

49. Tang, W., T. Jiang, F.R. Fan, A.F. Yu, C. Zhang, X. Cao, and Z.L. Wang, *Liquid-metal electrode for high-performance triboelectric nanogenerator at an instantaneous energy conversion efficiency of 70.6%.* Advanced Functional Materials, 2015. **25**(24): p. 3718-3725.

50. Cui, N., L. Gu, J. Liu, S. Bai, J. Qiu, J. Fu, X. Kou, H. Liu, Y. Qin, and Z.L. Wang, *High performance sound driven triboelectric nanogenerator for harvesting noise energy.* Nano Energy, 2015. **15**: p. 321-328.

51. Chen, S., C. Gao, W. Tang, H. Zhu, Y. Han, Q. Jiang, T. Li, X. Cao, and Z. Wang, *Self-powered cleaning of air pollution by wind driven triboelectric nanogenerator.* Nano Energy, 2015. **14**: p. 217-225.

52. Mao, Y., D. Geng, E. Liang, and X. Wang, *Single-electrode triboelectric nanogenerator for scavenging friction energy from rolling tires.* Nano Energy, 2015. **15**: p. 227-234.

53. Su, Y., X. Wen, G. Zhu, J. Yang, J. Chen, P. Bai, Z. Wu, Y. Jiang, and Z.L. Wang, *Hybrid triboelectric nanogenerator for harvesting water wave energy and as a self-powered distress signal emitter.* Nano Energy, 2014. **9**: p. 186-195.

54. Wang, S., L. Lin, and Z.L. Wang, *Triboelectric nanogenerators as self-powered active sensors.* Nano Energy, 2015. **11**: p. 436-462.

55. Zhang, N., C. Tao, X. Fan, and J. Chen, *Progress in triboelectric nanogenerators as self-powered smart sensors.* Journal of Materials Research, 2017. **32**(9): p. 1628-1646.

56. Feng, Z., S. Yang, S. Jia, Y. Zhang, S. Jiang, L. Yu, R. Li, G. Song, A. Wang, and T. Martin, *Scalable, washable and lightweight triboelectric-energy-generating fibers by the thermal drawing process for industrial loom weaving.* Nano Energy, 2020: p. 104805.

57. Lin, Z., J. Yang, X. Li, Y. Wu, W. Wei, J. Liu, J. Chen, and J. Yang, *Large-scale and washable smart textiles based on triboelectric nanogenerator arrays for self-powered sleeping monitoring.* Advanced Functional Materials, 2018. **28**(1): p. 1704112.

58. Dong, K., J. Deng, Y. Zi, Y.C. Wang, C. Xu, H. Zou, W. Ding, Y. Dai, B. Gu, and B. Sun, *3D orthogonal woven triboelectric nanogenerator for effective biomechanical energy harvesting and as self-powered active motion sensors.* Advanced Materials, 2017. **29**(38): p. 1702648.

59. Han, M., X. Zhang, and H. Zhang, *Flexible and Stretchable Triboelectric Nanogenerator Devices: Toward Self-powered Systems*. 2019: John Wiley & Sons.

60. Zhou, T., C. Zhang, C.B. Han, F.R. Fan, W. Tang, and Z.L. Wang, *Woven structured triboelectric nanogenerator for wearable devices.* ACS applied materials & interfaces, 2014. **6**(16): p. 14695-14701.

61. Kwak, S.S., H. Kim, W. Seung, J. Kim, R. Hinchet, and S.-W. Kim, *Fully stretchable textile triboelectric nanogenerator with knitted fabric structures.* ACS nano, 2017. **11**(11): p. 10733-10741.

62. Dong, K., J. Zhang, L. Jin, B. Gu, and B. Sun, *Multi-scale finite element analyses on the thermal conductive behaviors of 3D braided composites.* Composite Structures, 2016. **143**: p. 9-22.

63. Tong, Y., Z. Feng, J. Kim, J.L. Robertson, X. Jia, and B.N. Johnson, *3D printed stretchable triboelectric nanogenerator fibers and devices.* Nano Energy, 2020: p. 104973.

64. Yin, X., D. Liu, L. Zhou, X. Li, C. Zhang, P. Cheng, H. Guo, W. Song, J. Wang, and Z.L. Wang, *Structure and dimension effects on the performance of layered triboelectric nanogenerators in contact-separation mode.* ACS nano, 2018. **13**(1): p. 698-705.

65. Wang, Q., M. Chen, W. Li, Z. Li, Y. Chen, and Y. Zhai, *Size effect on the output of a miniaturized triboelectric nanogenerator based on superimposed electrode layers.* Nano energy, 2017. **41**: p. 128-138.

66. Zi, Y., C. Wu, W. Ding, and Z.L. Wang, *Maximized Effective Energy Output of Contact-Separation-Triggered Triboelectric Nanogenerators as Limited by Air Breakdown.* Advanced Functional Materials, 2017. **27**(24): p. 1700049.

67. Zhang, H., C. Zhang, J. Zhang, L. Quan, H. Huang, J. Jiang, S. Dong, and J. Luo, *A theoretical approach for optimizing sliding-mode triboelectric nanogenerator based on multi-parameter analysis.* Nano Energy, 2019. **61**: p. 442-453.

68. Jing, Q., G. Zhu, P. Bai, Y. Xie, J. Chen, R.P. Han, and Z.L. Wang, *Case-encapsulated triboelectric nanogenerator for harvesting energy from reciprocating sliding motion.* ACS nano, 2014. **8**(4): p. 3836-3842.

69. Wang, S., L. Lin, Y. Xie, Q. Jing, S. Niu, and Z.L. Wang, *Sliding-triboelectric nanogenerators based on in-plane charge-separation mechanism.* Nano letters, 2013. **13**(5): p. 2226-2233.

70. Wang, M., N. Zhang, Y. Tang, H. Zhang, C. Ning, L. Tian, W. Li, J. Zhang, Y. Mao, and E. Liang, *Single-electrode triboelectric nanogenerators based on sponge-like porous PTFE thin films for mechanical energy harvesting and self-powered electronics.* Journal of Materials Chemistry A, 2017. **5**(24): p. 12252-12257.

71. Chen, S.W., X. Cao, N. Wang, L. Ma, H.R. Zhu, M. Willander, Y. Jie, and Z.L. Wang, *An ultrathin flexible single-electrode triboelectric-nanogenerator for mechanical energy harvesting and instantaneous force sensing.* Advanced Energy Materials, 2017. **7**(1): p. 1601255.

72. Zhao, Z., X. Pu, C. Du, L. Li, C. Jiang, W. Hu, and Z.L. Wang, *Freestanding flag-type triboelectric nanogenerator for harvesting high-altitude wind energy from arbitrary directions.* ACS nano, 2016. **10**(2): p. 1780-1787.

73. Guo, H., X. Jia, L. Liu, X. Cao, N. Wang, and Z.L. Wang, *Freestanding triboelectric nanogenerator enables noncontact motion-tracking and positioning.* ACS nano, 2018. **12**(4): p. 3461-3467.

74. Xie, Y., S. Wang, S. Niu, L. Lin, Q. Jing, J. Yang, Z. Wu, and Z.L. Wang, *Grating-structured freestanding triboelectric-layer nanogenerator for harvesting mechanical energy at 85% total conversion efficiency.* advanced materials, 2014. **26**(38): p. 6599-6607.

75. Niu, S., S. Wang, L. Lin, Y. Liu, Y.S. Zhou, Y. Hu, and Z.L. Wang, *Theoretical study of contact-mode triboelectric nanogenerators as an effective power source.* Energy & Environmental Science, 2013. **6**(12): p. 3576-3583.

76. Niu, S., Y. Liu, S. Wang, L. Lin, Y.S. Zhou, Y. Hu, and Z.L. Wang, *Theory of sliding-mode triboelectric nanogenerators.* Advanced materials, 2013. **25**(43): p. 6184-6193.

77. Niu, S., Y. Liu, S. Wang, L. Lin, Y.S. Zhou, Y. Hu, and Z.L. Wang, *Theoretical investigation and structural optimization of single-electrode triboelectric nanogenerators.* Advanced Functional Materials, 2014. **24**(22): p. 3332-3340.

78. Niu, S., Y. Liu, X. Chen, S. Wang, Y.S. Zhou, L. Lin, Y. Xie, and Z.L. Wang, *Theory of freestanding triboelectric-layer-based nanogenerators.* Nano Energy, 2015. **12**: p. 760-774.

79. Niu, S., Y.S. Zhou, S. Wang, Y. Liu, L. Lin, Y. Bando, and Z.L. Wang, *Simulation method for optimizing the performance of an integrated triboelectric nanogenerator energy harvesting system.* Nano Energy, 2014. **8**: p. 150-156.

80. Zhu, G., J. Chen, Y. Liu, P. Bai, Y.S. Zhou, Q. Jing, C. Pan, and Z.L. Wang, *Linear-grating triboelectric generator based on sliding electrification.* Nano letters, 2013. **13**(5): p. 2282-2289.

81. Zhou, Y.S., G. Zhu, S. Niu, Y. Liu, P. Bai, Q. Jing, and Z.L. Wang, *Nanometer resolution self-powered static and dynamic motion sensor based on micro-grated triboelectrification.* Advanced Materials, 2014. **26**(11): p. 1719-1724.

82. Zhu, G., Y.S. Zhou, P. Bai, X.S. Meng, Q. Jing, J. Chen, and Z.L. Wang, *A shape-adaptive thin-film-based approach for 50% high-efficiency energy generation through micro-grating sliding electrification.* Advanced materials, 2014. **26**(23): p. 3788-3796.

83. Jackson, J.D., *Classical electrodynamics*. 2007: John Wiley & Sons.

84. Dong, K., J. Deng, W. Ding, A.C. Wang, P. Wang, C. Cheng, Y.C. Wang, L. Jin, B. Gu, and B. Sun, *Versatile core–sheath yarn for sustainable biomechanical energy harvesting and real-time human-interactive sensing.* Advanced Energy Materials, 2018. **8**(23): p. 1801114.

85. Niu, S., S. Wang, Y. Liu, Y.S. Zhou, L. Lin, Y. Hu, K.C. Pradel, and Z.L. Wang, *A theoretical study of grating structured triboelectric nanogenerators.* Energy & Environmental Science, 2014. **7**(7): p. 2339-2349.

86. Zi, Y., S. Niu, J. Wang, Z. Wen, W. Tang, and Z.L. Wang, *Standards and figure-of-merits for quantifying the performance of triboelectric nanogenerators.* Nature communications, 2015. **6**(1): p. 1-8.

87. Zou, H., Y. Zhang, L. Guo, P. Wang, X. He, G. Dai, H. Zheng, C. Chen, A.C. Wang, and C. Xu, *Quantifying the triboelectric series.* Nature communications, 2019. **10**(1): p. 1-9.

88. Zhu, G., C. Pan, W. Guo, C.-Y. Chen, Y. Zhou, R. Yu, and Z.L. Wang, *Triboelectric-generator-driven pulse electrodeposition for micropatterning.* Nano letters, 2012. **12**(9): p. 4960-4965.

89. Chen, J., G. Zhu, W. Yang, Q. Jing, P. Bai, Y. Yang, T.C. Hou, and Z.L. Wang, *Harmonic-resonator-based triboelectric nanogenerator as a sustainable power source and a self-powered active vibration sensor.* Advanced materials, 2013. **25**(42): p. 6094-6099.

90. Khandelwal, G., A. Chandrasekhar, N.R. Alluri, V. Vivekananthan, N.P.M.J. Raj, and S.-J. Kim, *Trash to energy: A facile, robust and cheap approach for mitigating environment pollutant using household triboelectric nanogenerator.* Applied Energy, 2018. **219**: p. 338-349.

91. Chun, J., J.W. Kim, W.-s. Jung, C.-Y. Kang, S.-W. Kim, Z.L. Wang, and J.M. Baik, *Mesoporous pores impregnated with Au nanoparticles as effective dielectrics for enhancing triboelectric nanogenerator performance in harsh environments.* Energy & Environmental Science, 2015. **8**(10): p. 3006-3012.

92. Bai, P., G. Zhu, Z.-H. Lin, Q. Jing, J. Chen, G. Zhang, J. Ma, and Z.L. Wang, *Integrated multilayered triboelectric nanogenerator for harvesting biomechanical energy from human motions.* ACS nano, 2013. **7**(4): p. 3713-3719.

93. Yang, Y., H. Zhang, J. Chen, Q. Jing, Y.S. Zhou, X. Wen, and Z.L. Wang, *Single-electrode-based sliding triboelectric nanogenerator for self-powered displacement vector sensor system.* Acs Nano, 2013. **7**(8): p. 7342-7351.

94. Du, W., X. Han, L. Lin, M. Chen, X. Li, C. Pan, and Z.L. Wang, *A Three Dimensional Multi-Layered Sliding Triboelectric Nanogenerator.* Advanced Energy Materials, 2014. **4**(11): p. 1301592.

95. Lin, L., S. Wang, Y. Xie, Q. Jing, S. Niu, Y. Hu, and Z.L. Wang, *Segmentally structured disk triboelectric nanogenerator for harvesting rotational mechanical energy.* Nano letters, 2013. **13**(6): p. 2916-2923.

96. Bai, P., G. Zhu, Y. Liu, J. Chen, Q. Jing, W. Yang, J. Ma, G. Zhang, and Z.L. Wang, *Cylindrical rotating triboelectric nanogenerator.* ACS nano, 2013. **7**(7): p. 6361-6366.

97. Yang, P.-K., Z.-H. Lin, K.C. Pradel, L. Lin, X. Li, X. Wen, J.-H. He, and Z.L. Wang, *based origami triboelectric nanogenerators and self-powered pressure sensors.* ACS nano, 2015. **9**(1): p. 901-907.

98. Yang, Y., Y.S. Zhou, H. Zhang, Y. Liu, S. Lee, and Z.L. Wang, *A single-electrode based triboelectric nanogenerator as self-powered tracking system.* Advanced Materials, 2013. **25**(45): p. 6594-6601.

99. Zhang, H., Y. Yang, Y. Su, J. Chen, K. Adams, S. Lee, C. Hu, and Z.L. Wang, *Triboelectric nanogenerator for harvesting vibration energy in full space and as self-powered acceleration sensor.* Advanced Functional Materials, 2014. **24**(10): p. 1401-1407.

100. Meng, B., W. Tang, Z.-h. Too, X. Zhang, M. Han, W. Liu, and H. Zhang, *A transparent single-friction-surface triboelectric generator and self-powered touch sensor.* Energy & Environmental Science, 2013. **6**(11): p. 3235-3240.

101. Bai, P., G. Zhu, Q. Jing, J. Yang, J. Chen, Y. Su, J. Ma, G. Zhang, and Z.L. Wang, *Membrane-based self-powered triboelectric sensors for pressure change detection and its uses in security surveillance and healthcare monitoring.* Advanced Functional Materials, 2014. **24**(37): p. 5807-5813.

102. Wu, Y., Q. Jing, J. Chen, P. Bai, J. Bai, G. Zhu, Y. Su, and Z.L. Wang, *A self-powered angle measurement sensor based on triboelectric nanogenerator.* Advanced Functional Materials, 2015. **25**(14): p. 2166-2174.

103. Cui, C., X. Wang, Z. Yi, B. Yang, X. Wang, X. Chen, J. Liu, and C. Yang, *Flexible single-electrode triboelectric nanogenerator and body moving sensor based on porous Na2CO3/polydimethylsiloxane film.* ACS applied materials & interfaces, 2018. **10**(4): p. 3652-3659.

104. Shi, Q. and C. Lee, *Self-powered bio-inspired spider-net-coding interface using single-electrode triboelectric nanogenerator.* Advanced Science, 2019. **6**(15): p. 1900617.

105. Mule, A.R., B. Dudem, H. Patnam, S.A. Graham, and J.S. Yu, *Wearable Single-Electrode-Mode Triboelectric Nanogenerator via Conductive Polymer-Coated Textiles for Self-Power Electronics.* ACS Sustainable Chemistry & Engineering, 2019. **7**(19): p. 16450-16458.

106. Ning, C., L. Tian, X. Zhao, S. Xiang, Y. Tang, E. Liang, and Y. Mao, *Washable textile-structured single-electrode triboelectric nanogenerator for self-powered wearable electronics.* Journal of Materials Chemistry A, 2018. **6**(39): p. 19143-19150.

107. Guo, H., T. Li, X. Cao, J. Xiong, Y. Jie, M. Willander, X. Cao, N. Wang, and Z.L. Wang, *Self-sterilized flexible single-electrode triboelectric nanogenerator for energy harvesting and dynamic force sensing.* ACS nano, 2017. **11**(1): p. 856-864.

108. Wang, S., Y. Xie, S. Niu, L. Lin, and Z.L. Wang, *Freestanding triboelectric-layer-based nanogenerators for harvesting energy from a moving object or human motion in contact and non-contact modes.* Advanced materials, 2014. **26**(18): p. 2818-2824.

109. Wang, S., S. Niu, J. Yang, L. Lin, and Z.L. Wang, *Quantitative measurements of vibration amplitude using a contact-mode freestanding triboelectric nanogenerator.* ACS nano, 2014. **8**(12): p. 12004-12013.

110. Wang, J., W. Ding, L. Pan, C. Wu, H. Yu, L. Yang, R. Liao, and Z.L. Wang, *Self-powered wind sensor system for detecting wind speed and direction based on a triboelectric nanogenerator.* ACS nano, 2018. **12**(4): p. 3954-3963.

111. Phan, H., D.-M. Shin, S.H. Jeon, T.Y. Kang, P. Han, G.H. Kim, H.K. Kim, K. Kim, Y.-H. Hwang, and S.W. Hong, *Aerodynamic and aeroelastic flutters driven triboelectric nanogenerators for harvesting broadband airflow energy.* Nano Energy, 2017. **33**: p. 476-484.

112. Lin, L., Y. Xie, S. Niu, S. Wang, P.-K. Yang, and Z.L. Wang, *Robust triboelectric nanogenerator based on rolling electrification and electrostatic induction at an instantaneous energy conversion efficiency of ~ 55%.* ACS nano, 2015. **9**(1): p. 922-930.

113. Lin, L., S. Wang, S. Niu, C. Liu, Y. Xie, and Z.L. Wang, *Noncontact free-rotating disk triboelectric nanogenerator as a sustainable energy harvester and self-powered mechanical sensor.* ACS applied materials & interfaces, 2014. **6**(4): p. 3031-3038.

114. Yeh, M.H., H. Guo, L. Lin, Z. Wen, Z. Li, C. Hu, and Z.L. Wang, *Rolling friction enhanced free-standing triboelectric nanogenerators and their applications in self-powered electrochemical recovery systems.* Advanced Functional Materials, 2016. **26**(7): p. 1054-1062.

115. Qian, J., J. He, S. Qian, J. Zhang, X. Niu, X. Fan, C. Wang, X. Hou, J. Mu, and W. Geng, *A nonmetallic stretchable nylon-modified high performance triboelectric nanogenerator for energy harvesting.* Advanced Functional Materials, 2020. **30**(4): p. 1907414.

116. Lei, R., Y. Shi, Y. Ding, J. Nie, S. Li, F. Wang, H. Zhai, X. Chen, and Z. Wang, *Sustainable High Voltage Source based on Triboelectric Nanogenerator with Charge Accumulation Strategy.* Energy & Environmental Science, 2020.

117. Tao, J., R. Bao, X. Wang, Y. Peng, J. Li, S. Fu, C. Pan, and Z.L. Wang, *Self-powered tactile sensor array systems based on the triboelectric effect.* Advanced Functional Materials, 2018: p. 1806379.

118. Han, S.-T., H. Peng, Q. Sun, S. Venkatesh, K.-S. Chung, S.C. Lau, Y. Zhou, and V.A.L. Roy, *An Overview of the Development of Flexible Sensors.* Advanced Materials, 2017. **29**(33): p. 1700375.

119. Lin, M., N.-G. Gutierrez, and S. Xu, *Soft sensors form a network.* Nature Electronics, 2019. **2**(8): p. 327-328.

120. Shi, J., S. Liu, L. Zhang, B. Yang, L. Shu, Y. Yang, M. Ren, Y. Wang, J. Chen, W. Chen, Y. Chai, and X. Tao, *Smart Textile-Integrated Microelectronic Systems for Wearable Applications.* Advanced Materials. **n/a**(n/a): p. 1901958.

121. Khan, S.M., A. Gumus, J.M. Nassar, and M.M. Hussain, *CMOS Enabled Microfluidic Systems for Healthcare Based Applications.* Advanced Materials, 2018. **30**(16): p. 1705759.

122. Khan, Y., M. Garg, Q. Gui, M. Schadt, A. Gaikwad, D. Han, N.A.D. Yamamoto, P. Hart, R. Welte, W. Wilson, S. Czarnecki, M. Poliks, Z. Jin, K. Ghose, F. Egitto, J. Turner, and A.C. Arias, *Flexible Hybrid Electronics: Direct Interfacing of Soft and Hard Electronics for Wearable Health Monitoring.* Advanced Functional Materials, 2016. **26**(47): p. 8764-8775.

123. Kelly, K., *Out of control: The new biology of machines, social systems, and the economic world*. 2009: Hachette UK.

124. Minoli, D. and B. Occhiogrosso, *Internet of Things Applications for Smart Cities.* Internet of Things A to Z: Technologies and Applications, 2018: p. 319.

125. Ramalho, J.F.C.B., S.F.H. Correia, L. Fu, L.L.F. António, C.D.S. Brites, P.S. André, R.A.S. Ferreira, and L.D. Carlos, *Luminescence Thermometry on the Route of the Mobile-Based Internet of Things (IoT): How Smart QR Codes Make It Real.* Advanced Science, 2019. **6**(19): p. 1900950.

126. Ahmed, A., I. Hassan, M.F. El-Kady, A. Radhi, C.K. Jeong, P.R. Selvaganapathy, J. Zu, S. Ren, Q. Wang, and R.B. Kaner, *Integrated Triboelectric Nanogenerators in the Era of the Internet of Things.* Advanced Science. **n/a**(n/a): p. 1802230.

127. Xia, F., L.T. Yang, L. Wang, and A. Vinel, *Internet of Things.* International Journal of Communication Systems, 2012. **25**(9): p. 1101-1102.

128. Coetzee, L. and J. Eksteen, *Internet of things–promise for the future? An Introduction.* 2011.

129. Uckelmann, D., M. Harrison, and F. Michahelles, *Architecting the internet of things*. 2011: Springer Science & Business Media.

130. Gilchrist, A., *Industry 4.0: the industrial internet of things*. 2016: Apress.

131. Piyare, R., *Internet of things: ubiquitous home control and monitoring system using android based smart phone.* International journal of Internet of Things, 2013. **2**(1): p. 5-11.

132. Denton, J.A., *Society and the official world: a reintroduction to sociology*. 1990: Rowman & Littlefield.

133. Park, S. and S. Jayaraman, *Smart textiles: Wearable electronic systems.* MRS bulletin, 2003. **28**(8): p. 585-591.

134. Lee, H.J., Z.X. Jin, A.N. Aleshin, J.Y. Lee, M.J. Goh, K. Akagi, Y.S. Kim, D.W. Kim, and Y.W. Park, *Dispersion and Current− Voltage Characteristics of Helical Polyacetylene Single Fibers.* Journal of the American Chemical Society, 2004. **126**(51): p. 16722-16723.

135. Huang, J., S. Virji, B.H. Weiller, and R.B. Kaner, *Polyaniline nanofibers: facile synthesis and chemical sensors.* Journal of the American Chemical Society, 2003. **125**(2): p. 314-315.

136. Kang, T.S., S.W. Lee, J. Joo, and J.Y. Lee, *Electrically conducting polypyrrole fibers spun by electrospinning.* Synthetic Metals, 2005. **153**(1-3): p. 61-64.

137. Li, X., C. Li, J. Chen, C. Li, and C. Sun, *Polythiophene as a novel fiber coating for solid-phase microextraction.* Journal of Chromatography A, 2008. **1198**: p. 7-13.

138. Baik, W., W. Luan, R.H. Zhao, S. Koo, and K.-S. Kim, *Synthesis of highly conductive poly (3, 4-ethylenedioxythiophene) fiber by simple chemical polymerization.* Synthetic metals, 2009. **159**(13): p. 1244-1246.

139. Chen, Y., B. Zhang, G. Liu, X. Zhuang, and E.-T. Kang, *Graphene and its derivatives: switching ON and OFF.* Chemical Society Reviews, 2012. **41**(13): p. 4688-4707.

140. Wen, L., F. Li, and H.M. Cheng, *Carbon nanotubes and graphene for flexible electrochemical energy storage: from materials to devices.* Advanced Materials, 2016. **28**(22): p. 4306-4337.

141. Du, J., S. Pei, L. Ma, and H.M. Cheng, *25th anniversary article: carbon nanotube-and graphene-based transparent conductive films for optoelectronic devices.* Advanced materials, 2014. **26**(13): p. 1958-1991.

142. Yang, Y., N. Sun, Z. Wen, P. Cheng, H. Zheng, H. Shao, Y. Xia, C. Chen, H. Lan, and X. Xie, *Liquid-metal-based super-stretchable and structure-designable triboelectric nanogenerator for wearable electronics.* Acs Nano, 2018. **12**(2): p. 2027-2034.

143. Bo, G., L. Ren, X. Xu, Y. Du, and S. Dou, *Recent progress on liquid metals and their applications.* Advances in Physics: X, 2018. **3**(1): p. 1446359.

144. Zhao, S., J. Li, D. Cao, G. Zhang, J. Li, K. Li, Y. Yang, W. Wang, Y. Jin, and R. Sun, *Recent advancements in flexible and stretchable electrodes for electromechanical sensors: strategies, materials, and features.* ACS applied materials & interfaces, 2017. **9**(14): p. 12147-12164.

145. Sun, J., Y. Huang, C. Fu, Z. Wang, Y. Huang, M. Zhu, C. Zhi, and H. Hu, *High-performance stretchable yarn supercapacitor based on PPy@ CNTs@ urethane elastic fiber core spun yarn.* Nano Energy, 2016. **27**: p. 230-237.

146. Tokuno, T., M. Nogi, J. Jiu, and K. Suganuma, *Hybrid transparent electrodes of silver nanowires and carbon nanotubes: a low-temperature solution process.* Nanoscale research letters, 2012. **7**(1): p. 281.

147. Liu, Z., K. Parvez, R. Li, R. Dong, X. Feng, and K. Müllen, *Transparent conductive electrodes from graphene/PEDOT: PSS hybrid inks for ultrathin organic photodetectors.* Advanced Materials, 2015. **27**(4): p. 669-675.

148. Lu, Z., J. Foroughi, C. Wang, H. Long, and G.G. Wallace, *Superelastic hybrid CNT/graphene fibers for wearable energy storage.* Advanced Energy Materials, 2018. **8**(8): p. 1702047.

149. Paosangthong, W., R. Torah, and S. Beeby, *Recent progress on textile-based triboelectric nanogenerators.* Nano Energy, 2019. **55**: p. 401-423.

150. Lai, Y.C., J. Deng, S.L. Zhang, S. Niu, H. Guo, and Z.L. Wang, *Single-thread-based wearable and highly stretchable triboelectric nanogenerators and their applications in cloth-based self-powered human-interactive and biomedical sensing.* Advanced Functional Materials, 2017. **27**(1): p. 1604462.

151. Dong, K., Y.-C. Wang, J. Deng, Y. Dai, S.L. Zhang, H. Zou, B. Gu, B. Sun, and Z.L. Wang, *A highly stretchable and washable all-yarn-based self-charging knitting power textile composed of fiber triboelectric nanogenerators and supercapacitors.* Acs Nano, 2017. **11**(9): p. 9490-9499.

152. Yu, A., X. Pu, R. Wen, M. Liu, T. Zhou, K. Zhang, Y. Zhang, J. Zhai, W. Hu, and Z.L. Wang, *Core–shell-yarn-based triboelectric nanogenerator textiles as power cloths.* ACS nano, 2017. **11**(12): p. 12764-12771.

153. Wang, W., A. Yu, X. Liu, Y. Liu, Y. Zhang, Y. Zhu, Y. Lei, M. Jia, J. Zhai, and Z.L. Wang, *Large-scale fabrication of robust textile triboelectric nanogenerators.* Nano Energy, 2020. **71**: p. 104605.

154. Dong, K., X. Peng, J. An, A.C. Wang, J. Luo, B. Sun, J. Wang, and Z.L. Wang, *Shape adaptable and highly resilient 3D braided triboelectric nanogenerators as e-textiles for power and sensing.* Nature Communications, 2020. **11**(1): p. 1-11.

155. Park, J., A.Y. Choi, C.J. Lee, D. Kim, and Y.T. Kim, *Highly stretchable fiber-based single-electrode triboelectric nanogenerator for wearable devices.* RSC advances, 2017. **7**(86): p. 54829-54834.

156. Xie, L., X. Chen, Z. Wen, Y. Yang, J. Shi, C. Chen, M. Peng, Y. Liu, and X. Sun, *Spiral steel wire based fiber-shaped stretchable and tailorable triboelectric nanogenerator for wearable power source and active gesture sensor.* Nano-Micro Letters, 2019. **11**(1): p. 39.

157. Abouraddy, A., M. Bayindir, G. Benoit, S. Hart, K. Kuriki, N. Orf, O. Shapira, F. Sorin, B. Temelkuran, and Y. Fink, *Towards multimaterial multifunctional fibres that see, hear, sense and communicate.* Nature materials, 2007. **6**(5): p. 336-347.

158. Yan, W., A. Page, T. Nguyen-Dang, Y. Qu, F. Sordo, L. Wei, and F. Sorin, *Advanced Multimaterial Electronic and Optoelectronic Fibers and Textiles.* Advanced Materials, 2019. **31**(1): p. 1802348.

159. Yaman, M., T. Khudiyev, E. Ozgur, M. Kanik, O. Aktas, E.O. Ozgur, H. Deniz, E. Korkut, and M. Bayindir, *Arrays of indefinitely long uniform nanowires and nanotubes.* Nature materials, 2011. **10**(7): p. 494-501.

160. Yan, W., C. Dong, Y. Xiang, S. Jiang, A. Leber, G. Loke, W. Xu, C. Hou, S. Zhou, and M. Chen, *Thermally drawn advanced functional fibers: New frontier of flexible electronics.* Materials Today, 2020.

161. Rein, M., V.D. Favrod, C. Hou, T. Khudiyev, A. Stolyarov, J. Cox, C.-C. Chung, C. Chhav, M. Ellis, and J. Joannopoulos, *Diode fibres for fabric-based optical communications.* Nature, 2018. **560**(7717): p. 214-218.

162. Yu, L., S. Parker, H. Xuan, Y. Zhang, S. Jiang, M. Tousi, M. Manteghi, A. Wang, and X. Jia, *Flexible Multi-Material Fibers for Distributed Pressure and Temperature Sensing.* Advanced Functional Materials, 2020. **30**(9): p. 1908915.

163. Lestoquoy, G., N. Chocat, Z. Wang, J.D. Joannopoulos, and Y. Fink, *Fabrication and characterization of thermally drawn fiber capacitors.* Applied Physics Letters, 2013. **102**(15): p. 152908.

164. Kanik, M., S. Orguc, G. Varnavides, J. Kim, T. Benavides, D. Gonzalez, T. Akintilo, C.C. Tasan, A.P. Chandrakasan, and Y. Fink, *Strain-programmable fiber-based artificial muscle.* Science, 2019. **365**(6449): p. 145-150.

165. Loke, G., W. Yan, T. Khudiyev, G. Noel, and Y. Fink, *Recent progress and perspectives of thermally drawn multimaterial fiber electronics.* Advanced Materials, 2020. **32**(1): p. 1904911.

166. Younes, R., M. Jones, and T.L. Martin, *Classifier for activities with variations.* Sensors, 2018. **18**(10): p. 3529.

167. Blake, M., R. Younes, J. Dennis, T.L. Martin, and M. Jones, *A user-independent and sensor-tolerant wearable activity classifier.* Computer, 2015. **48**(10): p. 64-71.

168. Li, Z., M. Zhu, J. Shen, Q. Qiu, J. Yu, and B. Ding, *All-fiber structured electronic skin with high elasticity and breathability.* Advanced Functional Materials, 2020. **30**(6): p. 1908411.

169. Zhu, M., M. Lou, I. Abdalla, J. Yu, Z. Li, and B. Ding, *Highly shape adaptive fiber based electronic skin for sensitive joint motion monitoring and tactile sensing.* Nano Energy, 2020. **69**: p. 104429.

170. Lou, M., I. Abdalla, M. Zhu, J. Yu, Z. Li, and B. Ding, *Hierarchically rough structured and self-powered pressure sensor textile for motion sensing and pulse monitoring.* ACS Applied Materials & Interfaces, 2019. **12**(1): p. 1597-1605.

171. Chu, H., H. Jang, Y. Lee, Y. Chae, and J.-H. Ahn, *Conformal, graphene-based triboelectric nanogenerator for self-powered wearable electronics.* Nano Energy, 2016. **27**: p. 298-305.

172. Yi, F., X. Wang, S. Niu, S. Li, Y. Yin, K. Dai, G. Zhang, L. Lin, Z. Wen, and H. Guo, *A highly shape-adaptive, stretchable design based on conductive liquid for energy harvesting and self-powered biomechanical monitoring.* Science advances, 2016. **2**(6): p. e1501624.

173. Zheng, Q., Y. Zou, Y. Zhang, Z. Liu, B. Shi, X. Wang, Y. Jin, H. Ouyang, Z. Li, and Z.L. Wang, *Biodegradable triboelectric nanogenerator as a life-time designed implantable power source.* Science advances, 2016. **2**(3): p. e1501478.

174. Pu, X., M. Liu, X. Chen, J. Sun, C. Du, Y. Zhang, J. Zhai, W. Hu, and Z.L. Wang, *Ultrastretchable, transparent triboelectric nanogenerator as electronic skin for biomechanical energy harvesting and tactile sensing.* Science advances, 2017. **3**(5): p. e1700015.

175. Liu, R., X. Kuang, J. Deng, Y.C. Wang, A.C. Wang, W. Ding, Y.C. Lai, J. Chen, P. Wang, and Z. Lin, *Shape memory polymers for body motion energy harvesting and self‐powered mechanosensing.* Advanced Materials, 2018. **30**(8): p. 1705195.

176. Deng, J., X. Kuang, R. Liu, W. Ding, A.C. Wang, Y.C. Lai, K. Dong, Z. Wen, Y. Wang, and L. Wang, *Vitrimer elastomer‐based jigsaw puzzle‐like healable triboelectric*

nanogenerator for self‐powered wearable electronics. Advanced Materials, 2018. **30**(14): p. 1705918.

177. Yu, J., X. Hou, M. Cui, S. Zhang, J. He, W. Geng, J. Mu, and X. Chou, *Highly skin-conformal wearable tactile sensor based on piezoelectric-enhanced triboelectric nanogenerator.* Nano Energy, 2019. **64**: p. 103923.

178. Lan, L., T. Yin, C. Jiang, X. Li, Y. Yao, Z. Wang, S. Qu, Z. Ye, J. Ping, and Y. Ying, *Highly conductive 1D-2D composite film for skin-mountable strain sensor and stretchable triboelectric nanogenerator.* Nano Energy, 2019. **62**: p. 319-328.

179. Xiong, W., K. Hu, Z. Li, Y. Jiang, Z. Li, Z. Li, and X. Wang, *A wearable system based on core-shell structured peptide-Co9S8 supercapacitor and triboelectric nanogenerator.* Nano Energy, 2019. **66**: p. 104149.

180. Park, C., M. Koo, G. Song, S.M. Cho, H.S. Kang, T.H. Park, E.H. Kim, and C. Park, *Surface-Conformal Triboelectric Nanopores via Supramolecular Ternary Polymer Assembly.* ACS nano, 2020. **14**(1): p. 755-766.

181. Yu, J., X. Hou, J. He, M. Cui, C. Wang, W. Geng, J. Mu, B. Han, and X. Chou, *Ultra-flexible and high-sensitive triboelectric nanogenerator as electronic skin for self-powered human physiological signal monitoring.* Nano Energy, 2020. **69**: p. 104437.

182. Lopes, A.J., E. MacDonald, and R.B. Wicker, *Integrating stereolithography and direct print technologies for 3D structural electronics fabrication.* Rapid Prototyping Journal, 2012.

183. Macdonald, E., R. Salas, D. Espalin, M. Perez, E. Aguilera, D. Muse, and R.B. Wicker, *3D printing for the rapid prototyping of structural electronics.* IEEE access, 2014. **2**: p. 234-242.

184. Espalin, D., D.W. Muse, E. MacDonald, and R.B. Wicker, *3D Printing multifunctionality: structures with electronics.* The International Journal of Advanced Manufacturing Technology, 2014. **72**(5-8): p. 963-978.

185. Chen, B., W. Tang, T. Jiang, L. Zhu, X. Chen, C. He, L. Xu, H. Guo, P. Lin, and D. Li, *Three-dimensional ultraflexible triboelectric nanogenerator made by 3D printing.* Nano Energy, 2018. **45**: p. 380-389.

186. Gao, S., Y. Zhu, Y. Chen, M. Tian, Y. Yang, T. Jiang, and Z.L. Wang, *Self-power electroreduction of N2 into NH3 by 3D printed triboelectric nanogenerators.* Materials Today, 2019. **28**: p. 17-24.

187. Mannoor, M.S., Z. Jiang, T. James, Y.L. Kong, K.A. Malatesta, W.O. Soboyejo, N. Verma, D.H. Gracias, and M.C. McAlpine, *3D printed bionic ears.* Nano letters, 2013. **13**(6): p. 2634-2639.

188. Kong, Y.L., M.K. Gupta, B.N. Johnson, and M.C. McAlpine, *3D printed bionic nanodevices.* Nano Today, 2016. **11**(3): p. 330-350.

189. Gul, J.Z., B.-S. Yang, Y.J. Yang, D.E. Chang, and K.H. Choi, *In situ UV curable 3D printing of multi-material tri-legged soft bot with spider mimicked multi-step forward dynamic gait.* Smart Materials and Structures, 2016. **25**(11): p. 115009.

190. Lei, D., B. Luo, Y. Guo, D. Wang, H. Yang, S. Wang, H. Xuan, A. Shen, Y. Zhang, and Z. Liu, *4-Axis printing microfibrous tubular scaffold and tracheal cartilage application.* Science China Materials, 2019. **62**(12): p. 1910-1920.

191. Guo, S.Z., K. Qiu, F. Meng, S.H. Park, and M.C. McAlpine, *3D printed stretchable tactile sensors.* Advanced Materials, 2017. **29**(27): p. 1701218.

192. Laszczak, P., L. Jiang, D.L. Bader, D. Moser, and S. Zahedi, *Development and validation of a 3D-printed interfacial stress sensor for prosthetic applications.* Medical engineering & physics, 2015. **37**(1): p. 132-137.

193. Tong, Y., E. Kucukdeger, J. Halper, E. Cesewski, E. Karakozoff, A.P. Haring, D. McIlvain, M. Singh, N. Khandelwal, and A. Meholic, *Low-cost sensor-integrated 3D-printed personalized prosthetic hands for children with amniotic band syndrome: A case study in sensing pressure distribution on an anatomical human-machine interface (AHMI) using 3D-printed conformal electrode arrays.* Plos one, 2019. **14**(3): p. e0214120.

194. Chen, S., T. Huang, H. Zuo, S. Qian, Y. Guo, L. Sun, D. Lei, Q. Wu, B. Zhu, and C. He, *A single integrated 3D-printing process customizes elastic and sustainable triboelectric nanogenerators for wearable electronics.* Advanced Functional Materials, 2018. **28**(46): p. 1805108.

195. Kong, Y.L., I.A. Tamargo, H. Kim, B.N. Johnson, M.K. Gupta, T.-W. Koh, H.-A. Chin, D.A. Steingart, B.P. Rand, and M.C. McAlpine, *3D printed quantum dot light-emitting diodes.* Nano letters, 2014. **14**(12): p. 7017-7023.

196. Saari, M., B. Cox, E. Richer, P.S. Krueger, and A.L. Cohen, *Fiber encapsulation additive manufacturing: An enabling technology for 3D printing of electromechanical devices and robotic components.* 3D Printing and Additive Manufacturing, 2015. **2**(1): p. 32-39.

197. Tong, Y., J.M. Murbach, V. Subramanian, S. Chhatre, F. Delgado, D.C. Martin, K.J. Otto, M. Romero-Ortega, and B.N. Johnson, *A hybrid 3D printing and robotic-assisted embedding approach for design and fabrication of nerve cuffs with integrated locking mechanisms.* MRS Advances, 2018. **3**(40).

198. Murbach, J.M., S. Currlin, A. Widener, Y. Tong, S. Chhatre, V. Subramanian, D.C. Martin, B.N. Johnson, and K.J. Otto, *In situ electrochemical polymerization of poly (3, 4-ethylenedioxythiophene)(PEDOT) for peripheral nerve interfaces.* MRS Communications, 2018. **8**(3): p. 1043-1049.

199. Johnson, B.N., K.Z. Lancaster, G. Zhen, J. He, M.K. Gupta, Y.L. Kong, E.A. Engel, K.D. Krick, A. Ju, and F. Meng, *3D printed anatomical nerve regeneration pathways.* Advanced functional materials, 2015. **25**(39): p. 6205-6217.

200. Johnson, B.N., K.Z. Lancaster, I.B. Hogue, F. Meng, Y.L. Kong, L.W. Enquist, and M.C. McAlpine, *3D printed nervous system on a chip.* Lab on a Chip, 2016. **16**(8): p. 1393-1400.

201. Singh, M., Y. Tong, K. Webster, E. Cesewski, A.P. Haring, S. Laheri, B. Carswell, T.J. O'Brien, C.H. Aardema, and R.S. Senger, *3D printed conformal microfluidics for isolation and profiling of biomarkers from whole organs.* Lab on a Chip, 2017. **17**(15): p. 2561-2571.

202. Wang, K., G. Ouyang, X. Chen, and H. Jakobsen, *Engineering electroactive dielectric elastomers for miniature electromechanical transducers.* Polymer Reviews, 2017. **57**(3): p. 369-396.

203. Parida, K., V. Kumar, W. Jiangxin, V. Bhavanasi, R. Bendi, and P.S. Lee, *Highly transparent, stretchable, and self-healing ionic-skin triboelectric nanogenerators for energy harvesting and touch applications.* Advanced Materials, 2017. **29**(37): p. 1702181.

204. Lai, Y.C., J. Deng, S. Niu, W. Peng, C. Wu, R. Liu, Z. Wen, and Z.L. Wang, *Electric eel-skin-inspired mechanically durable and super-stretchable nanogenerator for*

deformable power source and fully autonomous conformable electronic-skin applications. Advanced Materials, 2016. **28**(45): p. 10024-10032.

205. Li, S., W. Peng, J. Wang, L. Lin, Y. Zi, G. Zhang, and Z.L. Wang, *All-elastomer-based triboelectric nanogenerator as a keyboard cover to harvest typing energy.* ACS nano, 2016. **10**(8): p. 7973-7981.

206. Wang, S., L. Gong, Z. Shang, L. Ding, G. Yin, W. Jiang, X. Gong, and S. Xuan, *Novel Safeguarding Tactile e-Skins for Monitoring Human Motion Based on SST/PDMS–AgNW–PET Hybrid Structures.* Advanced Functional Materials, 2018. **28**(18): p. 1707538.

207. Zhang, Z., K. Du, X. Chen, C. Xue, and K. Wang, *An air-cushion triboelectric nanogenerator integrated with stretchable electrode for human-motion energy harvesting and monitoring.* Nano energy, 2018. **53**: p. 108-115.

208. Li, T., H. Luo, L. Qin, X. Wang, Z. Xiong, H. Ding, Y. Gu, Z. Liu, and T. Zhang, *Flexible capacitive tactile sensor based on micropatterned dielectric layer.* Small, 2016. **12**(36): p. 5042-5048.

209. Denby, B., T. Schultz, K. Honda, T. Hueber, J.M. Gilbert, and J.S. Brumberg, *Silent speech interfaces.* Speech Communication, 2010. **52**(4): p. 270-287.

210. Taylor, M.J. and S.C. Baicu, *Current state of hypothermic machine perfusion preservation of organs: The clinical perspective.* Cryobiology, 2010. **60**(3): p. S20-S35.

211. Guibert, E.E., A.Y. Petrenko, C.L. Balaban, A.Y. Somov, J.V. Rodriguez, and B.J. Fuller, *Organ preservation: current concepts and new strategies for the next decade.* Transfusion Medicine and Hemotherapy, 2011. **38**(2): p. 125-142.

212. Pawlaczyk, M., M. Lelonkiewicz, and M. Wieczorowski, *Age-dependent biomechanical properties of the skin.* Advances in Dermatology and Allergology/Postępy Dermatologii i Alergologii, 2013. **30**(5): p. 302.

213. Hueber, T., E.-L. Benaroya, G. Chollet, B. Denby, G. Dreyfus, and M. Stone, *Development of a silent speech interface driven by ultrasound and optical images of the tongue and lips.* Speech Communication, 2010. **52**(4): p. 288-300.

214. Webster, K.E., *Quantifying Renal Swelling during Machine Perfusion using Digital Image Correlation*. 2017, Virginia Tech.

215. Brigham, K. and B.V. Kumar. *Imagined speech classification with EEG signals for silent communication: a preliminary investigation into synthetic telepathy*. in *2010 4th International Conference on Bioinformatics and Biomedical Engineering*. 2010. IEEE.